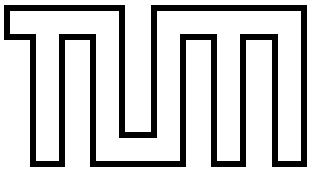

FAKULTÄT FÜR MEDIZIN

DER TECHNISCHEN UNIVERSITÄT MÜNCHEN

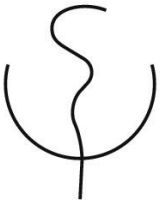

Development of Hybrid Optoacoustic Tomography, Pulse-Echo and Transmission Ultrasonography

Elena Merčep

Vollständiger Abdruck der von der Fakultät für Medizin der Technischen Universität München zur Erlangung des akademischen Grades eines

Doktors der Naturwissenschaften (Dr. rer. nat.)

genehmigten Dissertation.

Vorsitzender: Prof. Dr. Claus Zimmer

Prüfende der Dissertation:

1. Prof. Dr. Daniel Razansky
2. Prof. Dr. Dr. Fabian J. Theis

Die Dissertation wurde am 12.07.2018 bei der Technischen Universität München eingereicht und durch die Fakultät für Medizin am 17.06.2019 angenommen.

Abstract

Multispectral optoacoustic tomography (MSOT) is a fast developing imaging modality, combining the high contrast from optical tissue excitation with the high resolution and penetration depth of ultrasound detection [145]. Thanks to its unique capability to resolve multiple spectral signatures of endogenous and exogenous absorbers using multi-wavelength illumination, MSOT can non-invasively examine structural, physiological, molecular tissue features *in vivo* while being a low-cost non-ionizing imaging modality. Therefore MSOT excels other functional modalities like PET/SPECT that rely on the use of nuclear radioisotopes for gamma-ray detection and have poor spatial resolution [179], MRI that cannot capture high spatio-temporal resolution information [29], or other optical imaging techniques that suffer from poor spatial resolution at depths beyond 0.5 mm due to the high optical scattering properties of tissue [13].

MSOT has already found widespread application in pre-clinical imaging and is undergoing rapid clinical translation. Augmenting the stand-alone optoacoustic tomography (OAT) system by adding capabilities of conventional ultrasound (US) imaging is expected to further enhance the performance of MSOT and accelerate its clinical translation due to the current ubiquitous usage of ultrasound in routine clinical practice.

The presented work is dedicated to development of instrumentation and algorithms for the first hybrid optoacoustic, reflection (RUCT) and transmission (TUCT) ultrasound computed tomography system in the context of pre-clinical small animal imaging as well as translational research. Key technological aspects of combined ultrasound and optoacoustic tomography are analyzed and optimized regarding their influence on imaging performance of all modalities. Based on these findings, two hybrid optoacoustic-ultrasound (OPUS) imaging platforms were implemented: one for the whole-body mouse imaging, comprising a quasi-full or full-ring tomographic geometry capable of the simultaneous dual- (OAT+RUCT) or triple-modality (OAT+RUCT+TUCT) imaging, as well as the second setup for human imaging that employs a hybrid handheld detection probe. Imaging performance of the described platforms is characterized by means of numerical simulation, on phantoms and *in vivo* data in mice and humans.

Further contribution of the conducted research is to demonstrate optoacoustic and ultrasound image formation strategies for concave arrays followed by optimization of the algorithms considering non-conventional array geometries and, often contradicting, requirements imposed by the stand-alone imaging techniques. Besides instrumentation, signal processing and image reconstruction algorithms, methods for image quality improvement, including image contrast and feature enhancement, carry great importance in this work.

Finally, the unique capability of the hybrid imaging approach, that brings together optoacoustic and ultrasound contrast, to deliver complimentary anatomical, dynamic and molecular information is demonstrated in multiple highly relevant pre-clinical and human applications.

List of abbreviations

AA Acoustic attenuation

ADC Analog-to-digital converter

AQ Acquisition

CT Computed tomography

CW Continuous-wave

DAC Digital-to-analog converter

DAQ Data acquisition

DAS Delay-and-sum

DMA Direct memory access

DRF Dynamic receive focusing

FIR Finite impulse response

FOV Field of view

GPU Graphics processing unit

HR High-resolution

ICA Independent component analysis

KLM Krimholtz-Leedom-Matthaei

LR Low-resolution

ML-EM Maximum Likelihood - Expectation Maximization

MRI Magnetic resonance imaging

MSOT Multispectral optoacoustic tomography

MUX Multiplexing

OA Optoacoustic

OAT Optoacoustic tomography

OPO Optical parameter oscillator

OPUS Optoacoustic-ultrasound

PCIe Peripheral component interconnect express

PET Positron emission tomography

PRF Pulse repetition frequency

PW Pulsed-wave

RF Radio frequency

ROI Region of interest

RUCT Reflection ultrasound computed tomography

RX Receive

SA Sub-aperture

SAFT Synthetic aperture focusing technique

SPECT Single-photon emission computed tomography

SS Speed of sound

STA Synthetic transmit aperture

TOF Time of flight

TUCT Transmission ultrasound computed tomography

TX Transmit

US Ultrasound/Ultrasonography

UT Ultrasound transducer

Contents

1 Introduction

1.1 Motivation and objectives

Ultrasonography as a stand-alone modality is one of the most widespread in today's clinical practice, thanks to its intuitive handheld operation, instant feedback, cost-efficiency and absence of ionizing radiation [107]. In reflection mode, ultrasound (US) image formation relies on the acoustic reflection contrast due to acoustic impedance mismatch between different tissues. By utilizing acoustic signals transmitted through the object of interest, it becomes possible to recover information about the tissue acoustic properties, such as the speed of sound (SS) and acoustic attenuation (AA) , in a technique known as transmission ultrasound computed tomography (TUCT). The latter although can be applied in medicine for diagnostic examination has not yet become of great clinical significance [174].

Continuous efforts are underway to develop multimodal imaging solutions, such as US/CT or US/MRI [20], associated with technical challenges arising from the mutual interference between two modalities [88] while capitalizing on their complementary contrast and image co-registration. Integration of ultrasonography and optoacoustic tomography (OAT) can help to increase the diagnostically relevant content of the image. Optoacoustic (OA) imaging capitalizes on the photophonic effect [12] and combines advantages of high spatial resolution of pure US imaging, not affected by light scattering in deep tissues [145], with the high spectral specificity of optical methods. In contrast to conventional ultrasound, OA images are reconstructed from signals within an ultra-wide band of frequencies and represent distribution of the optical absorption distribution in tissue [199].

Augmenting the stand-alone OAT system with capabilities of reflection-mode ultrasonography will allow obtaining image of the tissue anatomy, not subject to its light absorption properties, for further quantification of the OA signal in the region of interest (ROI) located under US guidance. Besides, combination with transmission-mode ultrasound tomography can be used to improve the accuracy of reconstructed OA images by means of compensating for otherwise unknown heterogeneous distribution of the speed of sound [87].

The developed hybrid imaging approach is expected to benefit numerous medical applications. The availability of information on tissue morphology and its quantitative acoustic parameters such as speed of sound and attenuation, provided by the reflection- and transmission-mode ultrasonography, can complement the functional and molecular imaging results attained by the OA modality and ease their interpretation. Applications include cancer screening and study of tumor kinetics [16], quantification of blood oxygenation [171], image contrast enhancement with dual OA-US contrast agents [201] as well as various point-of-care diagnostic applications in humans such in the fields of melanoma [105, 177], inflammatory bowel disease (Crohn's disease) [101], breast abnormalities [28], thyroid cancer [39, 43].

This work focuses on a development of a hybrid imaging system that supports optoa-

coustic, reflection- and transmission ultrasound tomography modes, optimization of data acquisition and image reconstruction strategies as well as hardware components to achieve an accurate hybrid imaging performance.

The research has been carried out with the following objectives:

- Provide comprehensive theoretical foundation for physical contrast mechanisms behind each imaging modality of interest; formulate requirements to the system components needed to reproduce the respective underlying physical phenomena.
- Describe architecture of hybrid imaging device for combined optoacoustic tomography-reflection/transmission ultrasound computed tomography (OAT-RUCT-TUCT) modalities including key system components and interdependencies, data transfer and synchronization concept, data acquisition and image formation strategies.
- Develop simulation and experimental framework for analysis, characterization and optimization of OA and US imaging performance including aspects such as selection of optimal detector characteristics, improvement of image formation strategies, and artifacts suppression.
- Design and characterize new ultrasound transducer (UT) arrays tailored for combined OA-US tomographic image acquisition for pre-clinical and clinical applications.
- Conduct series of experiments to showcase the potential the developed hybrid imaging technology offers in a wide range of applications by visualizing label-free anatomical, functional and molecular information real-time *in vivo* in animals and humans.

1.2 Current state of research

From its first human application in the early 1940s [47] to becoming the most widespread imaging modality in today's clinical practice, ultrasonography is considered the ultimate choice whenever intuitive handheld operation, instant feedback, cost-efficiency and absence of ionizing radiation are of priority [107]. Affected by currently prevailing trends of further miniaturization of scanners, the merge of morphological and functional information as well as multimodal imaging and three-dimensional (3D) visualization, US imaging is rapidly expanding its traditional application portfolio. Among recent achievements in ultrasonography, notable are intravascular and needle guidance techniques [95, 127], three-dimensional (3D) color-Doppler US imaging [74], contrast-enhanced imaging [175] and elastography [167].

Another advantage of US is the low propagation speed of sound as compared to that of electromagnetic waves. This facilitates time-of-flight measurements in biological tissues, which in turn enable the quantification of material properties, temperature and other parameters affecting the speed of sound [64, 168]. In this regard, transmission ultrasound computed tomography (TUCT) has been used to map the distribution of speed of sound and acoustic attenuation in the female breast [104, 110], where recent clinical trials suggest

a superior performance with respect to standard screening approaches in terms of safety, examination time and patient comfort [46, 56, 106].

Continuous efforts are underway to develop multimodal imaging solutions, such as US/CT or US/MRI [20], associated with technical challenges arising from the mutual interference between two modalities [89] while capitalizing on their complementary contrast and image co-registration. Multimodal systems enable more comprehensive examinations of biological specimens without the need of repositioning them in independent setups, thus allowing for a reduction of motion artifacts and higher throughput [128]. By leveraging the strengths of different imaging modalities, hybridization provides a better picture of the tissue anatomy and function as compared to stand-alone modalities [24]. Multiple multimodal approaches have been exploited for both pre-clinical and clinical investigations at the macroscopic level by combining the different contrast mechanisms available in the whole-body imaging modalities, such as X-ray CT, MRI, PET or SPECT [20, 23, 157]. On the other hand, various microscopic methods can also be combined into multimodal devices in order to examine shallow tissue regions [79, 162].

Integration of ultrasound and optoacoustic tomography into one single device seems natural and can bring together the strengths of each method. OAT reflects an entirely different physical contrast mechanism by relying on generation of mechanical waves via transient absorption of pulsed laser radiation [12]. Images can be then formed by collecting the optoacoustically-generated responses using ultrasound detectors and applying reconstruction methods to render images of optical absorption distribution in tissue [199]. OAT benefits from the advantages of US imaging by making it possible to render images in real time while delivering diffraction-limited ultrasonic resolution not affected by intense light scattering in deep tissues [145]. On the other hand, owing to its optical contrast and high spectral selectivity, multispectral optoacoustic tomography (MSOT) has been shown to deliver label-free and contrast-enhanced information on tissue function, such as clearance kinetics [137, 186], cerebral function [139, 198] and blood oxygenation [60], as well as molecular contrast based on targeted contrast agents [114, 185] and genetic expression [164, 178].

An unprecedented combination of high spectroscopic selectivity and molecular sensitivity of optical methods with centimeter scale penetration and real-time imaging capability featured by ultrasound is making MSOT to a powerful functional and molecular imaging tool not only in routine small animal research but lately also for precision clinical diagnostics. Clinical translation of MSOT has been facilitated through the development of real-time hand-held imaging systems [14, 33], with first human studies focusing on vascular imaging [188], lymph node characterization [177] and breast imaging [28].

Hybridization is expected to further enhance the performance of MSOT with ultrasonography (US) appearing to be the natural partner as it also uses acoustically-detected signals for image formation. Such hybrid solution becomes particularly important for the clinical acceptance of MSOT since physicians are well accustomed to the use of US in clinical diagnostics.

To this date, a number of efforts have been made to combine US and OAT. However, fundamental differences in the contrast mechanisms and image formation methods have so far hampered an efficient hybridization. For example, pulse-echo US is generally performed with linear or convex arrays from a single access point to the sample, whereas TUCT and OA tomography (OAT) rely on a large tomographic coverage from multiple views for effective image reconstruction.

The common approach utilizing the conventional linear array US detectors where the hybrid imaging is achieved by adding fiber-guided light irradiation on one or both sides of the transducer probe [102, 140, 144, 148], attains good performance in sensing back-scattered ultrasonic waves. However, it is inefficient in recording of optoacoustically-induced signals and has generally resulted in reduced image quality and lack of quantification abilities, mainly due to limited tomographic view of the linear array geometry [34].

Additional reasons for the poor performance in the optoacoustic mode are the ultra-wideband nature of optoacoustic signals generated from common biological objects as well as the high optical absorption contrast between different tissues, both creating severe out-of-focus artifacts and making it challenging to apply the linear-array-based imaging approaches for collection and reconstruction of OT data. For instance, strong optoacoustic transients generated at the irradiation site, located outside of the imaged plane, may obscure weak signals from the deep-seated structures, either directly by propagating towards the probe, or via acoustic scattering.

Similar challenges were faced when the planar linear array approach was extended into three-dimensional hybrid imaging by means of the 1.75D/2D matrix array probes with very limited tomographic view around the imaged object [3]. Various methods have been suggested to alleviate the aforementioned drawbacks, including localized vibration tagging [81] and tomographic scanning approaches [59], which, however, compromise the real-time imaging performance.

An alternative, yet undesirable approach would instead employ two different detection systems, each specifically optimized for either US or OT imaging [38].

The signal intensity can also differ substantially for transmitted waves, back-scattered waves and OA responses [142, 153]. Even stand-alone modalities feature multiple hardware implementations for different applications. Particularly, the OA technology is characterized by a myriad of embodiments covering a large range of spatial and temporal imaging scales [51, 189]. Hybridization of pulse-echo US and OA imaging has been achieved with linear [144], concave [132] or hybrid (multi-segment) arrays [31]. Multimodal endoscopic [25, 207] and microscopic [51, 183] imaging systems based on single-element transducers have also been suggested. A different hybrid approach exploited for both pulse-echo US and TUCT consists in the excitation of US via passive (light absorbing) elements in OA imaging systems [52, 205]. Efforts have also been directed towards enhancing image quality by incorporating complementary information in reconstruction algorithms [87], clearly evincing the added value of multimodal versus stand-alone approaches.

Additional hybrid 2D and 3D implementations have been proposed to detect transmission of light-induced ultrasound waves through the imaged object for reconstructing speed-of-sound distribution, which was subsequently used to improve the quality of optoacoustic reconstructions [205]. Several groups proposed hybrid 2D and 3D imaging solutions based on tomographic array geometries, e.g. using concave arrays with passive element [49, 52] excitation for US image formation.

In general, concave arrays have proven to render a superior OA image quality as compared to the linear array approaches [38] , however, up to now there have been very few examples of efficient implementation of combined reflection- and transmission ultrasound computed tomography for concave detector geometry, often associated with increased computational and hardware complexity and implementation cost due to the use of extended number of detection elements to meet the strict inter-element pitch require-

ments [63].

1.3 Outline of the thesis

This doctoral dissertation is organized as follows:

CHAPTER 1: INTRODUCTION

The first chapter serves an introductory purpose in which I would like to familiarize the reader with the dissertation topic, present an overview of the thesis, and state its objectives.

CHAPTER 2: THEORETICAL BACKGROUND

The second chapter establishes the theoretical and technical background for the imaging technologies used in this work. The fundamental principles of the image generation in all modes employed through the study such as optoacoustic imaging, reflection- and transmission-mode ultrasonography as well as color Doppler are explained.

CHAPTER 3: TECHNOLOGICAL ASPECTS OF HYBRID OPTOACOUSTIC-ULTRASOUND SYSTEM IMPLEMENTATION

The third chapter presents the key instrumentation components and algorithmic strategies employed in the implemented hybrid optoacoustic-ultrasound system.

CHAPTER 4: HYBRID REFLECTION-MODE ULTRASOUND AND OPTOACOUSTIC TOMOGRAPHY USING CONCAVE DETECTOR ARRAYS

The forth chapter focuses on the evaluation of optimal detection geometries for hybrid optoacoustic/ultrasound imaging. The performance of the commonly employed arrays for image acquisition in both modalities is investigated, and the concave array design and algorithmic strategies are proposed that overcome the key limitations of real-time hybrid OT and pulse-echo US image acquisition. The new approach is characterized in numerical simulations and experiments on tissue phantoms and biological subjects.
Chapter 4 also demonstrates the applicability of the developed hybrid optoacoustic-ultrasound tomographic scanner for label-free anatomical studies as well as examination of the bio-distribution of contrast agents. These anatomical and functional imaging results are obtained for healthy mice *in vivo*.

CHAPTER 5: MULTI-SEGMENT DETECTOR ARRAY FOR HANDHELD HYBRID OPTOACOUSTIC AND ULTRASOUND IMAGING

Chapter 5 describes the implementation of real-time handheld detection technology that incorporates a novel multi-segment detector array approach that is optimally suited for image acquisition in both optoacoustic and pulse-echo ultrasound modes. The image rendering strategies are tested and optimized in numerical simulations and calibrated tissue-mimicking phantom experiments, while the *in vivo* imaging performance of the proposed OPUS system is demonstrated by scanning a healthy volunteer.
Chapter 5 further demonstrates the applicability of the developed handheld hybrid system for imaging of blood flow and oxygen state. Imaging results for the multimodal pulse-echo

ultrasound, multispectral optoacoustic tomography, and color Doppler are obtained from carotid artery of a healthy subject.

CHAPTER 6: TRIPLE-MODALITY TOMOGRAPHIC IMAGING SYSTEM FOR OPTOACOUSTIC, REFLECTION-, AND TRANSMISSION-MODE ULTRASONOGRAPHY OF SMALL ANIMALS

Chapter 6 describes an implementation of a multimodal imaging platform that enables accurate cross-sectional imaging in OAT, pulse-echo US and transmission ultrasound tomography modes. Imaging performance of the triple-modality imaging system is demonstrated in measurements on phantoms as well as *in vivo* mouse experiments.

CHAPTER 7: CONCLUSION AND OUTLOOK

Chapter 7 summarizes the obtained results and gives the reader a short outlook about the future developments.

APPENDIX – LIST OF PUBLICATIONS

Appendix contains the full list of publications including full paper submissions as well as conference contributions.

2 Theoretical Background

2.1 Optoacoustic imaging

In optoacoustic imaging, the acoustic waves are generated by absorption of short-pulsed laser radiation. Thus, generally the main goal of the optoacoustic image reconstruction problem is retrieving a map of the initial optoacoustic pressure, proportional to the absorbed energy density, on a pixel-by-pixel basis, effectively representing a point absorbing source problem. For light pulse durations verifying stress and thermal confinement conditions, the pressure field $p(\vec{r}, t)$ at a specific position $\vec{r}$ and time instant t may be approximated by [108]

$$p(\vec{r}, t) = \frac{\Gamma}{4\pi c^2} \int d\vec{r}' \frac{1}{|\vec{r} - \vec{r}'|} \frac{\partial H(\vec{r}', t')}{\partial t}|_{t'=t-|\vec{r}-\vec{r}'|/c}, \tag{2.1}$$

where $\Gamma = c^2\beta/C_P$ is the dimensionless Grueneisen parameter (c is the speed of sound in the medium, β is the isobaric volume expansion coefficient, and C_P is the specific heat), and $H(\vec{r}', t')$ is distribution of the deposited thermal energy converted per unit volume per unit time. For instance, for a delta pulse excitation, the analytical solution for the acoustic pressure, at $\vec{r}_0$ and time t, emitted from a uniformly absorbing spherical source, centered at $\vec{r}_s$ with radius a, can be obtained analytically [108], i.e.

$$p(\vec{r}_0, t) = A_0 \cdot U(a - |R - ct|)(R - ct)/(2R), \tag{2.2}$$

where A_0 is an amplitude of the initial pressure, $U(x)$ is the step function, and $R = |\vec{r}_0 - \vec{r}_s|$ is the distance from the center of the sphere. It can be readily seen that the pressure generated from a spherical absorber will resemble a typical "N-shape" profile, whereas both the magnitude and temporal duration of the signal are proportional to its size. Fig. 2.1 (a) shows an example of the simulated photoacoustic signal from a sphere of 1.5 mm radius assuming 1500 m/s propagation speed of sound through the sphere. Fig. 2.1 (b) displays the frequency spectrum of the signal, normalized and represented between 0 and 10 MHz. The maximal amplitude of the spectra defines the central frequency f_c of the source, which is approximately $f_c \sim \frac{0.8c}{2a}$ [134].

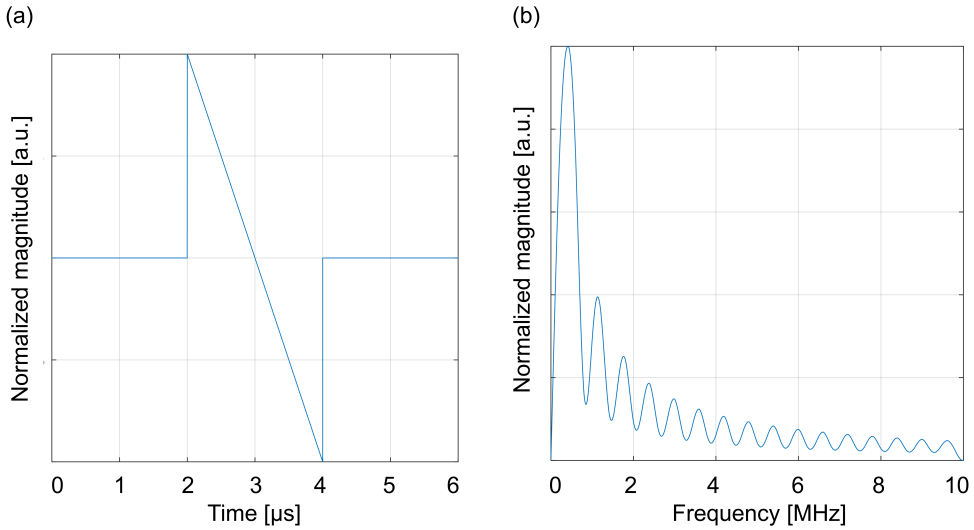

Figure 2.1: (a) Simulated optoacoustic signal from a spherical source with a radius of 1.5 mm; (b) Corresponding frequency spectrum.

The optoacoustic signals generated from a typical heterogeneous tissue containing absorbers of different sizes will generally contain frequencies in all spectral bands, including very low frequencies representing the size of the entire illuminated (imaged) region. As a result, the usable frequency range of optoacoustically-generated pressure signals may span an interval between tens of kHz to several tens of MHz [205]. In order to accurately capture these signals, the ultrasound detectors should ideally possess an ultra-wideband response [49].

Due to the very broadband frequency content of optoacoustic signals recorded from biological tissues, it becomes then impossible to efficiently focus the detection elements via physical or synthetic aperture techniques in order to obtain accurate spatially resolved information. Moreover, while in ultrasound imaging the focusing can be done in both transmission and detection, only the latter is possible in optoacoustics. Also, when imaging soft biological tissues with pulse-echo ultrasound, the acoustic impedance variations among the different tissues may only reach up to about 10% [45], whereas the optical absorption contrast in optoacoustics may differ by one or even two orders of magnitude for blood versus other tissues [57]. As a result of both inefficient focusing and high absorption contrast, optoacoustic image formation using phased arrays and other focusing techniques suffers from severe out-of-focus and limited view artifacts, impaired contrast, image blurring and overall lack of quantification abilities [10]. Thus, in contrast to pulse-echo ultrasound, correct image reconstruction in optoacoustic imaging is ideally achieved by an unfocused detection of optoacoustic responses from as many tomographic viewing angles as possible around the imaged object. It has been previously shown that, in partial tomographic view scenarios, only the regions effectively enclosed by the detection surface can be reliably reconstructed, while other parts of the image will suffer from limited-view artifacts [15]. In case of linear arrays used in B-mode ultrasonography, the typically available apertures may only provide tomographic views in the range of $\pm 30^{\circ}$ from the normal to the array [121], making it impossible reconstruct reliably optoacoustic images that cor-

rectly represent distribution of the deposited laser energy.

While optoacoustic images can be generated for each light wavelength separately by means of optical excitation through fast-tuning optical parametric oscillator based lasers, multispectral optoacoustic tomography (MSOT) has a unique ability of spectral identification of chromophoric molecules and particles distributed in tissue over background tissue absorption [146]. To recover the unique spectral signatures of optical reporter agents of interest in the presence of intrinsic tissue chromophores, special spectral processing methods are used [194]. Common approach to obtain images of the distinct absorbers is by using spectral fitting method. To achieve this, in the simplest form, assuming that it is possible to correct for the light fluence, every pixel in a single-wavelength optoacoustic image is represented as a combined contribution of all absorbing moieties with known molar extinction spectra α_m and unknown concentrations c_m. This can be written in the form of a linear equation system [146]

$$\mu_{n,m}(\lambda_k) = \sum_{m=1}^{M} \alpha_m(\lambda_k) c_m, \tag{2.3}$$

where $n = 1, ..., N$ is the number of data points (i.e. pixels in each single-wavelength optoacoustic image), $m = 1, ..., M$ is the number of distinct photoabsorbers of interest, and $k = 1, ..., K$ is the number of discrete excitation wavelengths.

In the matrix form the equation 2.3 reads

$$\mathbf{M} = \mathbf{AC} \tag{2.4}$$

Knowing the molar extinction spectra of the expected sources, i.e. the matrix **A**, Eq. 2.4 can be solved for the unknown concentrations c_m in each pixel in the sense of least square minimization for instance by the Moore-Penrose pseudoinverse $\mathbf{A}^{\dagger}$.

$$\mathbf{C} = \mathbf{A}^{\dagger}\mathbf{M}, \tag{2.5}$$

where **M** is the matrix of measured absorption values, **A** is the mixing matrix in which the columns contain the spectral signatures of the m distinct photoabsorbers, and **C** is the unknown matrix containing the concentration of each distinct absorber in the mixed pixel.

2.2 Reflection-mode ultrasound imaging

In a reflection-mode, or pulse-echo, ultrasound the acoustic waves at frequencies higher than 20 kHz are transmitted into the imaged tissue, reflected on various boundaries and scattered within the body, and subsequently travel back and received by the same ultrasonic transducer array. The propagation speed of acoustic waves in tissue c [m/s] is given by the Newton Laplace equation:

$$c = \sqrt{\frac{K_s}{\rho}}, \tag{2.6}$$

where K_s [Pa] is a coefficient of stiffness, ρ [kg/m^3] is the density, i.e. the denser or more rigid the material, the higher the propagation speed. In soft tissue, the velocity has a mean

value of 1540 m/s [203]. Variations typically do not exceed 10% [180]. The product of sound velocity and material density is called acoustic impedance Z [rayl/m^2]:

$$Z = c\rho, \tag{2.7}$$

Reflection occurs when ultrasonic waves encounter the boundary between two materials with different acoustic impedances, where the amount of energy getting reflected back is dependent upon the acoustic impedance of both materials and known as the reflection coefficient [7]:

$$R = \left(\frac{Z_2 - Z_1}{Z_2 + Z_1}\right)^2, \tag{2.8}$$

where Z_1 is acoustic impedance of the first material, is Z_2 acoustic impedance of the second material.

Travel time of the sound wave between the emitted pulse and the returned echo allows calculating the distance to the reflecting interface or point scatterer, and subsequently to generate a two-dimensional (B-mode or brightness mode) image of tissue structures. This operation of coherent summation is commonly known as delay-and-sum (DAS) beamforming [100, 196]. Thus, the basic contrast in ultrasound imaging originates from differences in tissue reflectivity on a pixel-by-pixel basis.

Typically, linear array geometries are used for two-dimensional (cross-sectional) ultrasonography. A typical array consists of 128 or 256 regularly spaced transducer elements separated by narrow spacers. In order to achieve cross-sectional imaging capability, the array is also focused on the imaging plane by means of a cylindrical acoustic lens. When operated as a phased array system, ultrasonic arrays are able to form images employing both steering and focusing of the beam in arbitrary directions in the imaged plane by applying suitable time delays on the driving input signals to the array elements. Beamforming at reception can be accomplished analogously to the transmission process with help of delay-and-sum circuitry or digital beamforming [176]. By inducing proper time delays in each channel it is possible to align received echoes before their coherent summation [120].

Under the paraxial approximation, the beam directivity pattern $D(\theta)$ can be expressed as a function of the angle θ from the center axis of the array to the source point in the imaged plane (x, y), which in the far-field is given by [98]:

$$|D(\theta))| \propto \left|\frac{sin(\frac{N\pi dsin(\theta)}{\lambda})}{sin(\frac{\pi dsin(\theta)}{\lambda})}\right|, \tag{2.9}$$

where λ is the acoustic wavelength, N is the number of array elements, and d is the distance between the centers of two adjacent elements (pitch size). In order to optimally confine the energy in the main beam of the array and reduce side (grating) lobes, the spatial sampling theorem criterion has to be fulfilled [151], that is, the pitch size should be ideally less than half a wavelength. If strong scatterers are present in the grating lobes of an undersampled array, they result in ghost responses, which severely limit contrast in the images. The sidelobe level can be dealt with by performing a smooth apodization of the aperture by applying windowing functions [170]. On the other hand, the array pitch does not influence the main beam width or the amplitude of the side-lobes. The width of the main beam or the lateral resolution can only be improved by increasing the aperture [117].

According to the Rayleigh criterion, two point sources of equal amplitude can be separated if the first source is placed at the maximum point of the beampattern, $x = 0$, and the second source at a point where the beampattern is zero, which occurs at the distance b:

$$b = \frac{F}{N \cdot d} \cdot \frac{c}{f_0}, \tag{2.10}$$

where f_0 is the center frequency of the transducer elements, F is the focal depth and c denotes speed of sound in medium. It can be seen that the beam width in the focal zone is inversely proportional to the transducer aperture size $N \cdot d$ [8]. This suggests making the aperture as large as possible, which in turn imposes limitations on the minimal achievable pitch size.

Since US imaging commonly employs the pulse-echo method, its axial resolution along the wave propagation direction is determined by temporal length of the transmitted pulses. For this reason, high-frequency system will generally deliver better axial resolution. However, the acoustic pressure field in reflection mode ultrasound is defined by the transducer geometry and does not depend on the size of the scatterers. Centre frequency and the bandwidth of the backscattered and reflected acoustic signals are correspondingly determined by the frequency and duration of the transmitted ultrasound pulse [61] while the signal amplitude results from the acoustic impedance mismatch between tissue boundaries. It is therefore possible to perform fully dynamic focusing in arbitrary direction with the given spatial resolution, and thus produce high-resolution ultrasound images with linear and phased arrays despite their limited tomographic view.

Beamforming techniques can be broadly divided into two categories:

- Real aperture beamforming, also known as conventional or line-by-line, is the oldest and simplest array signal processing algorithm that employs electronic delay-and-sum beamforming [86] where only imaging along one line in receiving is used. The technique is realized by all array elements, successively delayed in time relative to one another, to focus the transmitted beam and, optionally, steer it in a given direction. Delays are also applied during the reception. While the focus of the transmitted field remains static – associated with a single delay profile for a particular discrete depth, the back-scattered field can be dynamically focused at all points across the scan line (multiple delay profiles are used to process the echoes originating at different depths), known as dynamic receive focusing (DRF) [118] . Due to the fixed focus on transmit, DRF provides the best pulse-echo spatial resolution near the transmit focal depth [96], and in real aperture imaging it is impractical to implement dynamic focusing on transmit as it will require an unlimited data acquisition time [208].

- Synthetic aperture beamforming combines information from emissions close to each other. One method to realize the synthetic aperture is by transmitting an unfocused wave from every single element sequentially and receiving the echo signals with all elements simultaneously with subsequent DAS applied to the stored RF data, known as synthetic transmit aperture (STA) imaging or synthetic aperture focusing technique (SAFT) [147]. In contrast to DRF, in SAFT every image line is imaged as many times as the number of emissions used. This will create an equal amount of low resolution images which are summed up to create one high resolution image [92,192]. The advantage of this approach is that a full dynamic focusing can be applied to the

transmit and the receive, giving the highest quality of image.

2.3 Transmission-mode ultrasound imaging

In transmission ultrasound computed tomography (TUCT) two transducer elements are used that are submerged in water and mounted opposite to each other. An ultrasound pulse is transmitted by one of the transducers and travels through the object and coupling medium to the other one. From the received pulse some acoustical properties of the material, such as sound propagation velocity as well as acoustic attenuation, along the path of the sound pulse can be derived [174]. A number of projections (or linear scans of the object cross-section in one direction) are measured in different directions within one plane to obtain a tomographic image. The propagation of acoustic waves can be described by the following acoustic wave equation [54]:

$$\frac{1}{c^2}\frac{\partial^2 p(\vec{r},t)}{\partial t^2} - \nabla^2 p(\vec{r},t) = 0, \tag{2.11}$$

where $p(\vec{r},t)$ is the pressure field at a specific position $\vec{r}$ and time instance t, and c is the speed of sound in the medium. Eq. 2.11 has a harmonic solution:

$$p(\vec{r},t) = A(\vec{r})e^{-if(\theta(\vec{r})+t)}, \tag{2.12}$$

where $A(\vec{r})$ and $\theta(\vec{r})$ are the amplitude and phase of the wave, respectively. Combining equations 2.11 and 2.12 and taking a high-frequency approximation, the Eikonal equation is obtained [116]:

$$\left|\nabla^2\theta(\vec{r})\right| = \frac{1}{c^2} = S(\vec{r})^2, \tag{2.13}$$

where $\theta(\vec{r})$ corresponds to the time-of-flight (TOF) that is required for the wave to reach a point $\vec{r}$, and S is the slowness or the inverse of the speed of sound. Eq. 2.13 gives rise to the geometrical acoustics and describes the arrival time for the wavefront at any given point of the domain assuming that the sound travels along the shortest path (Fermat's principle) [156].

Speed of sound (SS) in a cross-section of an object can be determined using TOF measurements. When $c(l)$ is the local speed of sound, where l is the coordinate along the propagation path of the sound pulse, the total TOF T at small parts, dl, on the path L, between the two transducers is:

$$T = \int_L \frac{1}{c(l)} dl \tag{2.14}$$

A set of linear scans measured in different directions can be reconstructed into an image of the local TOF per unit length per pixel $1/c(x,y)$, which then can be transformed into an image of the local sound propagation velocity $c(x,y)$ by inversion. In order to satisfy the condition of zero TOF value outside the object, the TOF measurement with only water between the transducers is done and subtracted from other measured values [174].

Acoustic attenuation (AA) in a cross-section of an object can be obtained using the amplitude-decay method [17], and the inversion problem for the attenuation reconstruc-

tion can be formulated as follows:

$$\int_L \alpha_0 dl = \frac{1}{f_c} ln \left(\frac{A_S(f)}{A_W(f)} \right), \tag{2.15}$$

where the integral is taken along the ray path L, α_0 is attenuation coefficient, $A_S(f)$ is magnitude of the spectrum with the sample in place, $A_W(f)$ is magnitude of the spectrum with no sample in place, and f_c is the central frequency of the signal.

There exist several approximations of geometrical acoustics that provide computational models to simulate the wave propagation process. These include the straight-rays approximation [67], that accounts for the transmission process of the wave only, and the bent-rays approximation [6, 116], that accounts for both – transmission and refraction processes. Alternatively, there are more complex algorithms based on computational models that directly solve the wave equation (Eq. 2.11) known as full-wave inversion (FWI) methods [184].

A clear advantage of transmission-mode measurement versus the reflection mode is that, in addition to the ability to image anatomy, it offers the capability of tissue characterization [68]. Using TUCT different acoustic properties of the tissue, such as the sound propagation velocity and the attenuation coefficient can be determined, while only differences in acoustic impedance can be detected in the reflection-mode ultrasound imaging [174].

2.4 Color Doppler ultrasound imaging

Realization of color Doppler ultrasound imaging is based on the well-known Doppler principle that Christian Doppler first proposed in 1842 [44]. The sound emitted by or reflected from a moving object will shift to a higher frequency when moving toward the stationary observer and to a lower frequency when the object is moving away [69]. The difference between the frequency of the transmitted (incident) pulse f_0 and the received (reflected) pulse f caused by relative motion between the reflector and the transducer's transmitted beam is called the Doppler frequency shift and is given by:

$$\Delta f = \frac{2v}{c} f_0, \tag{2.16}$$

where v is the velocity of the scatterer in a given direction, c is the sound velocity in the medium.

If the direction of the incident beam is at angle (θ) to the direction of blood flow, the v in the Doppler equation 2.16 is replaced by the component of the velocity in the direction of the flow (obtained by the cosine of th angle, $cos\theta$) [125]:

$$\Delta f = \frac{2v \cdot cos\theta}{c} f_0 \tag{2.17}$$

To determine the velocity of the scatterer, the equation can be rewritten as follows:

$$v = \frac{\Delta f \cdot c}{2 f_0 \cdot cos\theta} \tag{2.18}$$

Thus, if the angle of beam incidence and the Doppler shift frequency are known, and the transducer frequency and the speed of sound in tissue are assumed constant and known, the velocity of blood flow can be calculated using the above equation. It is further important to note that the $cos\theta$ in the denominator of equation 2.18 requires that the Doppler angle be less than about $60°$, otherwise a small error in θ will produce a large error in the measured velocity [133].

There are two common techniques of Doppler ultrasonography: the continuous-wave (CW) method is performed by two transducers, one for continuously transmitting the sound wave and another for receiving echo signals; and the pulsed-wave (PW) Doppler method is performed by sending bursts of short US pulses into the tissue and receiving them at a predetermined pulse repetition frequency [208]. In the PW Doppler, similarly to B-scan line-by-line pulse-echo image, many RF back-scattered signals are obtained at multiple sampling sites (gates) along each scan line for a series of emitted US pulses. The group of pulses required to estimate the velocity of blood flow at a particular gate is known as a packet or a pulse train with the time between successive pulse trains determining the effective pulse repetition frequency (PRF) [154]. The frequency shift measured at each gate is automatically correlated using an autocorrelation function and encoded in the image via a preset color scheme with positive Doppler shifts (blood moving towards the transducer) represented by red colors and negative shifts represented by blue colors [149].

Color Doppler images are generally combined with grayscale (B-mode) images to display duplex ultrasonography images, allowing for simultaneous visualization of the anatomy of the area [22].

3 Technological Aspects of Hybrid Optoacoustic-Ultrasound System Implementation

Components of the experimental setup for hybrid OPUS imaging are schematically represented in Fig. 3.1 and include: (1) illumination unit comprising a pulsed tunable laser and optical fibers; (2) ultrasound transducer array; (3) optoacoustic data acquisition unit; (4) ultrasound electronics; (5) multiplexing unit; and (6) the main PC.

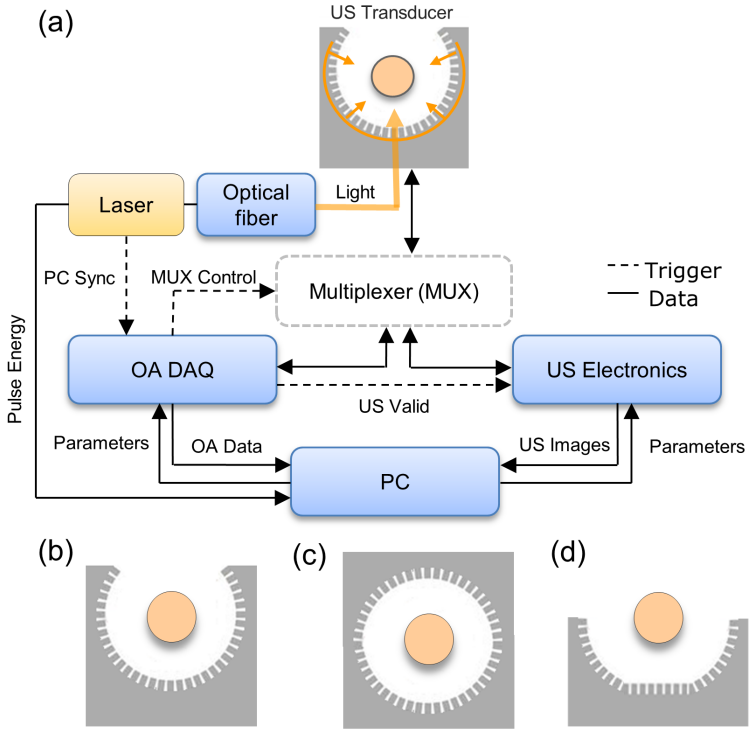

Figure 3.1: (a) Block diagram of the experimental setup for hybrid OPUS imaging. Several ultrasound detection array configurations were considered; (b) Arc-shaped (concave) transducer for whole-body small animal imaging providing angular coverage of 270° and center frequency of 5 MHz; (c) Full-ring transducer for whole-body small animal imaging providing angular coverage of 360° and center frequency of 5 MHz; (d) Multi-segment transducer for handheld imaging with 256 elements providing angular coverage of $\sim$ 170° and center frequency of 7.5 MHz.

3.1 Illumination unit

For the OA signal excitation, the pulsed Nd:YAG-pumped optical parameter oscillator (OPO) laser (InnoLas Laser GmbH, Krailling, Germany) was used that operates at max. 25 Hz repetition rate, has per-pulse energy of up to 120 mJ (750 nm), pulse duration of 9 ns and a tunable wavelength range of 680–980 nm.

In order to uniformly illuminate the imaged cross-section of the sample from multiple view angles, in case of the animal scanner, the laser beam is directed onto the animal's surface through the optical fiber bundle consisting of approx. 620 fibers partitioned into 12 outputs that create a ring-shaped illumination pattern, coinciding with the detection plane of the ultrasound transducer array.

In case of the handheld imaging, the maximum per-pulse energy output is set to 25 mJ and the laser light is guided to the specimen via a custom-made fiber bundle (CeramOptec GmbH, Bonn, Germany) with total number of approximately 893 fibers equally split between two output ferrules made of stainless steel, each having fiber output surface with dimensions of 40 mm by 0.6 mm. The outputs of the two ferrules are attached to the lateral sides of the array and oriented at a $\sim 17^\circ$ angle so that the two illuminating beams intersect the cross-sectional imaging plane roughly at the tissue surface.

3.2 Ultrasound transducer arrays

The types of transducers that were considered in the simulations and experiments are schematically depicted in Figs. 3.1(b-d). We used three transducer arrays (Imasonic SaS, Voray, France), two of those are custom-designed primarily for whole-body small animal imaging, consisting of 512 elements, with central frequency of 5 MHz, nominal TX/RX bandwidth of 60%, radius of curvature of 40 mm, and angular coverage of 270° (Fig. 3.1 (b)) and 360° (Fig. 3.1 (c)). Pitch of the individual elements for these transducers constitutes 0.37 mm and 0.42 mm, respectively.

The third type of the transducer array (central frequency of 7.5 MHz) is mainly intended for the handheld operation (Fig. 3.1 (d)). It combines two detector geometries, the linear segment consisting of 128 elements with 0.25 mm inter-element pitch and 10 mm height. Cylindrical focusing on the elevational axis (focal distance - 34 mm) was achieved by bending the active array surface. Attached to the linear part are two concave segments, each having 64 cylindrically-focused elements with 0.6 mm inter-element pitch, 10 mm height, and a focal distance of 38 mm. The radius of curvature for the concave part in the x-y plane was selected to be 40 mm so that the combined angular coverage of the multi-segment array constitutes 170°.

3.3 Optoacoustic data acquisition unit

Optoacoustic data acquisition system supports simultaneous digitization of signals from up to 512 channels at up to 50 Hz repetition rate and sampling rate of 40 MS/s. The number of samples recorded for each pulse is set to 2030, which, assuming sound propagation velocity of 1500 m/s, corresponds to the sufficiently large field of view of approximately 7.6 cm.

A 1-Gbit Ethernet connection is used to transmit the optoacoustic pressure signals, received and digitized by a data acquisition system to a designated PC.

3.4 Ultrasound electronics

The US electronics (S-Sharp Corporation, Taiwan) is composed of (1) PC motherboard; (2) PCIe GPU NVIDIA video card; (3) 4xPCIe ultrasound acquisition boards; (4) 512-channel connector board.

The PC motherboard connects the GPU board and the ultrasound acquisition boards. The ultrasound acquisition boards include: 2 transmitter boards (TX) and 2 receiver boards (RX), with 64 channels each.

The transmitter board (TX) generates the electrical pulse signals which are sent to the ultrasound transducer to produce the ultrasonic waves. For excitation a bipolar rectangular pulse is used with adjustable frequency f in the range of 1-10 MHz, period $T = 1/f$, and pulse width $P = T/2$, transmit voltage between 5 Vpp and 60 Vpp. The minimum and maximum cycle can be specified. Both are applied to all transmit voltages. If the peak voltage is as high as 60 V, the number of cycles is limited to 3 as the higher number can damage the transducer.

The receiver board (RX) acquires the ultrasound signal with a receive sampling frequency between 18 to 80 MS/s, which constitutes 4 times the transmit pulse frequency.

The 512-channel connector board has two functions. It switches the ultrasound transducer channels between the TX and RX boards. It also adjusts and converts the electrical signal from digital-to-analog (DAC) and from analog-to-digital (ADC).

PCIe ultrasound acquisition boards transfer data to the PC motherboard using DMA where a high level GPU is subsequently used to reconstruct the images using CUDA, and the reconstructed US images are then transferred as binary raw data files via Ethernet to the main PC.

3.5 Multiplexing unit and acquisition control

Acquisition of OA and US data is performed in interleaved manner facilitated through a custom-made programmable multiplexing control unit (MUX) connected to the transducer array. A laser-triggered signal from the OA data acquisition system (OA DAQ) controls transition of the MUX state between two operation modes:

- Receive-only mode (optoacoustic mode): ultrasound waves generated in the object in result of laser radiation are received by the transducer elements.
- Transmit-and-receive mode (ultrasound mode): ultrasound waves are emitted by the transducer elements and ultrasound waves reflected and/or transmitted by the object are received by the transducer elements.

In this way, any possible acquisition conflict is avoided by allocating strictly defined non-overlapping time windows for the OA and US data recording and processing. Fig. 3.2 schematically describes the timeline of the interleaved OA and US acquisition in case of 10 Hz laser repetition rate.

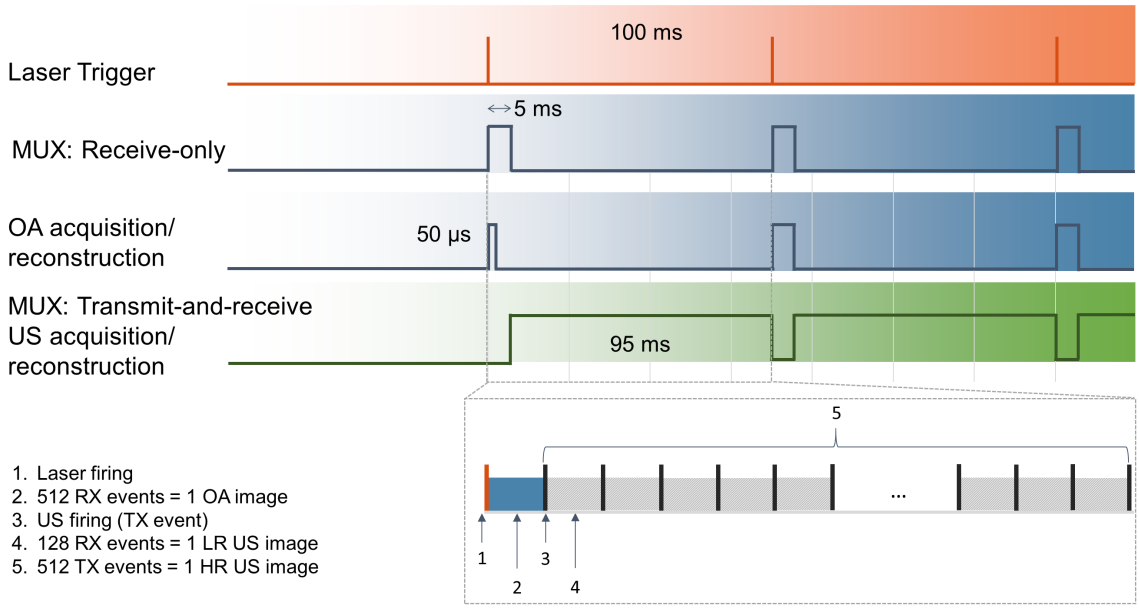

Figure 3.2: Timing diagram of interleaved OPUS image acquisition

3.5.1 OA acquisition

Acquisition of raw OA data is fast – generated photoacoustic signals are received on all transducer channels simultaneously, which yields one OA acquisition and can be further referred as a scan line. For OA mode, $1 \times Scanline$ can form one OA image (Fig. 3.3 (a)). In terms of the acquisition time, collection of 2030 samples with 40 MS/s sampling rate yields $\sim 50\mu s$ for one OA scan line.

3.5.2 US acquisition

Acquisition of raw US data is more time-consuming due to round-trip acoustic wave travel distance and multiple transmit-receive events required to form a complete US image.

For collection of reflection- and transmission mode US data, the synthetic transmit aperture (STA) technique is employed (Fig. 3.3 (b)).

A transmission (TX) of a pulse from the first single channel of the active sub-aperture of 128 channels (TX1) produces unfocused transmit beam. Reflected (or backscattered) and/or transmitted US signals are recorded by all channels of the active sub-aperture (RX1-128). Then the active group is moved by one channel and the transmit-receive cycle repeats (TX2, RX2-129; TX3, RX3-130;...TX512, RX512,1-127). Transmission by the last channel (TX512) and reception with the active group RX512, 1-127 completes the first acquisition (AQ1) . Totally four acquisitions are required to collect reflected/transmitted signals for any pair of transmit-receive channels.

Therefore in US mode, $N_{TX} \times Scanline$ comprise a single acquisition (AQ) and can form one US image where N_{TX} is a finite number of transducer channels emitting US waves. Considering collection of 2030 samples with 20 MS/s sampling rate, this results in ~52 ms for a single AQ when $N_{TX} = 512$. Individual or multiple AQs are executed after trigger

signal and a final US image is generated after all AQs are complete.

Table 3.1 illustrates the requirements and the resulting data rate associated with each of implemented imaging modes calculated from consideration of laser repetition rate of 10 Hz and total number of transducer channels equal to 512, which corresponds to the animal scanner.

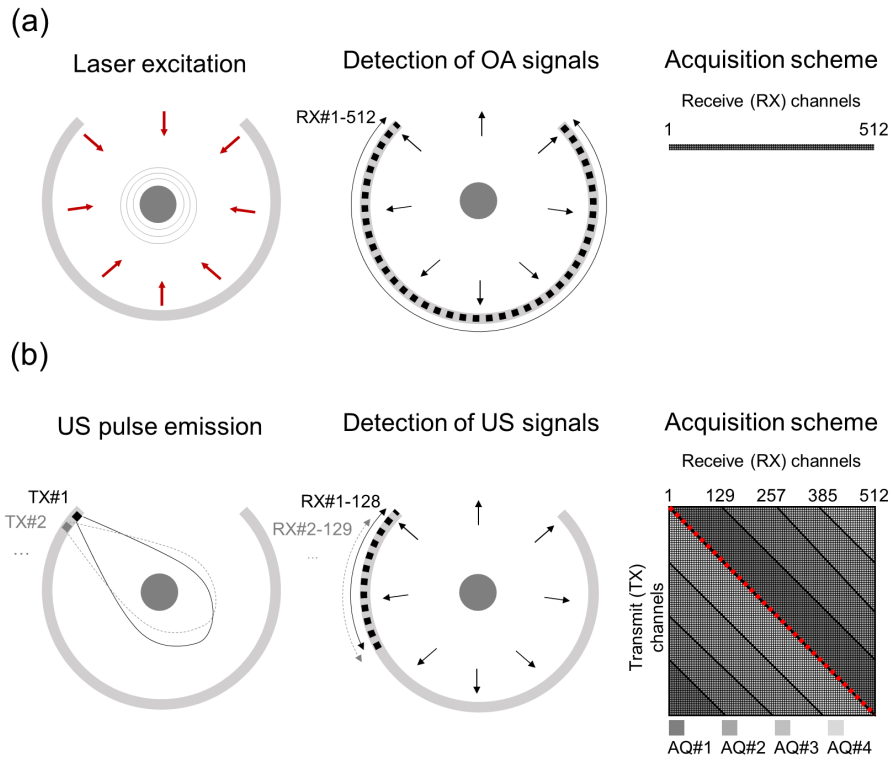

Figure 3.3: Generation and acquisition schemes for (a) optoacoustic and (b) ultrasound signals

Table 3.1: Data volume and rate for three imaging modes (based on calculation for 10 Hz laser repetition rate and 512-channel UT array)

Mode	OAT	RUCT	TUCT
Number of AQs	N/A	1	4
Number of samples	2030	2030	4060
Sampling rate	40 MS/s	$f_{TX} * 4$ e.g. 20 MS/s for f_{TX}=5 MHz	$f_{TX} * 4$ e.g. 20 MS/s for f_{TX}=5 MHz
Data per frame	2030 samples * 16 bit * 512 RX ch = 16.6 Mbit	2030 samples * 16bit * 128 RX ch * 512 TX ch * 1 AQ = 2.1 Gbit	4060 samples * 16 bit * 128 RX ch * 512 TX ch * 4 AQ = 17Gbit
Data rate (10 Hz)	166 Mbit/s	21 Gbit/s	170 Gbit/s
Time per frame	50 μs per acq. (RX) = 50 μs	100 μs per acq. (TX/RX) * 512 TX ch * 1 AQ = 52 ms	200 μs per acq. (TX/RX) * 512 TX ch * 4 AQ = 410 ms

3.6 Ultrasound image formation

3.6.1 Signal processing

The following signal processing steps precede the reconstruction of the US image.

Anti-aliasing filtering (AAF) is used to filter the received radio frequency (RF) signal prior to the ADC to reject dc signals and to band limit the signal for antialiasing. AAF is a band-pass filter which is composed of a single-pole high-pass filter and a second-order low-pass filter. For both filters, their cutoff frequencies are programmable. The high-pass filter can be configured as a ratio of the low-pass filter cutoff. For all experiments the low and high-pass cutoff frequencies were set to $f_{LP} = 0.7 \cdot 1/4.5 \cdot f_s$, and $f_{HP} = f_{LP}/8.57$, respectively, where the sampling frequency f_s is set to be four times the frequency of the emitted pulse f_{TX} e.g. 24 MS/s in case of f_{TX}=6 MHz.

The RF-signal received by the transducer is a real, narrowband and its frequency spectrum is confined to a narrow band centered on a carrier frequency, namely, the frequency of the transmitted signal [161]. In order to remove the frequency shift between the spectrum of the received signal and the center of the observed spectral band, *baseband demodulation*, also commonly referred to as IQ-demodulation (In-phase-Quadrature), is commonly performed on the signals and includes three main steps [99]

- Down-mixing
  The real-valued received signal is shifted to the baseband such that the subsequent processing can be done in complex-valued baseband domain. This is done by multiplication of the real valued RF-signal $x_{RF}(t)$ with a complex sinusoid signal:

$$x_{IQ}(t) = x_{RF}(t) \cdot exp(-i2\pi f_{TX} \cdot t), \tag{3.1}$$

  where f_{TX} is the carrier frequency, or the frequency of the transmitted signal. The

resulting signal $x_{IQ}(t)$ is complex.

- Low-pass filtering
  After down mixing, the complex signal is low-pass filtered using a low-pass finite impulse response (FIR) filter with rectangular frequency response to remove the negative frequency spectrum and noise outside the desired bandwidth. The cutoff frequency was set between 6 and 9 MHz depending on the center frequency of the UT detector array used in the study.

- Up-mixing
  To shift the frequency spectrum from the base-band and back to its original band, the signal is up-mixed. Up-mixing is achieved by just multiplying the filtered IQ-signal $x'_{IQ}(t)$ by the inverse of the complex exponential used for the down-mixing:

$$x(t) = x'_{IQ}(t) \cdot exp(i2\pi f_{TX} \cdot t) \tag{3.2}$$

3.6.2 Image reconstruction

Beamforming is performed with baseband demodulated signals using synthetic transmit aperture (STA) imaging technique applied across several sub-apertures (sub-groups of the transducer elements that span a specific angle). Fig. 3.4 shows the image reconstruction workflow.

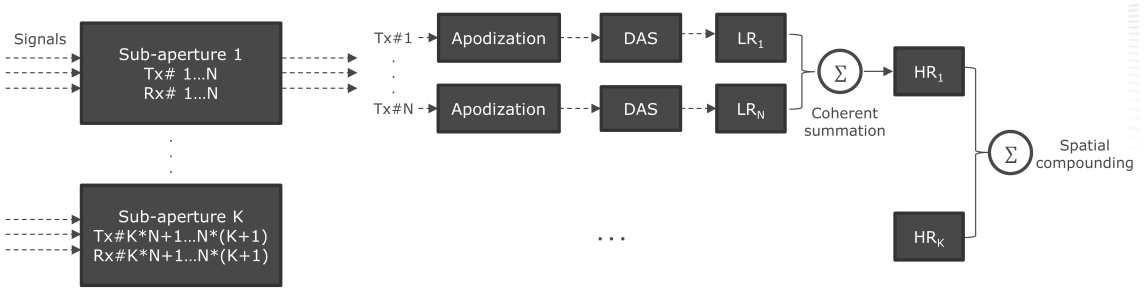

Figure 3.4: Block diagram illustrating the key steps of the US image reconstruction

STA imaging creates a high-resolution (HR) image by coherently combining many low-resolution (LR) images. The LR images are created from the signals of transmit-receive element pairs of each sub-aperture (SA). For each transmit (TX) channel of the SA the backscattered signals on the receive (RX) channels are backprojected based on a time of flight calculation (also known as delay-and-sum (DAS) beamforming [100]).

The binary apodization matrix is used to weight the received signals based on their origin with respect to the selected sub-aperture in order to reduce side-lobe artifacts by assuming gradually expanding aperture from near- to far-field.

Since the time of arrival of the signal from each pixel location and each TX-RX pair is calculated, all back-projections reconstructions (LR images) add up at the points where the isochronal lines (lines connecting pixels for which the time of flight of the sound wave to a particular receiver has the same value) overlap on a real scatterer. At other locations, the individual images add incoherently resulting in a much lower signal level.

In order to reduce the speckle noise and increase contrast and resolution, a spatial compounding technique [135] is applied across different HR sub-images corresponding to different sub-apertures. The number of images for spatial compounding across different view angles determines the level of speckle reduction and image smoothing, and relates to overlap between adjacent sub-apertures, size of individual sub-aperture and the total angular span of the transducer array. Overlap between the sub-apertures can be adjusted between 0 and 0.9 times the individual sub-aperture size.

4 Hybrid Reflection-Mode Ultrasound and Optoacoustic Tomography using Concave Detector Arrays

4.1 Introduction

Implementation of hybrid imaging using optoacoustic tomography (OAT) and ultrasound (US) brings together the important advantages and complementary features of both methods. Yet, the fundamentally different physical contrast mechanisms of the two modalities may impose significant difficulties in the optimal tomographic data acquisition and image formation strategies. In this chapter we investigate the applicability of the commonly applied imaging geometries for acquisition and reconstruction of hybrid optoacoustic tomography and pulse-echo ultrasound (OPUS) images.

Experimental validation was performed using a custom-made multiplexer unit executing switching between the two modalities employing the same transducer array. A variety of array probes with different angular coverage were subsequently tested, including arrays for clinical handheld imaging as well as stationary arrays for tomographic small animal imaging. The results demonstrate that acquisition of OAT data by mere addition of illumination source to the common US linear array geometry may result in significant limited-view artifacts and overall loss of image quality. On the other hand, unsatisfactory US image quality is achieved with tomographic arrays solely optimized for OAT image acquisition without considering the optimal transmit-receive beamforming parameters.

Optimal selection of the array pitch size, tomographic coverage and spatial compounding parameters has achieved here an accurate hybrid imaging performance, which was experimentally showcased in tissue-mimicking phantoms, *post mortem* mice and handheld imaging of a healthy volunteer.

4.2 Materials and methods

4.2.1 Experimental system

Key instrumentation aspects and algorithmic strategies employed in the hybrid OPUS system are described in Chapter 3. Here we remind the reader and repeat some of the description for completeness.

Components of the OPUS experimental setup are schematically represented in Fig. 4.1 (a).

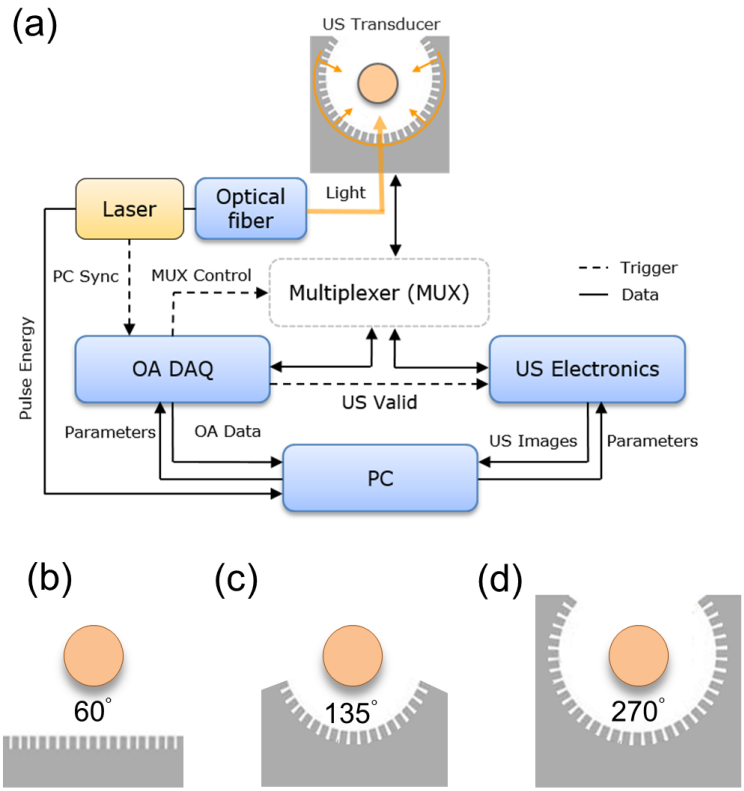

Figure 4.1: (a) Block diagram of the experimental setup for hybrid USOT imaging. Several ultrasound detection array configurations were considered; (b) Linear array geometry with 128 elements providing approximately 60° tomographic coverage around the imaged object; (c) Arc-shaped (concave) transducer geometry for handheld operation with 64, 128 or 256 elements providing angular coverage of 135° and center frequency of 4 MHz; (d) Arc-shaped (concave) transducer for whole-body small animal imaging with 128, 256 or 512 elements providing angular coverage of 270° and center frequency of 5 MHz.

Switching between optoacoustic imaging and ultrasonography is facilitated through a custom-made multiplexer connected to the US transducer array. A pulsed Nd:YAG-pumped optical parameter oscillator (OPO) laser (InnoLas Laser GmbH, Krailling, Germany) uniformly illuminates the imaged cross-section of the sample from multiple view angles through the optical fiber bundle connected to the light diffuser. Additionally, the option of pulse energy monitoring based on the spectrograph allows for normalization of the data. The laser source operates at 10 Hz repetition rate, has per-pulse energy of up to 120 mJ, pulse duration of 9 ns and a tunable wavelength range of 680–980 nm, yet OAT images in the current study were acquired at a fixed wavelength of 800 nm (oxygenated and deoxygenated hemoglobin have similar absorption properties). During OAT data acquisition, the US transducer operates in receive-only mode. A 1-Gbit Ethernet connection is used to transmit the optoacoustic pressure signals, received and digitized by a custom-made data acquisition system (Falkenstein Mikrosysteme GmbH, Taufkirchen, Germany) at a sampling rate of 40 MS/s, to a designated PC. Synchronization between the laser, op-

toacoustic signal acquisition and US transmit-receive (TX/RX) electronics is ensured using a laser-triggered control signal from the optoacoustic data acquisition system enabling the US acquisition window. The recorded back-reflected US signals are pre-amplified with a gain of 15.5 dB, time-gain-compensated in the range between -45 to 0 dB as a function of depth, post-amplified with a gain of 24 dB, and digitized by a 12-bit analog-to-digital convertor. The US electronics includes a custom-built 128-channel beamformer (S-Sharp Corporation, Taiwan) with transmit voltage up to 80 Vpp and a variable receive sampling frequency between 18 to 80 MS/s. Voltage, center frequency, and number of cycles in the transmitted pulse are all adjustable parameters. Reconstructed US images are transferred as binary raw data files via Ethernet to the optoacoustic acquisition computer.

4.2.2 Ultrasound transducers

The types of transducers that were considered in the simulations and experiments are schematically depicted in Figs.4.1b-d. We used three concave arrays (Imasonic SaS, Voray, France), custom-designed primarily for whole-body small animal imaging, with central frequency of 5 MHz, nominal TX/RX bandwidth of 60%, angular coverage of 270° and radius of curvature of 40 mm (Fig. 4.1 (d)). Pitch (p) of the individual elements for the 128-, 256-, and 512-element arrays was 1.47, 0.74, and 0.37 mm, respectively. The second type of the concave transducer array (central frequency of 4 MHz) is mainly intended for the handheld operation and has the same radius of curvature but lower angular coverage of 135° containing either 64, 128 or 256 elements, corresponding to the pitch size of 1.47, 0.74 and 0.37 mm, respectively (Fig. 4.1 (c)). The height of the individual elements in the concave arrays is 15 mm whereas the elements are further focused in the elevational direction so that signals are detected from a common imaging plane. Finally, we considered a transducer geometry closely resembling a conventional 128-element US linear array with 0.37 mm pitch size covering approximately 60° angular coverage around the imaged object (Fig. 4.1 (b)). The latter geometry was simulated by reconstructing images with a segment of the 512-element array corresponding to the same angular coverage.

4.2.3 Reflection-mode ultrasound image formation

For generation of the pulse-echo US images, the synthetic transmit aperture (STA) technique was employed, which enables rendering of images of both high quality and frame rate [84,92]. In short, the STA method implies sequential transmission of pulses from each channel while all elements receive the echo signals. In this way, an unfocused rather than directive transmit beam is produced, thus, all pixels are uniformly insonificated by the ultrasound wave. By computing geometric distances from the transmit channel to the focal point and back to the receiving channel, the "round-trip" time delays can be incorporated, thus two-way dynamic focusing accomplished, both in transmit and receive modes. This is in contrast to the conventional "line-by-line" beamforming performed with static focusing in transmit and dynamic focusing in receive. In order to reduce speckle noise and increase contrast and resolution, a spatial compounding technique [135] is subsequently applied across different sub-images corresponding to different sub-apertures. The method implies scanning of the same region from multiple viewing angles and incoherently summing up the resulting sub-images to form the final composite image. Overlap between sub-aperture

areas was set at 3/4 times the individual sub-aperture size. Spatial compounding can provide higher level of artifact reduction and speckle noise suppression. Finally, logarithmic compression is applied to the compounded image and the latter is displayed with gray-level mapping.

4.2.4 OAT image formation

For optoacoustic image reconstruction, the detected pressure signals were first processed with a bandpass filter with lower 0.1 MHz and upper 7.5 MHz cutoff frequencies in order to reject low frequency offsets and reduce high frequency noise. Either filtered backprojection [206] or a semi-analytical interpolated model-matrix inversion algorithm (IMMI) was then employed in order to reconstruct the OAT images [166]. The latter has been previously found to provide more accurate performance in mapping distribution of the optical absorption coefficient in the imaged object by finding an approximation $\hat{x}$ of unknown image **x** via minimization of the sum of squared differences between signals theoretically predicted by model **F** and the pressure signals **p** actually detected by the ultrasound array. An acoustic pressure map that reflects the distribution of absorbed energy is thus calculated via

$$\hat{x} = argmin_x \left\| \mathbf{Fx\text{-}p} \right\|, \tag{4.1}$$

where **F** is the linear operator (or model matrix) mapping the optical absorption to the detected pressure variations. Computational time for generating 200 by 200 pixels US image using STA method is below 100 ms while it takes 6.1 ms and 8.8 s to reconstruct optoacoustic images for the same grid size using the GPU-accelerated filtered backprojection and IMMI algorithms, respectively.

4.2.5 Numerical simulations for image parameters optimization

In order to determine the optimal US image formation strategy for the various concave array geometries, simulations of the US experiments were conducted using Matlab code (MathWorks, Natick, MA). For this, impulse response of the individual transducer elements was employed by further assuming the point source and point receiver approximations. All simulations were done on a desktop computer with Intel Core i7-4820K 3.7-GHz processor and 32-GB RAM. Multi-element concave transducer was simulated as an array of N receivers arranged on the arc of radius R and central angle α with an inter-element spacing (pitch) p. These parameters were related via

$$N = \frac{R \cdot \alpha}{360 \cdot p} 2\pi + 1, \tag{4.2}$$

The transducer was assumed to be located in the XY plane with its axis of symmetry oriented along the positive Y-axis, central element at the origin of coordinates (0,0) and the surface facing the ROI. A computational grid of 271 by 271 pixels (pixel size of 0.15 by 0.15 mm) was used. Sound speed of the surrounding medium was set to 1480 m/s and no additional effects, such as sound diffraction, were considered.

The simulated imaging geometry considered the case of a point reflector whose position was varied within the ROI. In case of the numerical phantom consisting of three point

targets, the individual reflectors were distributed within the field of view and spaced by 20 mm, as shown in the inset in Fig. 4.2 (a). Impulse response of the individual elements was approximated with the cosine function $\cos(2\pi f_c t)$ with probe-dependent center frequency f_c, sampled on the time interval of 2.4 ns with 80 MHz sampling frequency and multiplied by the Hanning function. Excitation pulse consisted of one-cycle cosine waveform, and the final emitted signal was defined as a convolution of the transducer excitation function with the impulse response of the emitting aperture.

In the simulations, the previously described synthetic aperture technique was adopted with each element sequentially emitting ultrasound pulses and other elements receiving the echoes. The simulated data were generated by computing the detected echoes for each pair of transmit-receive channels. Every such signal represents a composite reflected signal from all point scatterers located in the field of view. After forward simulation, a number of steps were applied to process the raw data into a brightness mode (B-mode) ultrasound image. The basic operations include baseband demodulation, receive beamforming, envelope detection, logarithmic compression, and scan conversion. More detailed explanation on each step can be found elsewhere [160].

In simulations with various sub-aperture sizes, the angular span for each individual array segment was changed accordingly, i.e. 90°, 120°, 150°. Reconstructed B-mode images from sub-apertures with up to 75% overlap are then compounded to obtain the final image. Synthesis of the sub-apertures was done using a maximum number of 128 simultaneously available TX/RX channels of the beamformer, resulting in 135° angular span for the 256-element concave transducer. Apertures of larger scale were correspondingly synthesized by using a multiplexing arrangement to connect a new transducer element of the expanded sub-aperture to a specific TX/RX pair. As a result of the dynamic synthetic aperture allocation, array elements at different angular positions can contribute to image formation, which would have otherwise required more than 128 channels to be acquired simultaneously.

4.2.6 Numerical simulations for spatial resolution characterization

The spatial resolution of the system was characterized in numerical simulations and further validated in phantom experiments. The Field II ultrasound simulation program [83] was used with a computational grid of 310 by 310 pixels (0.1 mm pixel size). The speed of sound of the medium was assumed to be constant and set to 1480 m/s. Point absorbers and scatterers (n=961) were placed into the field of view of the array. The concave transducer geometry was constructed from multiple rectangles and bounding lines while the electric impulse response of the transducer was generated assuming a detector center frequency of 4.9 MHz, a bandwidth of 60%, and a sampling frequency of 40 MHz. Pressure fields emitted by all the absorbers were then calculated and the backprojection algorithm was employed to reconstruct the OA images of the numerical phantom. For calculation of the pulse-echo field, excitation pulse was defined as one-cycle cosine waveform, and the final emitted signal was defined as a convolution of the transducer's excitation function with the impulse response of the emitting aperture. All simulated images from the numerical phantom were processed to extract measures of in-plane resolution. For this, the pixels with intensity below 50% from the maximum value in the image were discarded and the maximum distance between remaining pixels was calculated and served as the metric of

in-plane resolution.

4.2.7 Phantoms for characterization of the imaging performance

The tissue-mimicking phantom used is a solid polyurethane-based cylinder (CIRS, VA (USA)) with a diameter of 19.2±0.2 mm and length of 100±0.2 mm. Its acoustic attenuation is approximately 1 dB·cm^{-1}·MHz^{-1} and propagation sound velocity is 1440 m/s. The phantom possesses optical scattering properties close to values found in soft biological tissues. It further contains two ink tubes with diameters of 2 ± 0.2 mm and 5 ± 0.2 mm respectively, symmetrically positioned around the center parallel to the central axis of the cylinder. The inclusions are filled with solution of black ink in order to introduce optical absorption contrast in the phantom. Since the tubes are made of plastic, they are also acoustically scattering, thus expected to have good contrast for both OAT and pulse-echo US.

To obtain the experimental validation measurements we used 90-106 μm diameter black polyethylene (PE) microspheres distributed over the surface of a 30 mm diameter cylindrical agar phantom. Hybrid images were reconstructed using the same set of parameters as in simulations, i.e. 310x310 pixels with 0.1 mm pixel size.

4.2.8 Animal imaging

For the animal *post mortem* experiments, healthy ICR (Imprinting Control Region) albino mice were sacrificed and imaged immediately after, *post mortem*, in order to avoid undesired artifacts due to motion. Hair around the imaged region was removed to avoid strong surface artifacts. The imaging chamber accommodates the fiber bundle arrangement, transducer array and the animal holder. The chamber is filled with water for optimal signal coupling. The holder is designed to place the animal in the horizontal position and lower it into the field of view of the transducer array to allow cross-sectional (two-dimensional) tomographic data detection. The holder surrounds the mouse by a water-impermeable transparent film that averts direct animal contact with water while providing a wide tomographic view of more than 270° around the animal. A linear stage (NRT150, Thorlabs GmbH, Dachau, Germany) allows linear translation of the animal holder along its long axis over a 150-mm range for acquisition of whole-body 3D data sets.

For the animal *in vivo* experiments 10 week old female Hsd:Athymic Nude-Foxn1nu/nu mice were imaged. All procedures involving animal care and experimentation were conducted according to the guidelines of Helmholtz Zentrum Muenchen and the government of Upper Bavaria and complied with German federal and international laws and regulations. The animal was anesthetized with a mixture of 1.8% isoflurane in 100% oxygen at a 0.8 L/min flow rate and introduced into the imaging chamber in the supine position using a specially designed animal holder. Direct contact of the animal with water was averted by using a thin transparent polyethylene membrane. A series of cross-sectional images were subsequently acquired from its anterior to posterior regions with 0.5 mm step size. OA images were acquired at 800 nm, the isosbestic wavelength of hemoglobin.

4.3 Results

4.3.1 Numerical optimization

In order to improve US image quality with concave arrays using the spatial compounding technique, the optimal sub-aperture size, i.e. angular size of the individual sub-images acquired from multiple directions constituting the compounded image, needs to be determined. For this, series of simulations with three point targets were conducted to calculate beam profiles for the different selections of element pitch and sub-aperture angles.

Distribution of the point sources in the field of view of the detector allowed for analysis of the beam profile along the central axis of the array (the central target), as well as in the periphery of the field of view of the detector (the off-axis target). For each beam profile, two quantitative metrics were calculated: peak-to-sidelobe ratio (PSLR) and the full beam width (BW) of the main lobe. PSLR was computed as the ratio between the peak intensities of the side lobe and the main lobe (in decibels), thus reflecting the relation between the useful and undesired signal contributions. Larger values of PSLR imply better contrast in the images. The BW was computed as the distance in millimeters between the -20 dB points on the main lobe. The BW is directly related to lateral resolution, thus a narrower main lobe is desirable for a better resolved image. Fig. 4.2 presents the plots which were used for optimizing the sub-aperture size. The graphs illustrate the trade-off between lateral resolution and magnitude of the side lobes. For instance, by comparing the beam pattern for 90° and 150° sub-apertures for 0.74 mm and 1.47 mm transducer pitch, one observes that using 90° sub-aperture, the beam profile has narrower main lobe but higher side-lobe level. The difference is also noticeable when considering results for the off-axis lateral beam spread (Fig. 4.2 (b)). This particular plot illustrates the importance of the combined analysis of characteristics of the beam directivity pattern at different angles to the transducer central axis. Because the side lobe level elevates toward the edges of the sub-aperture, the sole analysis of the central target beam profile gives a false impression about which sub-aperture (SA) span is optimal. For instance, both SA of 60° and 90° in case of 0.37 mm pitch transducer result in excellent trade-off between PSLR and BW for the central target but, at the same time, leads to one of the highest side lobe level for the off-axis target.

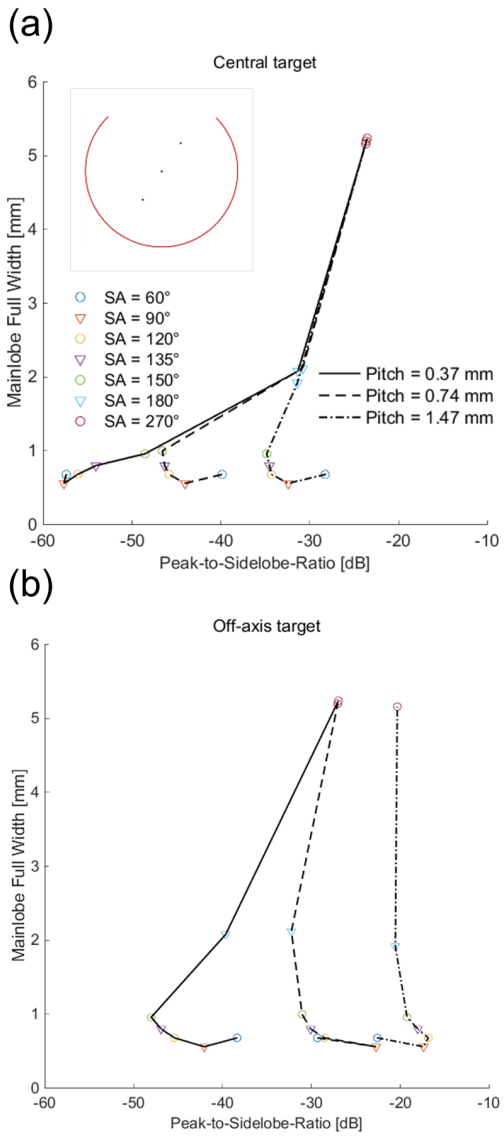

Figure 4.2: The trade-off between two quantitative metrics of the US array beam profile, namely, the peak-to-sidelobe ratio and the main lobe width. Simulations were conducted for the numerical phantom consisting of three point reflectors and arrays with aperture of maximum 270° tomographic coverage, as shown in the inset in panel (a). Results for central (a) and off-axis (b) targets are shown for three different values of the element pitch and variable angular span of the sub-aperture.

As previously mentioned, grating lobes can be further suppressed by applying the spatial compounding technique. Once the size of the optimal sub-aperture has been determined, the next question is how many sub-images should be used and to what extent these are allowed to overlap in order to effectively suppress the noise. Prior work suggests that the choice of the optimal number of individual single-angle images should result from

a compromise between the best lateral resolution and the lowest level of side lobes [11]. An example of simulation conducted for the case of a transducer with 0.74 mm pitch and 256 elements is shown in Fig. 4.3.

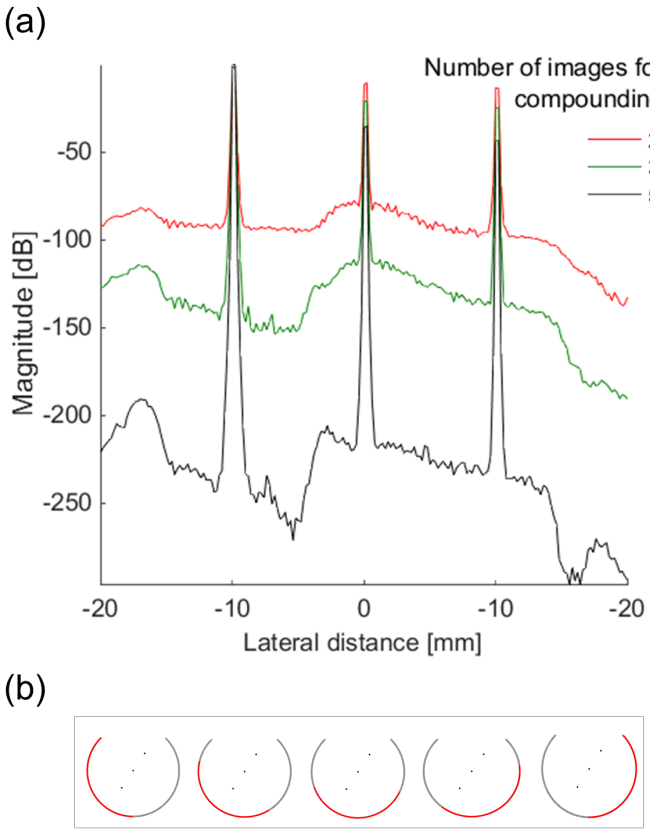

Figure 4.3: Simulation of the beam directivity pattern for three point targets demonstrating the effect of spatial compounding. (a) Example of the lateral beam profile simulated for the 256-elements transducer (0.74 mm pitch) using sub-aperture size of 135° and spatial compounding with 2, 3, and 5 sub-images; (b) Schematics showing 5 sub-apertures for spatial compounding for the case with 5 sub-images (sub-aperture increment of 32 elements).

Clearly, the broad angular coverage of the transducer allows acquisition of more than one sub-image. The resulting beam profiles after the spatial compounding was performed with 2, 3, and 5 sub-images are presented in Fig. 4.3 (a). Using two sub-apertures of 135° with no overlap already leads to notable side lobe suppression by 80 dB or more. Increasing the number of views to 3 results in side lobe suppression of 115 dB. Drastic improvement is achieved with 5 sub-images, or a 32-element increment between subsequent sub-apertures, when the magnitude of the side lobes is lower by at least 190 dB than the main lobe. The schematic in Fig. 4.3 (b) illustrates the exact orientation of the individual sub-apertures that were used for the spatial compounding.

4.3.2 Phantom experiments

Next, the performance of US and OAT was investigated experimentally using the detection arrays with different angular coverage and pitch size. The reconstructed US and OAT images for 6 transducer configurations are shown in Fig. 4.4. All ultrasound images were reconstructed using sub-aperture size inferred from the earlier numerical optimization, namely, 120°, 135°, and 150° for arrays with pitch size of 0.37 mm, 0.74 mm, and 1.47 mm, respectively. In case of concave arrays with 270° angular coverage, the final image was spatially composited from 5 sub-images.

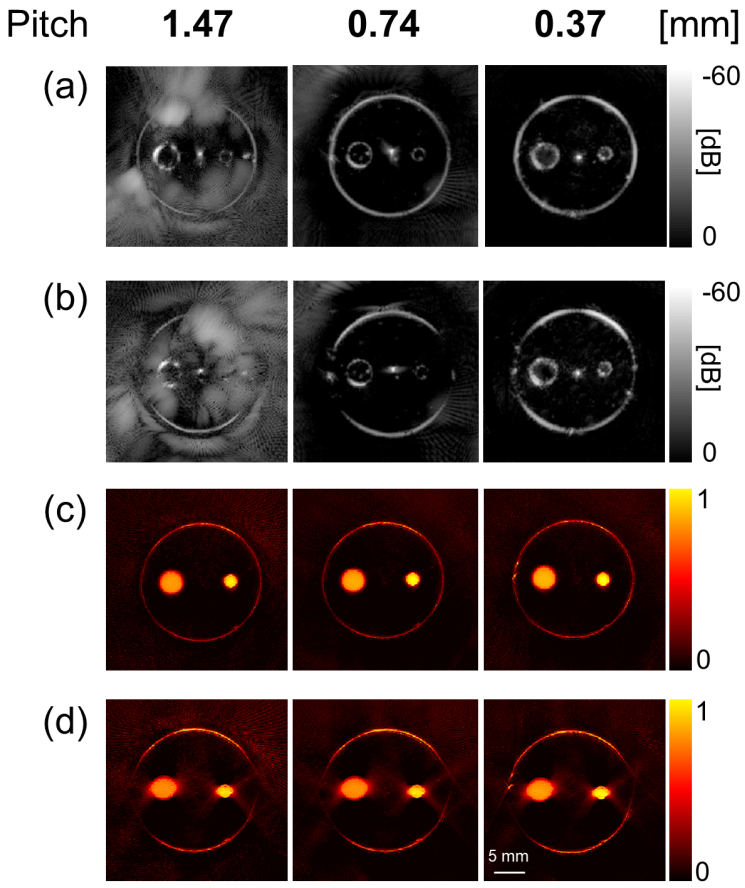

Figure 4.4: US and OAT images for six transducer configurations. (a) US images acquired with transducers having pitch size of 1.47, 0.74, and 0.37 mm and angular coverage of 270°; (b) Same images recorded with angular coverage of 135°; (c) and (d) display OAT images of the phantom acquired with the same sets of transducers as in (a) and (b), respectively.

It can be readily observed that the quality of pulse-echo US images is primarily determined by the pitch size and to less extent by the angular coverage of the transducer. To properly analyze effects of the various parameters on the image quality, the contrast-to-noise-ratio was computed for every image:

$$CNR = |\mu_{ROI1} - \mu_{ROI2}| / \sigma_{ROI2}, \tag{4.3}$$

where μ_{ROI1} denotes the mean intensity of the region containing the ink tube, μ_{ROI2} and σ_{ROI2} are the mean intensity and the standard deviation of the background signal outside the phantom, respectively. Considering different physical origin of the optoacoustic and ultrasound contrast, ROI1 for OAT images was chosen to incorporate the entire cross-section of the light absorbing ink inclusion, whereas ROI1 for US images included only a rim since scattering mainly occurs at the tube boundaries. An estimate of the mean side lobe level was made based on the mean intensity of the background signal.

When comparing Fig. 4.4 (a) and (b), the 50% reduction in the tomographic coverage only resulted in degradation of the CNR by about 13% and increase of about 2 dB in the side lobe levels for all three pitch sizes, as well as incompleteness of side boundaries as it can be seen in Fig. 4.4 (b). On the other hand, doubling the pitch size resulted in image degradation by 7 dB in terms of the side lobe levels and 49% reduction of the CNR. Images in the left column acquired with transducers with pitch of 1.47 mm are all corrupted by a high level of speckle noise and pronounced side-lobe artifacts, which arise due to interfering signals from neighbor elements and manifest in the image as strong reflections outside of the real object location, making these particular configurations unusable for pulse-echo US imaging purposes.

For the OAT images, angular coverage was instead the main factor determining image quality. This follows from the quantitative and visual assessment of images in Fig. 4.4 (c) and (d). Degradation of image quality due to limited tomographic coverage around the field-of-view is manifested in the characteristic horizontal elongation of circular structures, missing boundaries, which hinders correct interpretation of the images. An average drop of CNR due to a two-fold increase in the pitch size was 16% while similar reduction of the angular coverage contributed 26% to the CNR degradation. The combined analysis suggests that considerations of optimizing the pitch size should be prioritized when designing hybrid OPUS imaging systems using concave arrays.

4.3.3 Resolution characterization

Fig. 4.5 (a) shows optoacoustic and ultrasound images of the microspheres covering the entire x-y cross-section of the phantom as well as two magnified regions (4 mm by 4 mm) from the center and the periphery of the field of view. Fig. 4.5 (b) contains the resulting maps of in-plane resolution along x- and y-dimensions obtained in numerical simulations. Plots of in-plane resolution values relative to the distance from the center of the cylindrical array geometry are given in Fig. 4.5 (c) for both the numerical simulations and representative values from the validation experiments. As can be seen, the hybrid system renders in-plane OA resolution in the range of 150-200 μm whereas the corresponding pulse-echo US resolution lies in the range of 340-380 μm. The resolution and sensitivity field of the array remains relatively uniform across a large area of more than 2 cm evinced by the insignificant elongation of the microspheres in the transverse direction.

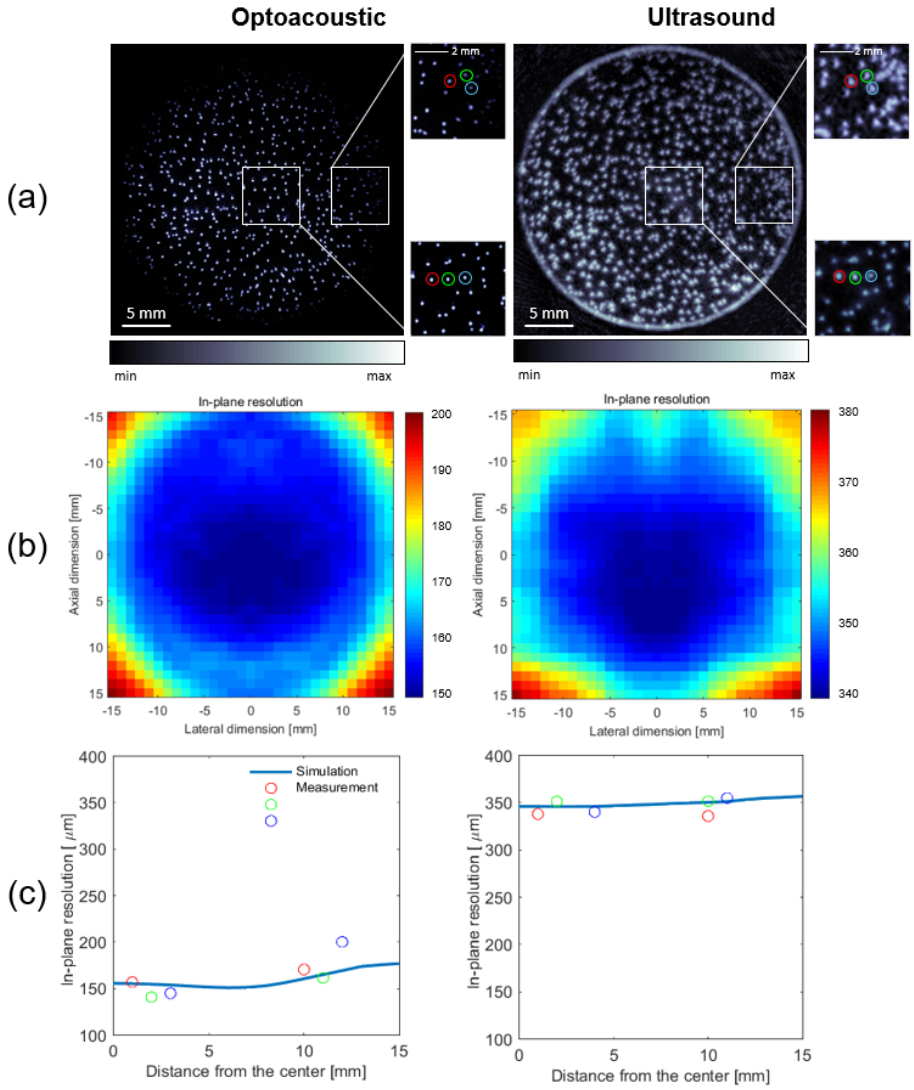

Figure 4.5: System resolution characterization. (a) The reconstructed optoacoustic (left) and ultrasound (right) images of the phantom are shown - two distinctive areas within the field of view magnified; (b) Simulated maps of the spatial resolution within the imaging plane; (c) Comparison between the in-plane resolution obtained in the phantom measurements for the marked microspheres in the center and periphery of the array versus numerical simulations.

4.3.4 Experimental images from biological targets

Next, the reflection mode ultrasound and optoacoustic images were acquired from a mouse *post mortem* using five different array geometries (Fig. 4.6).

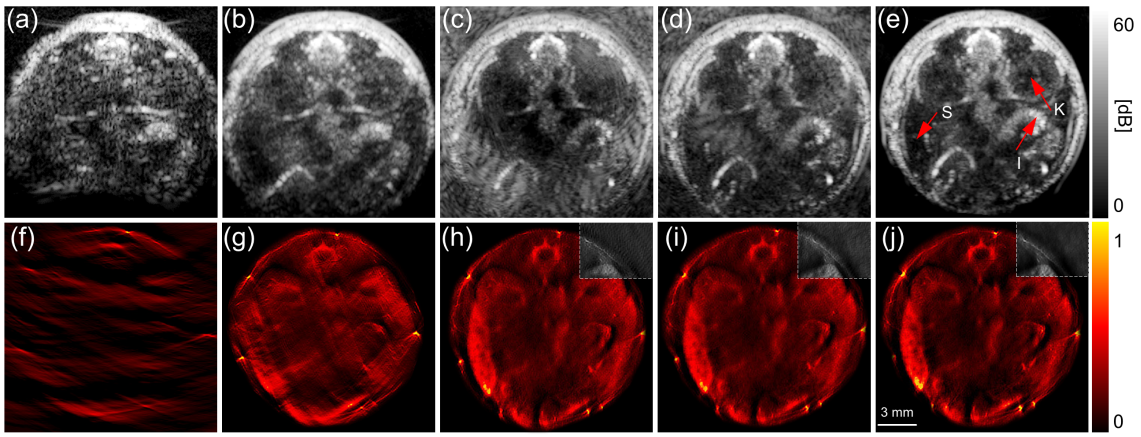

Figure 4.6: OAT and pulse-echo US images from the *post mortem* mouse through the kidney region. K – kidney; S – spleen; I – intestines. (a) US image acquired with a small segment $\sim 60°$ angular coverage) of the 512 element array (0.37 mm pitch), closely resembling the linear array geometry; (b) US image of the mouse acquired with 256-element concave array (0.37 mm pitch) with 135° angular coverage; (c-e) US images of the mouse acquired with concave array with 270° angular coverage and pitch size of 1.47 mm, 0.74 mm, and 0.37 mm, respectively; (f-j) show the corresponding OA images acquired with the same arrays as for (a-e). Small portions of images in panels h-j are presented in gray color scheme with reduced contrast in order to increase visibility of the effects related to the reduced number of elements.

The pulse-echo US images acquired with the concave arrays with 270° angular coverage demonstrate gradual improvement of image quality with an increasing number of elements and thus finer element pitch size. In particular, Fig. 4.6 (e) shows better resolved image with significantly higher contrast and suppressed grating lobes artifacts compared to images in Fig. 4.6 (c) and (d) acquired with the array of 2- and 4-times larger pitch, respectively. In addition, due to the broad tomographic coverage of 270°, these concave arrays were able to evenly visualize the reflection contrast around the entire circumference of the mouse. Although the image acquired with the handheld array having 135° angular coverage (Fig. 4.6 (b)) is not affected by side lobe artifacts owing to its small pitch size, one may notice that some of the boundaries of internal organs have reduced contrast or partially discarded. The configuration resembling a typical linear array probe geometry generally attained inferior image quality (Fig. 4.6 (a)). On the other hand, for the optoacoustic mode, image contrast and overall quality were mostly affected by the tomographic coverage of the array employed. For instance, image quality was totally unacceptable when the data were acquired under the limited-view linear array geometry (Fig. 4.6 (f)). The OAT image quality drastically improved once the tomographic coverage was increased to 135° (Fig. 4.6 (g)), yet superior image quality and contrast are readily achieved when employing arrays with larger angular coverage of 270° (panels h-j). A minor aliasing pattern is observed when acquiring the OAT data with the lower number of 256 and 128 transducer elements (panels h-i) as compared to the case of 512 transducer elements (Fig. 4.6 (j)). Naturally, when the detector elements are distributed more sparsely, the missing information

is manifested in the form of streak artifacts (Fig. 4.6 (h)). Aliasing is one of the fundamental problems in tomographic image reconstruction, which may be caused by either an undersampled grid for displaying the image or due to incomplete tomographic projection data. As a rule of thumb, a well-balanced tomographic image containing N x N pixels should be ideally reconstructed from a total number of approximately N projections [55]. Finally, for an additional demonstration of the image quality, a finger of a healthy volunteer was scanned in a hybrid mode using the 512-element tomographic array for mouse imaging with 270° angular coverage stationary positioned in a water tank. Representative hybrid images are shown in Fig. 4.7. Results of a full volumetric scanning of the finger with the handheld array are further presented in supplementary video 1 accompanying the manuscript. The complementary contrasts of the two modalities are clearly visible since the US images (Fig. 4.7 (a)) emphasize the highly reflecting skin and bone boundaries whereas the OAT contrast mainly stems from the highly absorbing blood vessels (Fig. 4.7 (b)).

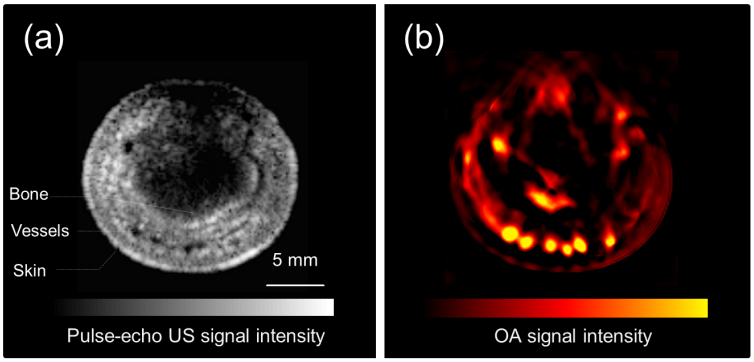

Figure 4.7: OAT and pulse-echo US images of a human proximal interphalangeal joint in transverse plane. (a) Ultrasound image, with indicated anatomical structures, acquired with concave array with 270° angular coverage and pitch size of 0.37 mm; (b) The corresponding OA image acquired with the same array.

4.4 Applications

In vivo imaging performance is demonstrated by label-free hybrid anatomical scans through living mice as well as real-time visualization of optical contrast agent perfusion. By setting new standards for whole-body tomographic imaging performance in both the optoacoustic and pulse-echo ultrasound modes, the developed hybrid imaging approach is expected to benefit numerous applications where the availability of high quality structural information provided by the tomographic reflection-mode ultrasound can ease interpretation of the functional and molecular imaging results attained by the optoacoustic modality.

4.4.1 Imaging of mouse anatomy *in vivo*

Four representative cross-sections are shown in Fig. 4.8, demonstrating the ability to resolve main organs, such as brain, liver, pancreas, and kidneys, in both US (Fig. 4.8 (a)) and

OA (Fig. 4.8 (c)) modes.

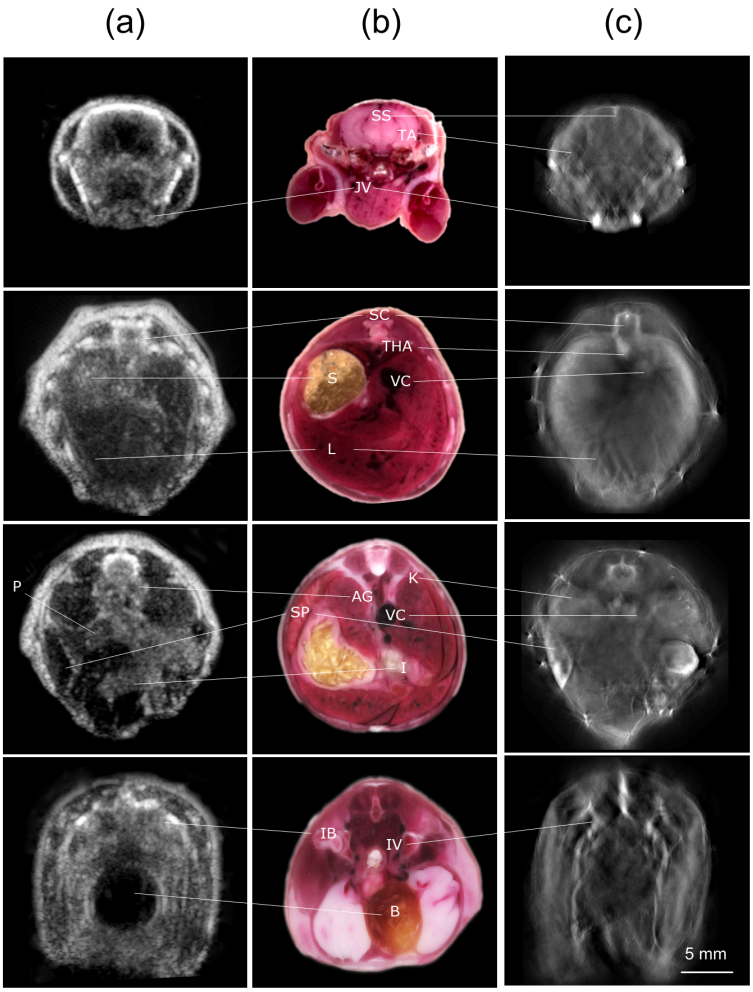

Figure 4.8: Hybrid reflection-mode ultrasound and optoacoustic tomography through the whole mouse. The annotated cross-sections of the ultrasound and optoacoustic images taken *in vivo* are shown in (a) and (c), respectively; (b) Reference macroscopic RGB pictures of cross sections of the frozen mouse taken from approximately the same area. Annotations: SS: saggital sinus; TA: temporal artery; JV: jugular vein SC: spinal cord; THA: thoracic aorta; VC: vena cava; S: stomach; L: liver; AG: adrenal gland; K: kidney; VC: vena cava; P: pancreas; SP: spleen; I: intestines; IB: iliac body; IV: iliac vein; B: bladder.

Notably, US and OA each provide some distinct complementary anatomical features, e.g. the hyperechoic contrast of bones and skin, or the pancreas or the bladder, making them clearly visible in the pulse-echo US images, or the unsurpassed OA contrast from structures highly perfused by the blood, such as the superior sagittal sinus, temporal arteries and jugular veins. Likewise, the thoracic aorta and vena cava generate high OA signals, yet provide anechoic (dark area) appearance in US images. As expected, organs

such as stomach and pancreas produce diffuse reflections and appear grey or hypoechoic in the US images. Tomographic (270°) imaging geometry of the system allows visualizing the entire mouse cross-section, further reducing the limited-view artifacts characteristic of the linear-array probes. For instance, the pancreas is considered to be an elusive organ and its visualization by US has been very challenging due to the complex anatomy of the organ and surrounding tissues [18]. In contrast to imaging with conventional probes, placed in contact with the body and possibly inducing motion, the proposed method facilitates repeatable pancreas detection and reproducible positioning of the animal thanks to non-contact examination. In addition, the broad tomographic coverage allows visualizing the full extent of the organ.

4.4.2 Imaging of perfusion *in vivo*

The synergistic and complementary value of the hybrid imaging system were further demonstrated by acquiring a time series of cross-sectional US and multi-wavelength OA images through the bladder area. The images were acquired during 15 minutes post i.v. injection of 20 nmol of the IRDye-800CW near-infrared optical contrast agent (LI-COR Biotechnology - GmbH, Bad Homburg, Germany). The OA data were acquired at six wavelengths (715, 730, 775, 800, 850, and 900 nm) and averaged 10 times for each wavelength to reduce noise as well as to cope with breathing motion. A small portion of frames with more severe motion was subsequently discarded from the analysis using a metric of mutual information as similarity between all the acquired frames and the reference static frame to detect the most deviating images. Spectral un-mixing of the images was done using independent component analysis (ICA) [62] and the unmixed component corresponding to the IRDye-800CW signal was superimposed over the simultaneously acquired US and single wavelength (760 nm) OA images (Fig. 4.9).

The experiment shows that the US images allow for clear identification of the anechoic bladder otherwise invisible in the single–wavelength OA images prior to the injection. The dye uptake by the bladder reflects glomerular filtration and excretion, therefore the measurements in the vicinity of the center of the bladder directly enable functional analysis of the kidney function and were previously challenging due to insufficient contrast of stand-alone optoacoustic imaging.

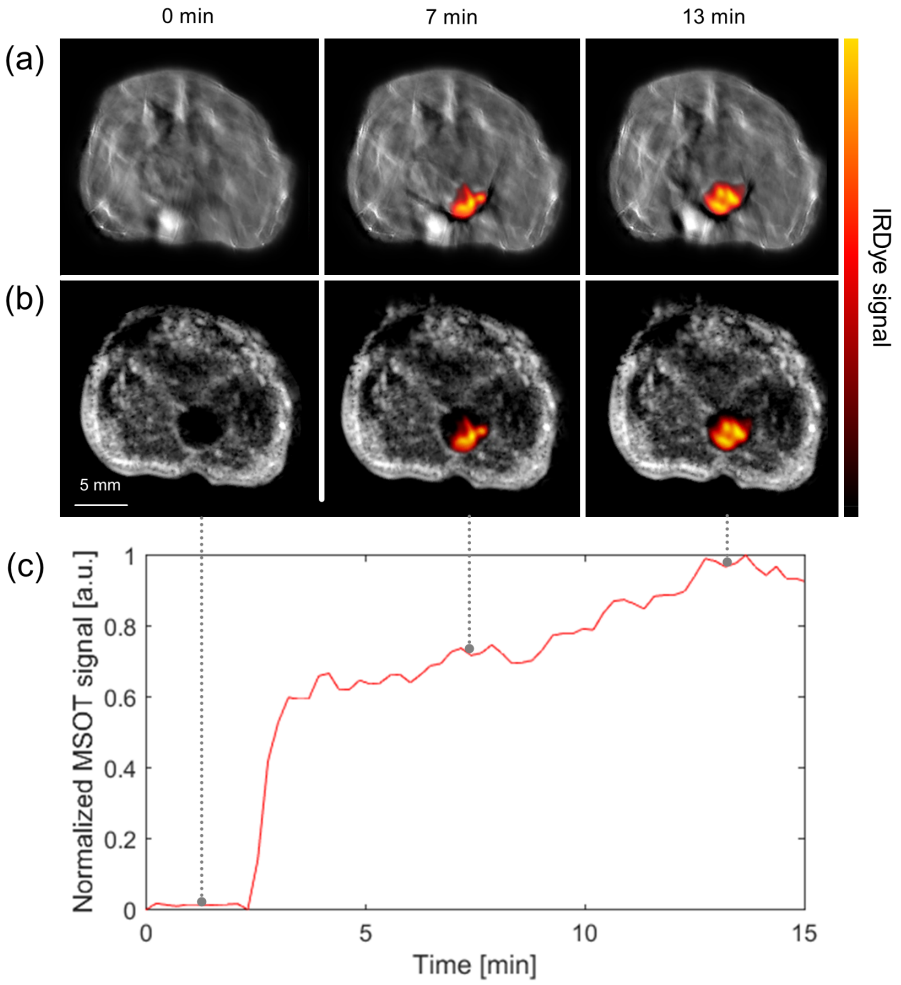

Figure 4.9: Imaging of longitudinal uptake of near-infrared dye by the bladder. (a) OA images of dye distribution at 0, 7, and 13 minutes after injection. Unmixed IRDye-800CW distribution is overlaid over the single wavelength OA image of the imaged mouse cross-section; (b) The same unmixed dye distribution superimposed onto the US image; (c) Normalized mean signal traces of the dye in the bladder.

4.5 Discussion

In this chapter we have analyzed the applicability of combined US and OAT from a technical perspective and provided insights into key design parameters and their effect on performance of both modalities. Furthermore, a hybrid OPUS system has been proposed employing for the first time concave array geometry with large tomographic coverage for real-time imaging in both pulse-echo US and OAT modes. In the current study, the image acquisition and rendering was performed at a rate of 10 Hz, limited by the laser pulse frequency, but higher imaging rates are generally possible.

Measurements conducted with various array geometries revealed high relevance of

pitch size and tomographic coverage in achieving accurate hybrid imaging performance. An additional strategy of improving spatial resolution and depth of field in US imaging mode was proposed that uses advanced beamforming method for image formation. The synthetic transmit aperture (STA) technique comprises a more effective approach in terms of the resulting CNR and achievable frame rate as compared to the "line-by-line" beamforming approach. To adapt STA for concave arrays, optimal sub-aperture size for each type of array was selected by means of numerical simulations based on the trade-offs in main lobe width and the side lobes amplitude. In order to further improve image quality and reduce speckle noise, spatial compounding was performed with optimized overlap between subsequent sub-apertures.

The concave array geometry successfully employed in the current study for imaging in pulse-echo US mode creates the opportunity of including also the transmission ultrasound imaging capability, which can simultaneously provide maps of distribution of speed of sound and acoustic attenuation in the object [90]. This particular aspect is addressed in Chapter 6.

The hybrid imaging capabilities show promise to ease interpretation of the OA images by providing high reflection contrast from different internal organs, some of which, such as the pancreas and bladder, are not clearly visible in the OA images. The multispectral imaging capacity of the system in the OA mode further provides the ability to visualize contrast agents and functional blood parameters. Thus, the complementary contrasts of the two modalities may expand the applicability of the developed hybrid imaging approach into a wide range of applications, such as cardiovascular and tumor biology, studies of pharmacokinetics, organ metabolism, and neuroimaging.

5 Multi-Segment Detector Array for Handheld Hybrid Optoacoustic and Ultrasound Imaging

5.1 Introduction

The use of multispectral optoacoustic tomography (MSOT) as a powerful functional and molecular imaging tool has increased exponentially over the last years, both in routine small animal research [137] and precision clinical diagnostics [177]. Hybridization is expected to further enhance the performance of MSOT with ultrasonography (US) appearing to be the natural partner as it also uses acoustically-detected signals for image formation. Such hybrid solution becomes particularly important for the clinical acceptance of MSOT since physicians are well accustomed to the use of US in clinical diagnostics. Yet, due to the fundamentally different physical contrast and image formation mechanisms, the development of detection technology optimally suited for image acquisition in both modalities remains a major challenge.

in this chapter, we introduce a multi-segment detector array approach incorporating array segments of linear and concave geometry to optimally support both ultrasound and optoacoustic image acquisition. The various image rendering strategies are tested and optimized in numerical simulations and calibrated tissue-mimicking phantom experiments. We subsequently demonstrate real-time hybrid optoacoustic ultrasound (OPUS) image acquisition in a healthy volunteer. The new approach enables the acquisition of high-quality anatomical data by both modalities complemented by functional information on blood oxygenation status provided by the multispectral optoacoustic tomography.

The experimental performance of the multimodal approach is further showcased by imaging the carotid artery region of a healthy volunteer, where Doppler US is commonly used for the detection of vascular abnormalities, such as stenosis or intraluminal turbulence [4].

5.2 Materials and methods

5.2.1 Experimental system

Key instrumentation aspects and algorithmic strategies employed in the hybrid OPUS system are described in Chapter 3. Here we remind the reader and repeat some of the description for completeness.

The main components of the hybrid OPUS system are schematically depicted in Fig. 5.1 (a).

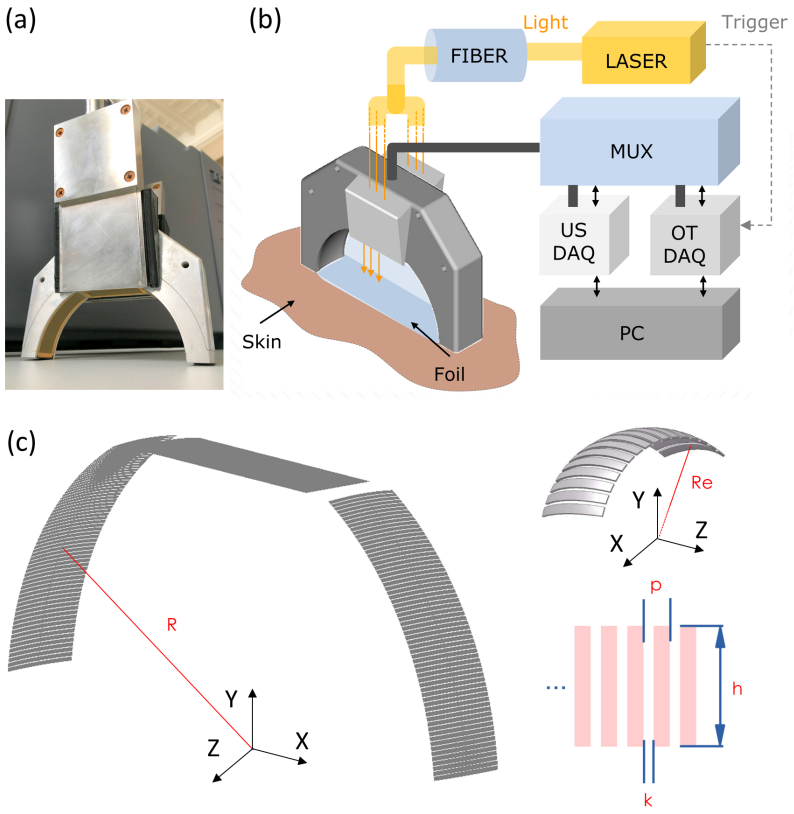

Figure 5.1: Components of the hybrid optoacoustic-ultrasound tomography (OPUS) imaging system. (a) Photograph of the multi-segment handheld detector array; (b) Block diagram illustrating functional components of the system; (c) 3D rendering of the multi-segment array with geometric characteristics of the detector marked in red. R – radius of the concave array geometry, p – inter-element pitch, h – element height, k - inter-element spacing, Re – radius of curvature.

For the OA signal excitation, light from the pulsed Nd:YAG-pumped optical parameter oscillator (OPO) laser (InnoLas Laser GmbH, Krailling, Germany) is guided to the specimen via a custom-made fiber bundle (CeramOptec GmbH, Bonn, Germany) with total number of approximately 893 fibers equally split between two output ferrules made of stainless steel, each having fiber output surface with dimensions of 40 mm by 0.6 mm. The outputs of the two ferrules are attached to the lateral sides of the array and oriented at a $\sim 17°$ angle so that the two illuminating beams intersect the cross-sectional imaging plane roughly at the tissue surface. The rationale for providing the illumination at the central part of the linear array was mainly driven by usability considerations in hand-held imaging of human subjects. For optimal acoustic coupling, the array cavity was filled with de-ionized water and sealed using acoustically and optically transparent foil, as shown in Fig. 5.1 (a).

The laser source operates at 25 Hz repetition rate, with the per-pulse energy output set to 25 mJ, pulse duration of ~ 9 ns and a tunable wavelength range of 680 to 980 nm. The beam profile at the tissue surface had an ellipsoidal shape with dimensions of 45 mm (long axis)

x 32 mm (short axis) and the incident fluence at 730 nm was estimated at 1 mJ/cm^2, which is below the ANSI recommended maximum permissible exposure limits (23 mJ/cm^2 for 730 nm pulsed laser with pulse duration range of 1 to 100 ns [1]).

The OA signals collected by the array probe are digitized by a custom-made data acquisition system (Falkenstein Mikrosysteme GmbH, Taufkirchen, Germany) at a sampling rate of 40 MS/s. The signals are subsequently transferred to a designated PC station using a 1-Gbit Ethernet connection. Image reconstruction is performed at the PC. During OA data acquisition, the probe operates in receive-only mode.

Switching between OA and US imaging modes is facilitated through a custom-made a programmable multiplexing control unit (MUX) connected to the transducer array. A laser-triggered signal from the OA data acquisition system (OA DAQ) controls transition of the MUX state from "receive-only" for OA imaging to "transmit-receive" for B-mode US imaging, thus ensuring the synchronization of the two data streams. In this way, any possible acquisition conflict is avoided by allocating strictly defined non-overlapping time windows for the OA and US data recording and processing. Moreover, frame time-stamping enables clearly differentiating the incoming data streams from the different modalities. Only the latest frames with the closest time stamps are overlaid for the multimodal representation. Fig. 5.2 schematically describes the timeline of the interleaved OA and US acquisition. The time window between two consecutive laser pulses (40 ms at 25 Hz repetition rate) is divided into two segments. The first 5 ms are allotted to OA acquisition, where simultaneous reception (Rx) of the optoacoustically-induced signals on all 256 channels followed by tomographic reconstruction using the GPU-accelerated filtered backprojection [206] yields one OA image frame. The pulse-echo US image acquisition is executed by a custom-built US data acquisition system (US DAQ) having 128 transmit/receive channels (S-Sharp Corporation, Taiwan), 12-bit vertical resolution, 10 MHz input bandwidth, and 20 MS/s sampling rate. A transmission (TX) event of a single-cycle bipolar pulse (20 Vpp, 8 MHz) from a single channel of the linear part of the array and simultaneous recording of the reflected ultrasound signals on the 128 elements of this array segment yield one low-resolution (LR) image. The final high-resolution image (HR) is generated by coherent summation of many LR images from all 128 subsequent transmission events using a synthetic aperture imaging scheme [92]. The GPU-accelerated reconstruction of pulse-echo US images is performed on the US DAQ system with the subsequent transfer of the reconstructed images as binary raw data files via Ethernet to the PC.

Two basic operation modes are enabled by the acquisition hardware, namely, (1) interleaved MSOT and pulse-echo US by means of synthetic transmit aperture (STA) beamforming or (2) interleaved MSOT and duplex US (color Doppler combined with pulse-echo US) by means of dynamic receive focusing (DRF) beamforming, also known as B-scan mode. Switching between the two modes is performed manually.

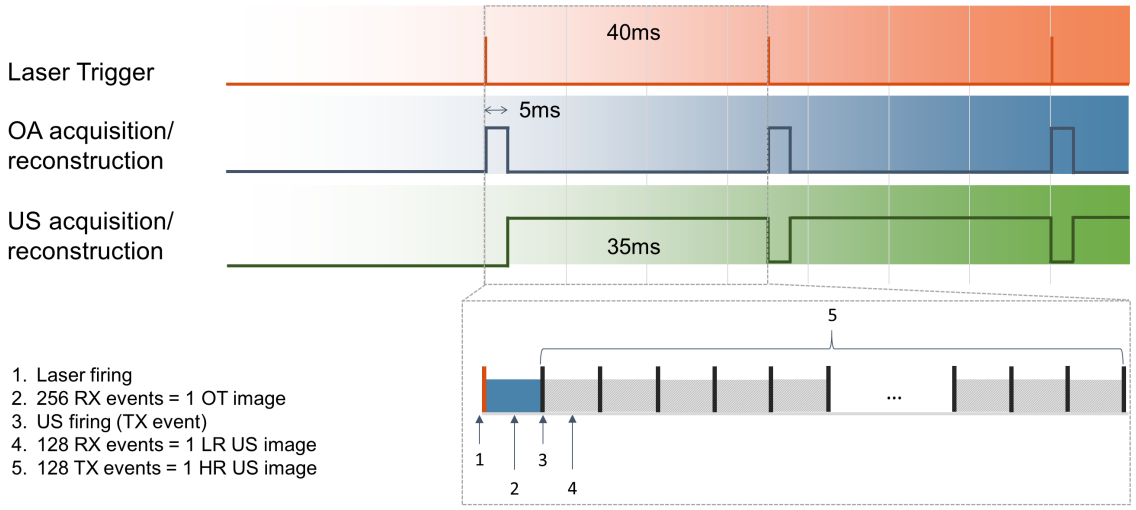

Figure 5.2: Timing diagram of interleaved OPUS image acquisition

5.2.2 Multi-segment detection array

The ultrasound transducer array employed in this study was custom-designed (Imasonic SaS, Voray, France) and is schematically depicted in Fig. 5.1. It combines two detector geometries, the linear segment consisting of 128 elements with 0.25 mm inter-element pitch and 10 mm height. Cylindrical focusing on the elevational axis (focal distance - 34 mm) was achieved by bending the active array surface. Attached to the linear part are two concave segments, each having 64 cylindrically-focused elements with 0.6 mm inter-element pitch, 10 mm height, and a focal distance of 38 mm. The radius of curvature for the concave part in the x-y plane was selected to be 40 mm so that the combined angular coverage of the multi-segment array constitutes 170°, which represents a convenient trade-off between broad optoacoustic angular coverage and usability of the array for hand-held applications. All elements have a central frequency of 7.5 MHz and nominal TX/RX bandwidth of 60%. The geometric characteristics of the array elements are summarized in Table 5.1.

Table 5.1: Geometric characteristics of the elements on the central (linear) and external (concave) segments of the detector.

	Center (linear) segment	External (concave) segments
Element pitch (p) [mm]	0.25	0.6
Element height (h) [mm]	10	10
Inter-element spacing (k) [mm]	0.05	0.1
Radius of curvature in x-y plane (R) [mm]	∞	40
Radius of curvature on z axis (Re) [mm]	34	38

5.2.3 Numerical simulations

Numerical simulations were conducted by means of the Field II ultrasound simulation software [83] to characterize the effective field of view of the multi-segment array for OA and US modes. The program calculates the spatial impulse response (SIR) of an arbitrary shaped transducer by dividing the surface of the transducer into small sub-apertures. Specifically, the transducer aperture was modelled from multiple rectangles and bounding lines with each single element simulated by a matrix of 495 rectangles arranged in 3D space on a spherical (concave segments) or cylindrical (linear segment) surface. The electric impulse response of the transducer was simulated using a 2D Gaussian function assuming a detector center frequency of 7.5 MHz, a bandwidth of 60%, and a sampling frequency of 40 MS/s. As imaging targets, 961 points were placed in the field of view of the transducer equally spaced by 1mm in the x- and y-direction. The OA field of view was characterized as described in [83]. The pressure fields received by each detection element were estimated following a discrete delta function excitation at the 961 positions of point sources subsequently convolved with the electrical impulse response of the transducer. A computational grid of 310 by 310 pixels (0.1 mm pixel size) was used for OA reconstruction of point targets. The speed of sound of the surrounding medium was set to 1480 m/s. On the other hand, for effective estimation of the US field of view, the excitation pulse was defined as a single-cycle bipolar waveform, and the final transmitted signal was determined as a convolution of the excitation function with the impulse response of the transducer. The generated acoustic data frame had a size of $2030 \times 128 \times 128$ where each signal consisting of 2030 samples represents a composite reflected signal from all point scatterers located in the field of view for each pair of transmit-receive channels. After forward simulation of the acoustic data, a synthetic transmit aperture (STA) technique was used for reconstruction of an US image [92]. The latter creates a high-resolution image by coherently combining many low-resolution images whereas one low-resolution image corresponds to one transmit event from a single channel while recording the resulting echoes on all elements, and can be reconstructed using standard delay-and-sum algorithm based on a time of flight calculation.

In both OA and US modes, the resulting images of the grid of point sources were processed to extract metrics of in-plane sensitivity field. For this, the ratio of pixel intensity to the maximum value of pixel intensity in the image was computed on a per-pixel basis. The effective field of view was then defined as the region where the sensitivity remains above 50% of its maximum. All simulations were done in Matlab (MathWorks, Natick, MA) on a laptop computer with Intel Core i5-2410 2.3-GHz processor and 4-GB RAM.

5.2.4 MSOT imaging

For OA image formation, the time-resolved optoacoustic pressure transients detected with all 256 transducer elements were used. The acquired signals were first pre-processed with a bandpass finite impulse response (FIR) filter (0.05 and 10 MHz cutoff frequencies) and deconvolved with the electrical impulse response of the transducer used in the simulations. Two-dimensional OA images were eventually reconstructed with a standard back-projection algorithm [206].

For spectral unmixing, the OA images were acquired at seven wavelengths (700, 730, 760, 780, 800, 825, and 850 nm) in order to accurately sample the absorption spectrum profiles of the endogenous chromophores of interest. To minimize the negative effect of motion on the unmixing accuracy, the probe was kept still during acquisition of the multi-wavelength data. Alternatively, motion artefacts in multispectral imaging can be effectively averted by using microsecond-delayed triggering of multiple lasers [26], which was however not attempted in the current study. The distributions of oxy- and deoxy-hemoglobin were subsequently rendered by means of spectral fitting of unaveraged single-wavelength images to the known absorption spectra of oxy- and deoxy-hemoglobin [194], and the resulting 2D maps of the specific chromophore distribution were visualized using pseudo-color coding. This type of visualization does not permit quantitative evaluation of blood oxygen saturation but rather intended for visualizing the distribution of oxy- and deoxy-hemoglobin.

5.2.5 Pulse-echo STA US and duplex US image acquisition

In the pulse-echo US mode, single-cycle 20 Vpp bipolar pulses at 7 MHz frequency were transmitted. The 128 elements of the linear array segment were used for US image formation by employing a synthetic transmit aperture (STA) focusing technique [92]. The concave parts of the array were not considered for US image formation as those would introduce grating-lobe artefacts associated to the large inter-element pitch of the concave segments [131]. The method is realized by sequential pulse transmission from individual elements and detection of the back-scattered echoes with all the array elements. The sampled channels are then stored to build 128 low-resolution images (LRIs) corresponding to each event of an unfocused emission of an ultrasonic pulse from a single element and acquisition of the resulting echoes by all the other elements. The LRIs are formed using delay-and-sum (DAS) beamforming within a defined FOV with a pixel size of 150 μm. The LRIs from subsequent transmit events are coherently summed to form a final high-resolution image (HRI). The LRIs add up at points where the isochronal lines, i.e. those connecting pixels with the same time of flight, overlap on a real scatterer. At other locations, the individual images add incoherently resulting in a much lower signal level. In

this way, the STA algorithm synthetically focuses both the transmitted and back-scattered fields throughout the entire image. In our experiments, the synthetically focused beam intervals were set to 200 μm.

In the duplex US imaging mode, a two-dimensional B-scan image is rendered by pulse-echo interrogation of multiple scan lines swept across the FOV using dynamic receive focusing (DRF) type of beamforming. As opposed to STA, in DRF only the back-scattered field is dynamically focused at all points across the FOV while the focus of the transmitted field remains steady [[82, 193]. Similarly to B-scan pulse-echo image, the color flow map is then generated by multi-gated interrogation of the multiple scan lines using bursts of short US pulses [126]. In this way, many RF back-scattered signals are obtained at multiple sampling sites (gates) along each scan line for a series of emitted US pulses. The group of pulses required to estimate the velocity of blood flow at a particular gate is known as a packet or a pulse train with the time between successive pulse trains determining the effective pulse repetition frequency (PRF) [154]. In our experiments, packet size of 8, PRF of 5 kHz, and 5-cycle 20 Vpp bipolar pulses at 6 MHz frequency was employed. The transmitted field was focused at an approximate depth of 1.5 cm from the tissue surface and the aperture size was varied by means of dynamic apodization [209] to achieve a constant F-number of 2, both in transmit and receive modes. The beam intervals for the color Doppler flow image are set to 300 μm. The frequency shift measured at each gate is automatically correlated using an autocorrelation function and encoded in the image via a preset color scheme with positive Doppler shifts (blood moving towards the transducer) represented by red colors and negative shifts represented by blue colors [149]. The color-coded flow patterns are subsequently superimposed onto the gray-scale anatomical B-scan image [126]. Rendering of two-dimensional 200x200 pixels B-mode US images was performed in real time at a rate of 25 frames per second, while the frame rate in the color Doppler mode was 10 Hz. The latter can be calculated via [94]

$$FPS_{DP} = \frac{1}{\frac{NL_B}{PRF} + \frac{NL_C \cdot PS}{PRF}}, \tag{5.1}$$

where NL_B is the number of lines in the reconstructed B-mode image; NL_C is the number of lines in the reconstructed color Doppler-mode image; PRF is the pulse repetition frequency [Hz] and PS is the packet size. Clearly, the frame rate can be increased by using larger pixels or, alternatively, by reducing the packet size.

5.2.6 Phantoms for resolution characterization

A non-scattering agar-based (2% w/v) cylindrical phantom of 50mm height and 20mm diameter was used for resolution characterization of the multi-segment array. A 90-106µm diameter black polyethylene (PE) absorbing microsphere (Cospheric LLC, USA) was centrally positioned on top of the cylinder and illuminated from one side using a fiber bundle. The array was fixed to the mechanical stage and aligned under optoacoustic guidance such that the microsphere is positioned in the central point of the concave detector geometry. For in-plane resolution characterization, the array was translated along X- and Y-axes to collect measurements at positions $\pm$5 mm and $\pm$10 mm from the center of the concave array geometry. For the elevational (out-of-plane) resolution characterization, the array was translated along the Z-axis with a step size of 200 μm. Images were reconstructed using the

same set of parameters as in the numerical simulations described in section 5.2.3, i.e. 310 × 310 pixels with 0.1 mm pixel size. By analyzing the image of the microsphere at each individual position, metrics of the in-plane axial and lateral resolution were extracted as the full width at half maximum of the image profile along x- (FWHMx) or y-axis (FWHMy), respectively. The elevational (out-of-plane) resolution was estimated by fitting a Gaussian model to the signal profile along the Z-axis and taking its full width at half maximum (FWHM).

5.2.7 *In vivo* imaging of a healthy volunteer

The *in vivo* imaging performance of the proposed OPUS system was demonstrated by slowly scanning the probe along the wrist of a healthy volunteer in a hybrid mode. The reconstructed field of view was 30 mm × 30 mm with a pixel size of 0.1 mm. Distribution of endogenous oxy- and deoxy-haemoglobin were unmixed using spectral fitting [194] and the result was visualized as a composite image with the specific chromophore distribution superimposed in color over the structural background provided by the ultrasound image.

For image acquisition in a carotid region, a healthy volunteer was lying in a supine position with a stretched neck and the chin turned away from the side being examined. For optimal scanning we referred to the standard guidelines for carotid US examinations [181]. The probe was placed on the left side of the lower neck and the scan in the transverse plane was first performed along the common carotid artery slowly moving into the carotid bifurcation area (Fig. 5.3 (a)). After identifying the internal and external carotid arteries, the probe was kept still to minimize motion artifacts during the MSOT image acquisition. The probe was then slowly rotated 90° and a scan in the longitudinal plane was performed to better visualize the common carotid artery and the bifurcation area (Fig. 5.3 (b)).

All human imaging experiments were done in full accordance with the work safety regulations [80].

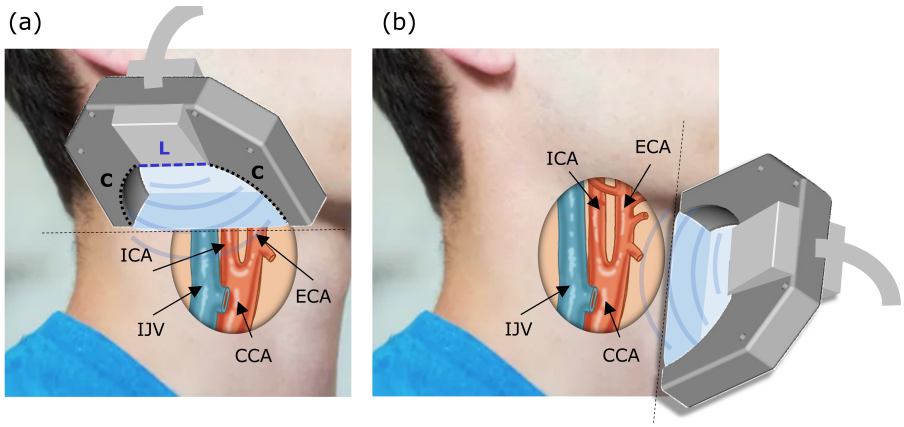

Figure 5.3: Geometry of the multimodal (MSOT, pulse-echo US, and color Doppler) image acquisition with the multi-segment probe in (a) transverse and (b) longitudinal planes. ICA: internal carotid artery; ECA: external carotid artery; IJV: internal jugular vein; CCA: common carotid artery.

5.3 Results

5.3.1 Simulations

Numerical simulation results are shown in Fig. 5.4. Fig. 5.4 (a) illustrates the relative detector position with respect to a regular grid of point sources distributed within the field of view of 31 mm $\times$ 31 mm with equal spacing of 0.1 mm. Negative values in the reconstructed images were discarded by setting them to zero followed by normalization of optoacoustic and ultrasound images between 0 and 1 (Fig. 5.4 (b), (d)).

The metric of sensitivity was subsequently calculated for each individual grid point as a ratio of maximum pixel intensity of the respective grid point to the to the maximum value of pixel intensity in the whole image. The resulting sensitivity maps consisting of 31 $\times$ 31 discrete points were then interpolated (upsampled) by a factor of 10 for smoother visualization while additional 50% intensity contours were added to the maps (Fig. 5.4 (c), (e)). Such characterization of the sensitivity field of the detector by means of numerical simulation allows for quantitative assessment of the effective field of view in both imaging modes. Fig. 5.4 (c) suggests that the field of view in optoacoustic mode along x- and y-dimensions is around 30 mm $\times$ 25 mm whereas a field of view larger than 30 mm $\times$ 30 mm is estimated for the ultrasound imaging mode (Fig. 5.4 (e)). Note, however, that all 256 array elements were used for rendering the optoacoustic reconstructions whereas only the 128 elements of the linear array segment were employed for the pulse-echo ultrasound imaging simulations.

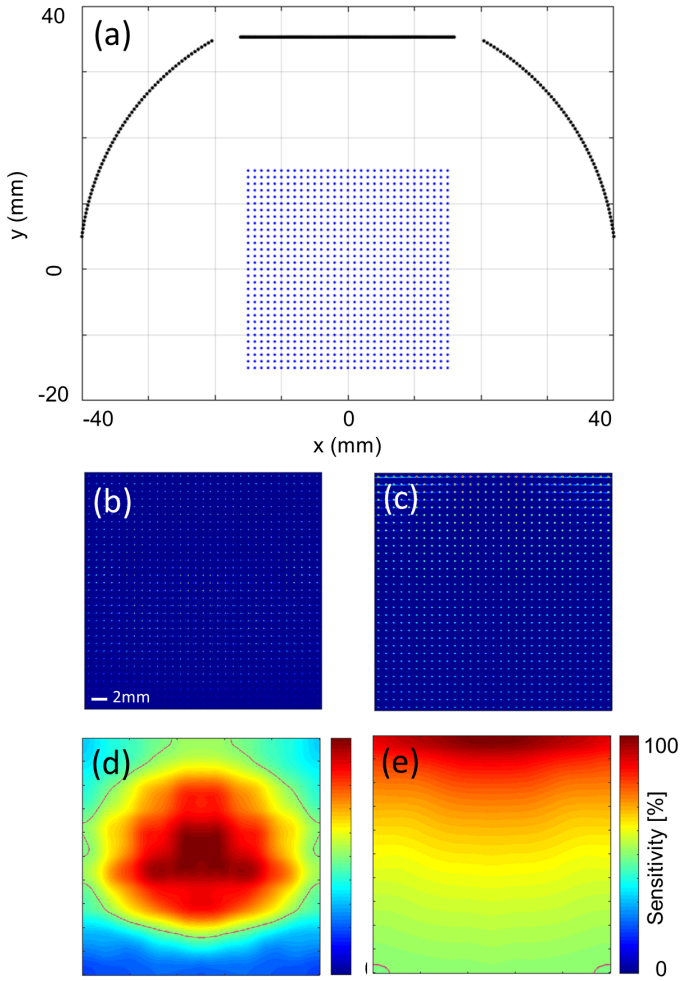

Figure 5.4: Characterization of the multi-segment array field of view. (a) Schematics of the detector geometry and the measurement points used in numerical simulation. The simulated optoacoustic and ultrasound reconstructions of the grid of point sources are shown in (b) and (c), respectively. (d) and (e) Simulated sensitivity maps within the imaging plane for the respective optoacoustic and ultrasound modes.

5.3.2 Resolution characterization

Quantitative experimental assessment of the spatial resolution performance is presented in Fig. 5.5. The OA resolution is characterized in Fig. 5.5 (a-h) whereas the corresponding US resolution is described in Fig. 5.5 (i-l).

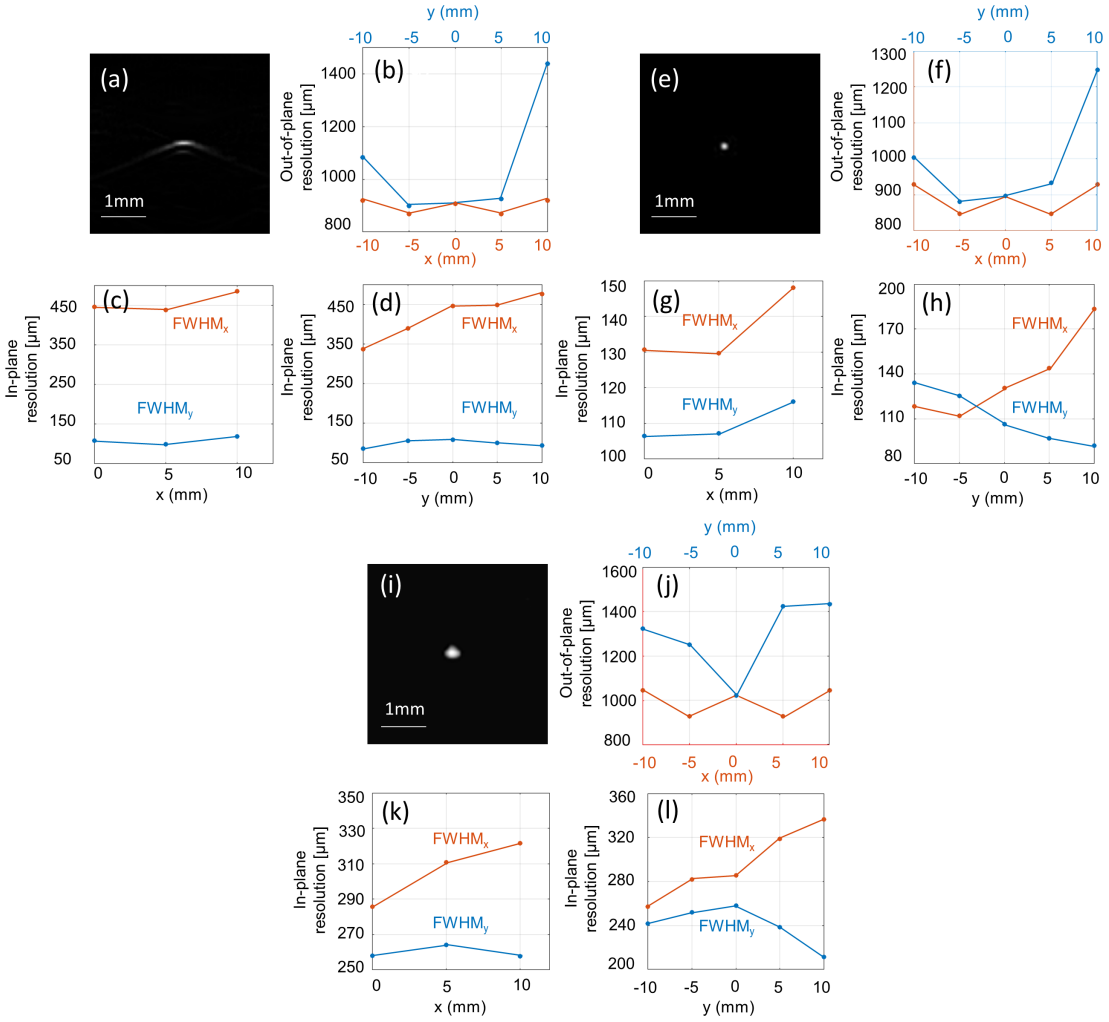

Figure 5.5: Experimental resolution characterization. (a) and (e) Optoacoustic MIP images for the microsphere at scanned position (x,y) = (0,0) reconstructed using central array segment and all 256 elements, respectively; (i) Ultrasound MIP image for the microsphere at scanned position (x,y) = (0,0) reconstructed using central array segment; (b) ,(f) and (j) Out-of-plane resolution for all scanned positions along x- (red) and y-dimensions (blue) for optoacoustic and ultrasound modes, respectively; (c),(g) and (k) Axial (FWHMy) and lateral (FWHMx) in-plane resolution for all scanned positions along x-axis for optoacoustic and ultrasound modes, respectively; (d),(h) and (l) Axial (FWHMy) and lateral (FWHMx) in-plane resolution for all scanned positions along y-axis for optoacoustic and ultrasound modes, respectively.

The maximal intensity projection (along z-axis) of the actual OA and US images of the microsphere at the scanned position (x,y) = (0,0) are shown in Fig. 5.5 (a), (e),and (i), respectively. Fig. 5.5 (a), (e) correspond to OA images reconstructed using central array segment (128 elements) and all 256 elements, respectively. When all 256 elements are used for reconstruction, namely, including the outer concave segments, the estimated OA in-

plane axial and lateral resolutions are within the range of 90 to 130 μm and 110 to 180 μm (Fig. 5.5 (q), (h)) for a field of view of at least 2 cm $\times$ 2 cm. The lateral resolution is significantly worsened when only central array segment is used for the reconstruction (Fig. 5.5 (c), (d)). The estimated OA in-plane axial and lateral resolutions in this case are within the range of 90 to 120 μm and 340 to 480 μm, respectively. Corresponding US in-plane resolution along axial and lateral dimensions was estimated between 210 and 260 μm, and 260 and 340 µm (Fig. 5.5 (k), (l)), respectively. The out-of-plane OA resolution (along the elevational z direction) was then estimated as FWHM of the maximum intensity values of the reconstructed images of the microsphere at the scanned positions. For the reconstruction solely based on the linear array segment, it was found to be in the 850 to 1250 μm range within the analyzed 2 cm $\times$ 2 cm field of view (Fig. 5.5 (b)). The respective out-of-plane OA resolution for the reconstructions using all the 256 elements was in the 870 to 1440 μm range (Fig. 5.5 (f)). The estimated out-of-plane resolution for US mode was within 930 to 1430 μm range.

5.3.3 Imaging of a healthy volunteer

The advantages of the proposed design for hybrid OPUS imaging can be best appreciated by comparing the OA and US images of the wrist made with various combinations of the array segments, as shown in Fig. 5.6 (a-d). For providing an additional comparison, the same region of interest was scanned in the hybrid OPUS mode using 256-element concave array with the same radius of curvature of 40 mm and angular coverage of 170° but having a uniform inter-element pitch of 0.47 mm across of its elements. It can be readily noticed that the OA image contrast and overall quality are mostly affected by the tomographic coverage of the array. Indeed, while the image reconstructed by employing all the array segments displays the correct round appearance of the radial veins and arteries (Fig. 5.6 (a)), the image quality is drastically degraded when using solely the limited-view data acquired by the 128 elements of the linear array segment (Fig. 5.6 (c)), in which the vessel shape is completely distorted. OA image obtained with the concave detector having a uniform pitch confirms the importance of angular coverage for the OA reconstructions by rendering superior OA image quality (Fig. 5.6 (e)) as compared with the linear array reconstructions in Fig. 5.6 (c). On the other hand, the quality of the pulse-echo images is in fact significantly deteriorated when adding the concave array segments, featuring large inter-element pitch, to the image reconstruction process. The US image acquired by using all the 256 array elements exhibits a higher level of artifacts associated to grating lobes and reduced contrast (Fig. 5.6 (b)) as compared with the image rendered solely by the linear array segment (Fig. 5.6 (d)). Similar observation can be readily made regarding the US image obtained with the concave detector array having uniform pitch (Fig. 5.6 (f)). The large inter-element pitch size exceeding λ at the central frequency makes it impossible to confine the ultrasound beam into a single lobe. The energy is thus radiated at various angles resulting in ghost responses whenever strong scatterers appear within the grating lobes, which severely limits contrast of the images in those areas [98, 132]. Thus, the proposed hybrid multi-segment design of the array provides flexibility of choosing acquisition geometry that yields optimal imaging performance in both modalities.

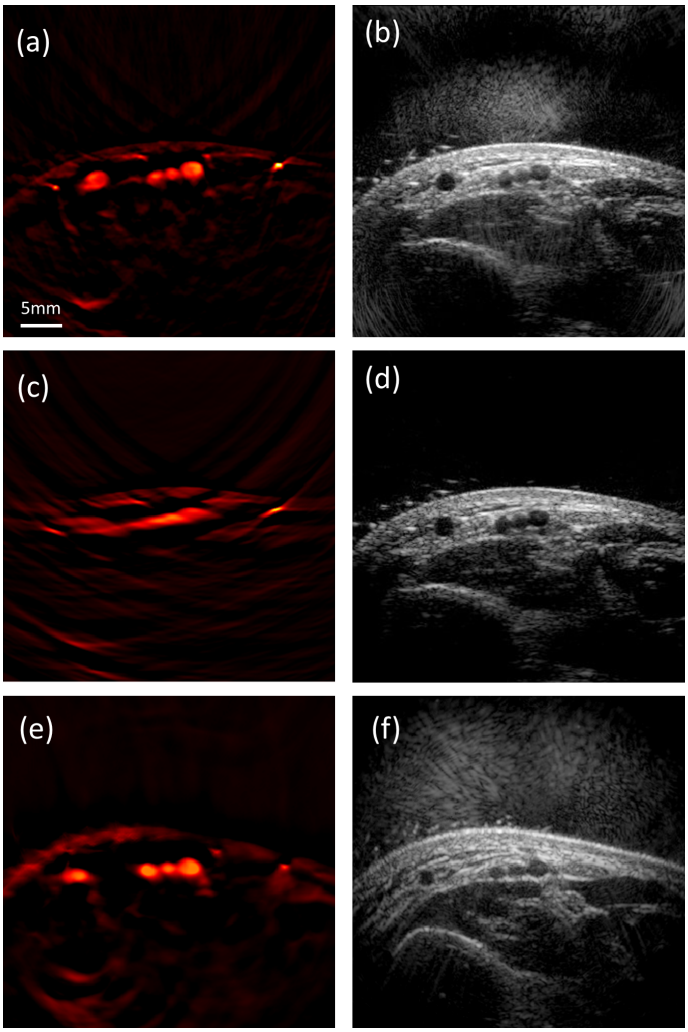

Figure 5.6: OA and US images of the wrist of a healthy volunteer. (a) OA image acquired with all 256 elements of the hybrid array transducer; (b) US image acquired with all 256 elements of the hybrid array transducer; (c) OA image acquired with 128 elements of the central linear segment of the array; (d) US image acquired with 128 elements of the linear segment; (e) OA image acquired with 256-element concave array; (f) US image acquired with 256-element concave array.

The capacity of the hybrid system for functional imaging of blood oxygenation using multi-wavelength data acquisition is further demonstrated in Fig. 5.7. Two-dimensional maps of oxy- (HbO2) and deoxy-hemoglobin (Hb) were extracted (Fig. 5.7 (a), (b)), as described in section 5.2.7, and superimposed onto the background US image in different colormaps using image transparencies (Fig. 5.7 (c)). Note that this type of visualization does not permit quantitative evaluation of the blood oxygenation levels. Yet, the unmixed images correctly assign high HbO2 signals to the radial artery (ra), whereas the Hb signal is more prominent in the radial veins (rv) and in the subcutaneous microvasculature. Vi-

sualization 1 further demonstrates the dynamic imaging performance of the hybrid OPUS system, featuring real-time hybrid image rendering and preview during hand-held scanning.

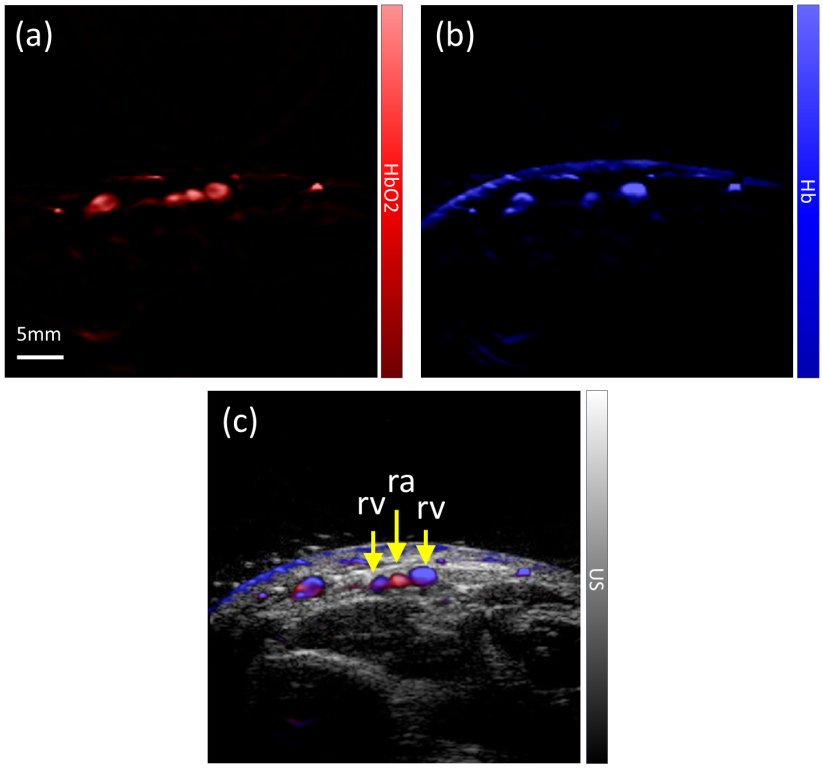

Figure 5.7: *In vivo* functional imaging performance of the OPUS system. (a) Maps of oxygenated hemoglobin (HbO2) distribution acquired in the MSOT mode; (b) The corresponding deoxygenated hemoglobin (Hb) distribution image; (c) Hybrid image compounded from the Hb, HbO2 and US images.

5.4 Applications

Changes in hemodynamic parameters are directly linked to biological function and physiological activity. Characterization of hemodynamics is commonly performed by Doppler ultrasound, which provides accurate measurements of blood flow velocity. Multispectral optoacoustic tomography is rapidly undergoing clinical translation fostered by its unique and complementary capacity for label-free mapping of the blood volume and the distribution of oxy- and deoxy-hemoglobin in blood. Here we report on a hybrid optoacoustic and ultrasound imaging approach that enables multimodal imaging of blood flow and oxygen state using a multi-segment detector array. We further demonstrate rendering of multimodal pulse-echo ultrasound, multispectral optoacoustic tomography, and color Doppler images from carotid artery of a healthy subject.

5.4.1 Imaging of blood flow and oxygen state

First, a series of images from the region of the left lower neck were collected in the first operation mode of interleaved MSOT and pulse-echo STA US, as shown in Fig. 5.8. The OA image acquired at a wavelength of 800 nm (Fig. 5.8 (a)), which effectively reflects the total hemoglobin contrast, readily allows for the identification of major blood vessels, such as the common carotid artery and the internal jugular vein owing to their increased blood absorption contrast and characteristic shapes. Note that the same vessels appear hypoechoic in the pulse-echo US image (Fig. 5.8 (b)). The jugular vein usually appears in a collapsed condition while moderate pressures applied during imaging may have caused additional flattening of the vein. From the US image it is further possible to outline the strap and sternocleidomastoid muscles, which exhibit moderate vascularization in the optoacoustic image and have lower echogenicity as compared to the thyroid tissue. On the other hand, the left thyroid lobe is characterized by a homogenous echogenicity without pronounced vascularization.

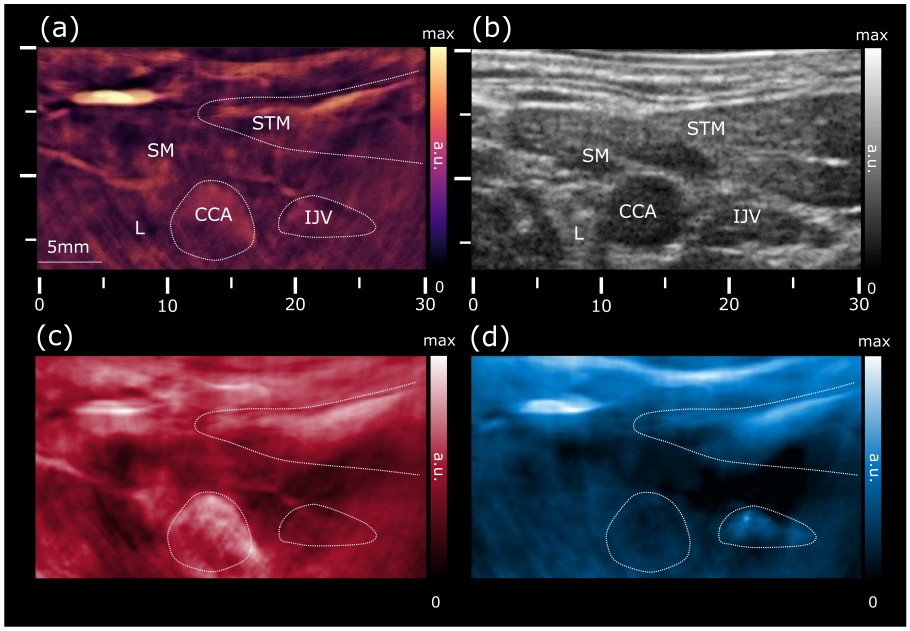

Figure 5.8: Cross-sectional views of the left common carotid artery in the transverse plane. (a) Optoacoustic image at 800 nm shows increased vascularization of the skin, strap and sternocleidomastoid muscles, allowing for a clear identification of the common carotid artery and internal jugular vein. (b) Ultrasound pulse-echo STA image revealing the common carotid artery and jugular vein as echo-free structures. (c) Map of the unmixed distribution of oxygenated hemoglobin (HbO2). (d) The corresponding map of deoxygenated hemoglobin (Hb). CCA: common carotid artery; STM: sternocleidomastoid muscle; SM: strap muscle; IJV: internal jugular vein; L: thyroid lobe.

The functional imaging capacity was further demonstrated via assessment of the blood oxygen state using multi-wavelength data acquisition. Maps of the spectrally-unmixed

distributions of oxy- (HbO2) and deoxy-hemoglobin (Hb) are shown in Figs. 2c and 2d, respectively. The images correctly assign the higher levels of HbO2 signal to the common carotid artery, whereas the Hb signal appears more prominent in the subcutaneous microvasculature and the jugular vein.

The carotid vessels were further examined from the lower neck to the point of bifurcation using the second operation mode, focusing on evaluation of the blood flow. Four representative cross-sections from the color-Doppler scan are shown in Fig. 5.9. First, the common carotid artery (CCA) was visualized in transverse section at the base of the neck (Fig. 5.9 (a)). To measure Doppler frequency shifts, the sampling window was centered at the CCA, as indicated by a blue rectangle in the image. As expected, the CCA shows a positive Doppler frequency shift (red). The probe was then rotated to acquire image of the CCA in its longitudinal section (Fig. 5.9 (b)). The measured flow velocity of the common carotid artery was in the normal range between 30 and 40 cm/s [97] and no evidence of blood flow abnormalities were observed. The CCA was also scanned along its length in transverse section, reaching the bifurcation into the external (ECA) and internal (ICA) carotid arteries (Fig. 5.9 (c)). Fig. 5.9 (d) depicts longitudinal view of the carotid bifurcation showing ECA at the top and ICA at the bottom. The sampling window was placed in a superior region of the ECA and the ICA, where the flow is directed towards the transducer in both branches. Note that a proper alignment of the ultrasound beam parallel to the vector of blood flow is further limited by the need to maintain a reasonable light incidence angle onto the tissue surface for optimal MSOT image quality [131].

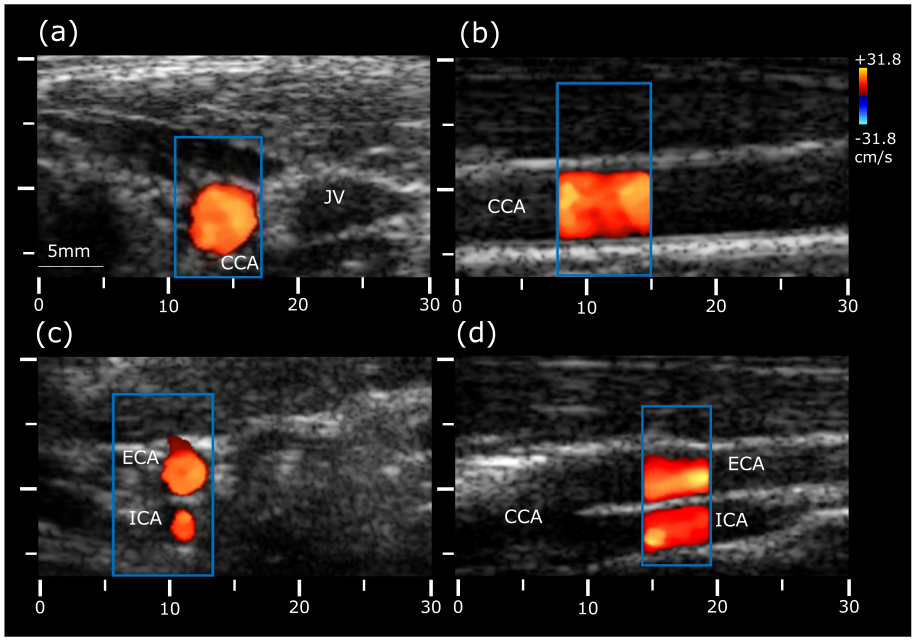

Figure 5.9: Color Doppler measurements of blood velocity in the carotid arteries and jugular vein. (a) Transverse and (b) longitudinal views of the common carotid artery; (c) Transverse and (d) longitudinal views of the carotid bifurcation into the external and internal carotid arteries. CCA: common carotid artery; ECA: external carotid artery; ICA: external carotid artery; IJV: internal jugular vein.

5.5 Discussion

The new hybrid imaging approach has been shown to provide excellent performance in both OA and US imaging modes by efficient interleaving of the data acquisition and image reconstruction schemes for both modalities. While the central (linear) part of the proposed acquisition geometry has rendered US images equivalent to those obtained with the conventional linear arrays, the two additional concave segments provided sufficient angular coverage for achieving good OA tomographic image quality. Hence, the multi-segment OPUS approach suggested herein outperformed previously reported hybrid imaging approaches based on uniform transducer arrays with either linear or concave detection geometries.

The dual-pitch design has greatly facilitated the reduction of costs and complexity of the detector array as well as the computational and memory burden. This is mainly because a uniformly small pitch on both linear and concave segments would result in more than a double the amount of elements. On the other hand, large detection elements on the concave segments ensure high sensitivity in detecting weak optoacoustic response [5], which is crucial for achieving an adequate image quality in real time without applying signal averaging. In comparison with the previously reported OPUS approaches based on concave array geometries, the newly introduced multi-segment array possesses a much larger field-of-view in both the US and OA modes. It has been previously reported that multiple linear or planar array segments were employed for enhancing optoacoustic image quality [48,76]. However, this type of design would be hardly beneficial for our purposes since many segments are required to effectively provide the 180° tomographic coverage, in which case an accurate calibration of the relative location and orientation between the multiple segments becomes challenging.

It has been shown that the sensitivity field and spatial resolution of the multi-segment array remains relatively uniform across a large area for both imaging modes. In the proposed acquisition geometry, both the spatial resolution and effective field of view can be readily optimized to fit specific applications. For example, a smaller central segment with convex geometry may provide even larger field of view for a more convenient US navigation, whereas the resolution can be enhanced by adjusting the pitch and central frequency of the elements. Smaller elements in the concave segments can be used to enlarge the OA field of view, which, however, would result in a much larger number of elements and hence in a higher complexity and cost of the system. Overall, the US and OA image features can be tuned by properly selecting the curvature and size of the different array segments as well as the size and frequency response of the corresponding detection elements. The interleaved OA and US image acquisition protocols can also be optimized to provide a faster imaging rate, which is ultimately limited by the pulse repetition frequency of the laser and maximum permissible exposure limits to laser radiation [1].

It should be noted, however, that the strongly anisotropic and non-uniform spatial resolution inherent in cross-sectional (2D) imaging approaches may still result in the so called "out-of-plane" artifacts manifested as image blurring and overall deterioration of image quality and contrast [29]. Thus, for attaining more accurate OA reconstructions, a full 3D acquisition geometry is necessary [33]. In this context, the newly introduced approach can be potentially extended to 3D image acquisition geometries by employing multi-segment matrix arrays featuring non-uniform pitch distribution. In this case, attaining a reasonably

small inter-element pitch size for adequate US imaging performance in 3D may imply a very high element count that would in turn necessitate significant upgrade of the data acquisition and processing capacities. An alternative recently reported approach suggested scanning of an unfocused linear array probe over a planar surface [72], which, however, significantly deteriorates the temporal resolution in 3D.

Imaging sessions in a healthy volunteer have proven excellent capacity of the new OPUS approach for hybrid anatomical imaging and functional angiography in humans. While major vessels can be accurately reproduced in both US and OA images, the latter have revealed smaller vasculature as well as the presence of subcutaneous microvasculature. More importantly, the functional imaging capacity of MSOT has further enabled estimating the relative concentrations of Hb and HbO2, thus providing complementary functional information. Accurate quantification of oxygen saturation has not been addressed within the scope of the current work, which solely concentrated on introducing the multi-segment detector approach. Yet, this topic remains a challenging problem and therefore an active area of research in optoacoustic tomography [195]. It is therefore anticipated that the quantified imaging performance of the hybrid OPUS approach can be greatly enhanced by introducing novel spectral acquisition and umixing approaches, which will be addressed in our future work.

It has been shown that the US image acquired by using all the 256 array elements exhibits a higher level of artifacts associated with grating lobes. This is due to a larger pitch size of the concave segments, which greatly exceeds half the acoustic wavelength. According to the spatial sampling theorem, an inter-element pitch lower than half the wavelength is required to completely avoid grating lobes [98]. For a larger pitch size, the energy is not confined to a single lobe, but radiates off at various angles. Hence, ghost responses are produced for strong scatterers located along the directions corresponding to the grating lobes, which result in image artefacts [132] that can be avoided when the image is rendered solely by the linear array segment.

The large FOV in the US mode achieved with the proposed multi-segment detector array can greatly aid the anatomical navigation and localization of structures to be imaged in the OA mode, which translates into better applicability in a clinical setting.

In combination with stage controlled animal beds [141], additional areas of potential application also include pre-clinical research, e.g. in the fields of neuroimaging [50, 65], and cardiovascular research [182].

The showcased capability of mapping the blood flow and oxygen state by means of the multi-segment detector array may provide a complementary diagnostic value to the existing functional imaging capacities of the stand-alone optoacoustic and ultrasound technologies. In combination with the rendered Doppler-based blood velocity measurements, the MSOT-based metrics may contribute to a more reliable assessment of the severity of carotid artery disease. Hemodynamic measurements are commonly done in patients undergoing surgery or in critical condition. In such cases, monitoring of multiple hemodynamic parameters may help in guiding treatments in a time frame that permits intervention to prevent organ failure [78].

In conclusion, by efficiently combining the benefits of ultrasonography and multispectral optoacoustic tomography, the developed hybrid OPUS approach brings a new standard of anatomical and functional imaging performance in biomedical research and clinical practice.

6 Transmission-Reflection Optoacoustic Ultrasound (TROPUS) Computed Tomography of Small Animals

6.1 Introduction

Over the last years tremendous advancements have been introduced into multispectral optoacoustic tomography (MSOT) technology [41, 187]. Those have enabled the implementation of ultrafast imaging systems for volumetric visualization of organ dynamics and motion [27, 53], whole body imaging of small animals with unsurpassed image quality [130], sensitive deep-tissue detection of molecular agents and disease bio-markers [101, 163]. MSOT brings along important advantages in terms of label-free anatomical and functional contrast arising from intrinsic tissue components, such as oxy- and deoxy-haemoglobin, melanin, bilirubin, lipids and water. In particular, the strong optical absorption of hemoglobin allows the visualization of vascular structures and hemodynamic responses, maintaining sub-millimeter resolutions at depths of several centimeters within highly scattering living tissues in the near-infrared spectrum. The great pre-clinical potential of MSOT has also encouraged the translation of this technology into the clinics with dedicated handheld [177] and endoscopic [71] probes introduced for high performance imaging of human subjects. Ultrasound (US) tissue contrast provides highly complementary information on elastic and functional properties [66]. At present, pulse-echo (reflection-mode) ultrasonography remains the most commonly employed clinical imaging modality. It is equally exploited in pre-clinical research, representing an essential tool in many active research areas such as neuroimaging [36], cardiology [93], tumor angiogenesis [113] or the development of novel contrast enhancement approaches [21]. Transmission-mode ultrasound computed tomography (TUCT) can instead map the distribution of speed of sound and acoustic attenuation, which are representative of a different set of physiological tissue properties, such as stiffness, density and temperature [64, 168]. In this regard, TUCT has been used to map the distribution of speed of sound (SoS) and acoustic attenuation (AA) in the female breast [104, 110], where recent clinical trials suggest a superior performance with respect to standard screening approaches in terms of safety, examination time and patient comfort [46, 106]. The integration of US-based imaging approaches into multi-modal optoacoustic-ultrasound (OPUS) platforms has previously been shown to complement and enhance advantages of the stand-alone modalities. The hybridization between optoacoustic (OA) and reflection-mode (pulse-echo) US imaging has recently been achieved with linear [152], concave [132] or multi-segment arrays [131]. Multi-modal endoscopic [207] and microscopic [51] imaging systems based on single-element transducers have also been suggested. Other efforts have been directed towards enhancing image quality by incorporating complementary information in recon-

struction algorithms [87], clearly evincing added value of the multi-modal approach. Efficient hybridization between the various OA and US imaging modalities is often hampered by the fundamental differences in the underlying contrast mechanisms and image formation strategies. While reflection-mode US is commonly performed with linear or convex arrays from a single access point to the sample, optimal transmission-mode US and OA reconstructions are achieved with large tomographic coverage from multiple views around the imaged region. The detected signal intensity ranges can also differ substantially for transmitted versus back-scattered US waves or OA responses [143], which implies different implementations of the front-end signal generation and amplification electronics and digitization chains. Here we devised a hybrid transmission-reflection optoacoustic ultrasound (TROPUS) imaging platform for whole-body computed tomography of small animals (Fig. 6.1(a)). The system features full view cross-sectional tomographic imaging geometry for concomitant non-invasive mapping of the absorbed optical energy, acoustic reflectivity, speed of sound and acoustic attenuation in whole living mice with sub-millimeter resolution. For this, a dedicated multiplexer unit was further developed to control and synchronize the excitation and detection of signals by the custom-made full-ring 512-element cylindrically-focused US transducer array (see Methods for details of the experimental set-up).

6.2 Materials and methods

6.2.1 Experimental system

Key instrumentation aspects and algorithmic strategies employed in the hybrid OPUS system are described in Chapter 3. Here we remind the reader and repeat some of the description for completeness.

The experimental set-up for the hybrid transmission-reflection optoacoustic ultrasound (TROPUS) system is schematically depicted in Fig. 6.1(a). The system comprises a dedicated multiplexer unit configured to control the custom-made full-ring US transducer array in two different operation modes in a time-interleaved fashion. In the receive-only mode OA signals are collected, whereas in the transmit-and-receive mode the array is actively driven to generate US waves and acquire the reflected and transmitted signals. The custom-made ring-shaped detector array of cylindrically-focused transducers (Imasonic SaS, Voray, France) was designed to cover nearly 360° around the imaged object, which facilitates optimal data acquisition for transmission and reflection US imaging as well as sufficient angular coverage for accurate OA tomographic imaging [35, 150]. The array has 512 elements in total and consists of two concave sub-arrays, attached to each other by means of special locking mechanism, each having 256 elements, active angular aperture of 174°, and radius of curvature of 40 mm with the individual elements focused at a distance of 38 mm. The modular design provides the flexibility to operate one of the 256-channel sub-arrays in a handheld mode. The elements have central frequency of 5 MHz, nominal Tx/Rx bandwidth of 60% and inter-element pitch of 0.47 mm. For acquisition of 3D data in all the modes, the array was translated along the mouse using a vertically-oriented translation stage (Model RCA2-TWA4NA, IAI Corporation, Shimizu-Ku, Japan). OA signal excitation was done with a pulsed ($\sim$ 8 ns) Nd:YAG laser (Spectra Physics, Santa

Clara, California) with 15 Hz repetition rate and 1064 nm optical wavelength. An optical fiber bundle (LightGuideOptics GmbH, Rheinbach, Germany) composed of 620 fibers distributed over 12 output ferrules was fixed at both sides of the transducer array (Fig. 6.1(a)) at angular steps of 60°. The fibers in each output ferrule were arranged along a rectangular surface with dimensions 0.21 mm x 12.65 mm and oriented at $\sim 24^{\circ}$ angle with respect to imaging plane of the array to achieve a uniformly illuminated ring with an area of ~ 6 cm^2 on the surface of the mouse. The total per-pulse energy measured at the output of the fiber bundle was ~ 54 mJ, resulting in light fluence of 9 mJ/cm^2 on the surface, which is well below the ANSI limit of 100 mJ/cm^2 at 1064 nm [80].

For collection of reflection- and transmission mode US data, the synthetic transmit aperture (STA) technique was employed (Fig. 6.1(b)) with active sub-apertures of 128 elements. Generation of a single-cycle bipolar pulse (20 Vpp, 6 MHz) from the first channel (TX 1) of the active sub-aperture results in an unfocused transmitted beam. The reflected (or backscattered) US wave front is subsequently recorded by all the 128 channels of the active sub-aperture (RX 1-128). The active group is subsequently moved by one channel and the transmit-receive cycle is repeated for all channels, i.e. TX 2, RX 2-129; TX 3, RX 3-130; TX 512,RX 512, 1-127. Transmission by the last channel (TX 512) and reception with the active group RX 512, 1-127 concludes the first acquisition cycle (AQ 1). Therefore, four acquisition cycles are required to collect reflected (transmitted) signals for each pair of transmit-receive channels. The schematic matrix representation of the acquisition in Fig. 6.1(c) with rows/columns corresponding to the transmit/receive (TX/RX) channels shows which channels were used in each of the four acquisition cycles. From this representation one may observe how US data for any pair of transmit and receive elements were collected, e.g. for the 1st transmit channel (TX 1), the echo waves were received by channels RX 1-128 in the 1st acquisition cycle (AQ 1), by channels RX 129-256 in the 2nd acquisition cycle (AQ 2), and channels RX 257-384 and RX 385-512 – in the 3rd (AQ 3) and 4th (AQ 4) acquisition cycles, respectively. Acquisition of reflection- and transmission US data was performed by a custom-built US data acquisition system (DAQ) having 128 transmit/receive channels (S-Sharp Corporation, Taiwan), 12-bit vertical resolution, 10 MHz input bandwidth, 24 MS/s sampling rate, and the function of triggered acquisition. In the implemented transmission ultrasound imaging scheme, single element is excited for each transmission event with the driving voltage limited to 20 V. Unfocused transmit beams are generated in this way, thus imposing significantly lower levels of ultrasound exposure as compared to conventional B-mode schemes using multi-element transmission and focused transmit beams. In particular, the current FDA regulatory limit for adult diagnostic imaging is Ispta = 720 mW/cm^2 (spatial-peak-temporal-average) whereas in our case the short pulse transmission with a single element resulted in intensity levels well below 50 mW/cm^2.

OA data acquisition was based on simultaneous collection of the generated signals by all the 512 channels of the array (Fig. 6.1(c)). Digitization was performed with a custom-made OA DAQ at 40 MS/s and 12-bit vertical resolution. The time required for OA tomographic data acquisition was ~ 50 μs, whereas ~ 86 ms were required for one full US image acquisition. The multiplexing unit synchronizing OA and US acquisitions was based on the pre-defined timing scheme triggered with the laser pulses (Fig. 6.1(d)).

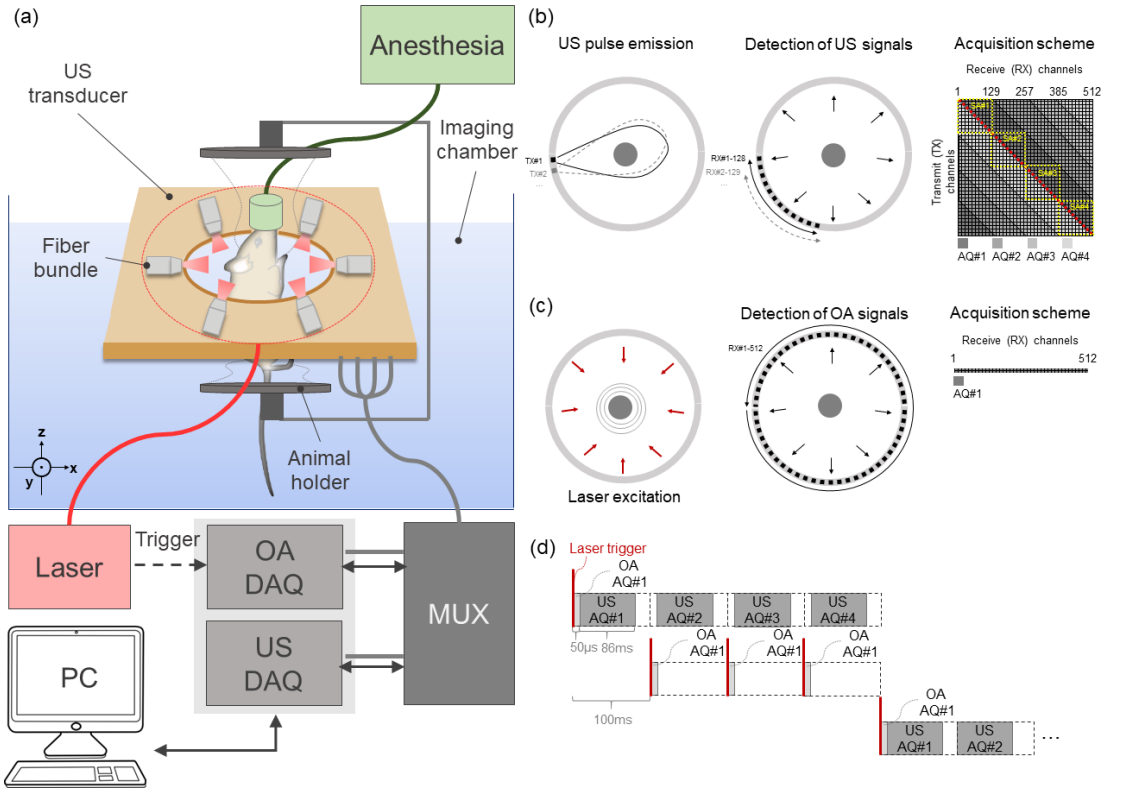

Figure 6.1: Diagram of the transmission-reflection optoacoustic ultrasound (TROPUS) imaging platform for whole-body computed tomography of small animals. (a) Block diagram illustrating the key components of the experimental prototype. A dedicated digital acquisition and signal generation hardware was developed for synchronizing the excitation and detection of broadband ultrasound signals by a 512-element cylindrically-focused full-ring array; (b) Both reflection- and transmission-mode ultrasound are based on sequential active excitation of each array element and parallel detection of 128 signals, i.e., four acquisition cycles are required for collecting signals from all the 512 channels; (c) In the optoacoustic data acquisition mode, signals generated by each laser pulse are recorded by all the 512 channels simultaneously; (d) The multiplexing unit synchronizing optoacoustic and ultrasound imaging modes was based on the pre-defined timing scheme triggered with the laser pulses.

6.2.2 Image reconstruction and post-processing

For OA image reconstruction, the acquired signals were first pre-processed with a 3rd order Butterworth band-pass filter (0.5 and 7 MHz cut-off frequencies) and deconvolved with the electrical impulse response of the transducer, simulated based on Krimholtz-Leedom-Matthaei (KLM) circuit model [103] using the information provided by the manufacturer. Reconstruction was then performed with a statistical weighting approach [30] assuming different speed of sound in the sample and the surrounding water [32]. A value of 1520 m/s was assumed for water at 34°C [124]. The mouse boundary was segmented from an OA image reconstructed assuming uniform speed of sound. The speed of sound value inside the mouse was assigned by considering the mean value of 95% top pixels of the reconstructed TUCT-SoS images. Specifically, values of 1573 m/s, 1565 m/s, and 1552 m/s were assumed for reconstructing cross-sections in the liver, kidney, and intestine regions of the mouse, respectively. A weighting-based back-projection algorithm was employed to mitigate image artifacts primarily stemming from the acoustic reflections from bones or air in areas such as spinal cord and intestine [204]. To improve signal-to-noise ratio (SNR) of the recorded OA signals, 50 frames were acquired for each position, out of which $\sim$ 30% (15 frames) covering the breathing cycle were discarded and the rest of the frames were averaged. For this we employed a simple retrospective motion correction algorithm based on removal of frames with in-plane motion (2D) [53]. In particular, a similarity metric function is calculated for each of the selected cross-sectional (2D) slices, reflecting the level of similarity between a particular slice and the reference slice. The latter represents an artificial frame from the median of all PCA coefficients. Once all similarity metrics are calculated, a desired percentage of most deviating frames can be discarded. To enhance contrast of the reconstructed OA images, several post-processing steps were further applied. First, we used contrast-limited adaptive histogram equalization (CLAHE) [210] with the Rayleigh distribution specified as a desired histogram shape. At the second step, vascular contrast was enhanced with the help of a multiscale vesselness filter [58] applied at scales σ = 0.5, 1, 2, 3 ,4. Two-dimensional vesselness filter was used instead of its 3D counterpart due to the relatively large step size between the adjacent slices. In addition, cylindrical focusing of the transducer array has resulted in an inferior spatial resolution in the elevation direction, thus making this particular tomographic configuration suboptimal for rendering true 3D reconstructions in order to accurately represent vascular structures in arbitrary directions [27]. Note that the adaptive histogram equalization is applied to the image at each scale followed by the weighted summation of the resulting images. At the final step, background suppression was applied to reduce nonzero background intensity. For this, the image was manually segmented into the foreground (mouse body) and background (surrounding coupling medium). The manual segmentation was performed under supervision of an experienced biologist and bio-imaging expert by drawing polygons around the structures followed by spline interpolation of the polygon smoothening. The background intensity was then reduced by a factor of 1.25 compared to the intensity of the foreground.

In the RUCT mode, a high-resolution image was created by coherent summation of the low-resolution images from 128 individual transmission events corresponding to one sub-aperture (SA). In particular, for each transmission event from a single element, echoes were collected by all the elements of the sub-aperture and a low-resolution image was gener-

ated by means of a standard delay-and-sum algorithm [73]. The transmission is repeated for all the 128 sub-aperture channels. In the current study, a total of four 128-element sub-apertures were used to cover the complete 512-element aperture of the full-ring array. A final tomographic image was then generated with a spatial compounding technique [85]. This involves incoherent summation of the high-resolution images corresponding to different sub-apertures from multiple viewing angles. Transmit and receive channels that constitute four sub-apertures (SA 1-4) used to compound a final image are shown in Fig. 6.1(b). Beamforming was performed on the signal envelope extracted using the following preprocessing steps: baseband demodulation of the signals, low-pass filtering with cut-off frequency of 10 MHz to suppress noise, and up-mixing to shift the frequency spectrum from the base-band back to its original band [99]. GPU-accelerated reconstruction of the RUCT images was performed on the US DAQ system and subsequently transferred as binary raw data files via Ethernet to the PC. The post-processing steps for the final RUCT images included logarithmic compression, image upscaling by factor of 2 and conversion to RGB using a custom-built colormap "golden hue" [138].

In TUCT mode, the transmission data was used to reconstruct speed-of-sound (SoS) and acoustic attenuation (AA) maps. For this, the time-of-flight (TOF) and signal attenuation were determined for each emitter-receiver pair. The TOF was obtained following the method proposed in [111]. The TOF picker code from E. Kalkan [91] was adapted to improve the accuracy of the selected TOF picks by weighting in the TOF values around the selected TOF, as described elsewhere [109]. No additional signal denoising was needed before the TOF picker [9] due to the high SNR of the signals. Median filtering and reciprocal pair comparison were incorporated in the TOF picker to effectively remove the outliers [109]. Signal attenuation was determined using the complex signal energy ratio method described in [109]. The acoustic attenuation coefficients are related with the measured signals as follows

$$\sum_{j=1}^{n} A_{i,j}\alpha_{0,j} = \frac{1}{f_c} ln\left(\frac{I_i^{'}}{I_i}\right), \tag{6.1}$$

where $A_{i,j}$ represent the propagating path along the ray determined by the emitter-receiver pair i within pixel j , $alpha_{0,j}$ is the attenuation coefficient at the pixel j; $I_i^{'}$ is the amplitude of the signal for the emitter-receiver pair i when there is only water in the field of view (FOV), I_i is the corresponding amplitude with the object located in the FOV and f_c is the central frequency of the signal.

The TOF and signal attenuation values extracted from the transmitted data served as the input for a bent-ray tracing iterative reconstruction algorithm [115]. In this work, the shortest (geodesic) path between each pair of ultrasound transducers for a given SS map was modeled as a Bézier curve [156, 190]. The geodesic path was selected among a family of quadratic Bé zier curves connecting the emitter and the receiver as the curve providing the lowest TOF. Among the many methods suggested to obtain the geodesic path [115,159], our approach has the advantage of exploiting the large capabilities of graphics processor units (GPU) to perform many computations in parallel. Each thread of the GPU was able to evaluate in parallel the TOF along a particular Bézier curve, which makes the code very fast and easy to use. Once that the geodesic paths have been determined, the Maximum Likelihood - Expectation Maximization (ML-EM) [159] was used to solve the optimization

Table 6.1: Tissue-mimicking phantom composition

Component	Concentration	Unit
Water	100	ml
Agar	1.3	g
Ink	0.2 (1.500 dilution)	ml
Intralipid	6	ml
Glass microspheres	2.5	g

problem for the SoS and the AA maps as

$$\xi_j^{n+1} = \frac{\xi_j^n}{\sum_{i'=1}^{M} A_{i',j}} \sum_{i=1}^{M} A_{i,j} \frac{p_i}{\sum_{j'=1}^{N} A_{i,j'} \xi_{j'}^n}, \tag{6.2}$$

where ξ_j^{n+1} is either the speed of sound or the attenuation coefficient value in the pixel j for iteration $n+1$ based on the value ξ_j^n for iteration n. $A_{i,j}$ are the coefficients defined in Eq. 6.1, and p_i representa the measured pressure field at the receiver location i. A total of 50 iterations (image updates) were used for reconstructing each 2D slice. They may ask about regularization in the inversion or things like that. For visualization, the mean intensity values of the background of the TUCT-SS and TUCT-AA images were calculated and set as minimum threshold such that the intensity values lower 1520 m/s and 0.002 dB·cm^{-1}·MHz^{-1} for the TUCT-SS and TUCT-AA images, respectively, were not displayed in the final RGB images.

All post-processing steps were performed in MATLAB (2016b, MathWorks, Natick, MA) on a desktop computer with Intel Core i7-4820K 3.7-GHz processor and 32-GB RAM.

6.2.3 Characterization of the imaging performance

A tissue-mimicking phantom with defined speed of sound and acoustic attenuation was used to test the imaging performance of the hybrid system. The phantom had a cylindrical shape with diameter of 20.0±0.2 mm and length of 50±0.2 mm. Acoustic attenuation was mimicked with glass microspheres (SpheriglassA, Potter Industries LLC, Malvern, Pennsylvania) with diameters between 38 and 63 μm added to the agar-based solution. Table 6.1 summarizes the concentrations of each additive for the tissue-mimicking phantom.

The acoustic properties of the phantom material were characterized with an acoustic transmission test. For this, a fiber bundle was coupled to the Nd:YAG laser and a thin wire served as an optoacoustic source. The phantom was immersed in a water-filled container. A single-element transducer (Sonotec, Halle, Germany) with 10 mm element size, 5 MHz center frequency and 80% bandwidth was used to collect the transmitted signals and a photodiode positioned near the output of the excitation laser source to trigger the oscilloscope acquisitions.

The OA signals generated by the wire were acquired for the container containing water

as reference and with the phantom material immersed. The speed of sound within the sample was determined from the temporal shift between the position of the OA signal peak with and without the sample in the path, as:

$$c_s = \left(\frac{1}{c_w} - \frac{\Delta t}{d} \right)^{-1}, \tag{6.3}$$

where c_w is the speed of sound in water [m/s], d is the sample thickness [m], and Δt is the time shift of the signal peak with the sample in place relative to the reference signal in water [s]. The speed of sound in water was calculated according to the formula for the speed of sound in distilled water as a function of temperature [124]. The effect of temperature on the speed of sound of the material was estimated with measurements conducted at 21°C, 23°C and 25°C. The target temperature was achieved with an electronic submersible water heater (Model 560, Offenbach, Schego GmbH, Germany) regulated with a thermostat. Three measurements were conducted three times in 5, 10, and 15 min to ensure the temperature stability and the data were fitted in a least-squares sense by the 2nd order polynomial.

The attenuation as a function of frequency [dB· cm^{-1}] was calculated from the log difference between the two spectra obtained:

$$\alpha(f) = -\frac{20}{d \cdot 10^2} log_{10} \frac{A_s(f)}{A_w(f)}, \tag{6.4}$$

where $A_s(f)$ - magnitude of the spectrum with the sample in place, and $A_w(f)$ - magnitude of the spectrum with no sample in place. The measurements were conducted three times, and the measured values were fitted by the frequency power law:

$$\alpha(f) = \alpha f^b \tag{6.5}$$

The phantom was further used to characterize the resolution of the implemented optoacoustic, reflection- and transmission ultrasound computed tomography imaging modes. For this, the transducer array was positioned relative to the phantom such that the center of the cylinder had coordinates (x,y)=(0,10) [mm], and the edge of the cylinder was located at the center of the transducer curvature with coordinates (x,y)=(0,0) [mm]. The resolution of the system as a function of distance from the array center was estimated by analyzing different radial intensity profiles. Specifically, the resolution was calculated as the edge response defined as the distance in the image between the points having intensities of 10% and 90% from the maximum image value [173].

6.2.4 Animal imaging

A healthy ICR (Imprinting Control Region) albino mouse was used for *in vivo* imaging. The animal was anesthetized with a mixture of 1.8% isoflurane in 100% oxygen at a 0.8 L/min flow rate, positioned into the imaging chamber in the upright position using a custom-designed animal holder, and, maintained under anesthesia throughout the experiment. The water temperature was strictly maintained at 34°C with an electric heater (Model 560, Offenbach, Schego GmbH, Germany). A series of cross-sectional images were sub-

sequently acquired from the anterior to posterior regions with 2 mm step size. All procedures involving animal care and experimentation were conducted in full compliance with the institutional guidelines of the Institute for Biological and Medical Imaging and with approval from the government of Upper Bavaria.

6.3 Results

6.3.1 Multi-modality imaging performance characterization

Performance of the developed system was tested by imaging a tissue-mimicking phantom, whose acoustic properties, namely attenuation and speed of sound, were first estimated using an acoustic transmission set-up with the phantom placed in between a light-absorbing 0.3 mm thick carbon black suture generating ultrasound signals and a single-element transducer. The experimentally measured acoustic attenuation and speed of sound of the phantom at 21.3°C were 0.26 dB/MHz/cm and 1492.1 m/s, respectively. Fig. 6.2 displays the resulting multi-modal images of the phantom. To accurately characterize the spatial resolution across the imaging plane for all the supported imaging modes, the phantom was positioned with its edge crossing the center of the circular array geometry and the radial signal profiles were assessed along the trajectories indicated in Fig. 6.2(a). The estimated in-plane spatial resolution as a function of the radial distance from array center are displayed in Fig. 6.2(e). The resolution values for both OA and reflection ultrasound computed tomography (RUCT) modes are comparable to those previously reported for a similar concave array with 270° angular coverage [130]. The spatial resolution in TUCT for both AA and SoS modes is lower than for the other modes but still within the sub-millimeter range. This is in agreement with what was previously achieved for ray-theory-based TUCT reconstructions, where resolution in the order of 2-3 mm has been reported [115].

6.3.2 Accuracy of the acoustic attenuation and speed of sound estimation

Acoustic properties such as attenuation and speed of sound of the material of the tissue-mimicking phantom were estimated using the acoustic transmission measurement setup, as described in Sec. 6.2.3. Knowledge of the expected acoustic properties allows evaluating the performance of the TUCT method with respect to the accuracy of the reconstructed acoustic attenuation and speed of sound maps. The measured and fitted acoustic attenuation as a function of frequency is shown in Fig. 6.3 (c), where the coefficients a and b of the power law (Eq. 6.5) are estimated to be a = 0.82 and b = 0.35, respectively. Considering the transmit frequency of 6 MHz used in the experiment this results in the expected acoustic attenuation of the phantom material α = 0.26 dB·cm^{-1}·MHz^{-1}. Fig. 6.3 (d) shows the measured and fitted speed of sound as a function of ambient water temperature, where the coefficients a and b of the 2nd order polynomial fit are estimated to be p1 = 0.2, p2 = -4.9, and p3 = 1523.5. Considering the measured ambient water temperature during the phantom experiment constituted 21.3 °C, this results in the expected speed of sound of the phantom material c = 1492.1 m/s.

After the acoustic properties of the phantom material were characterized, the reconstructed images of the fabricated phantom were used to evaluate the performance of the

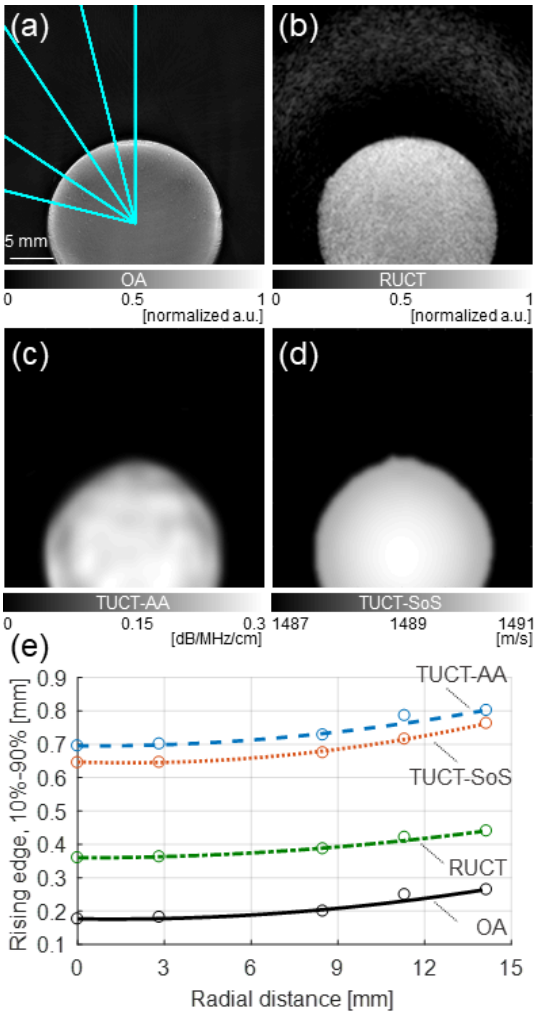

Figure 6.2: Imaging performance characterization of the TROPUS system in tissue-mimicking phantom. (a) Optoacoustic tomographic reconstruction of the phantom. Trajectories of the radial intensity profiles used for the spatial resolution characterization are marked in blue; (b) The corresponding reflection ultrasound computed tomography (RUCT) image of the phantom; (c) Acoustic attenuation image of the phantom reconstructed using transmission ultrasound (TUCT-AA); (d) The corresponding speed of sound (TUCT-SoS) image. (e) Measured and fitted in-plane resolution as a function of distance from the array centre for all the four cases.

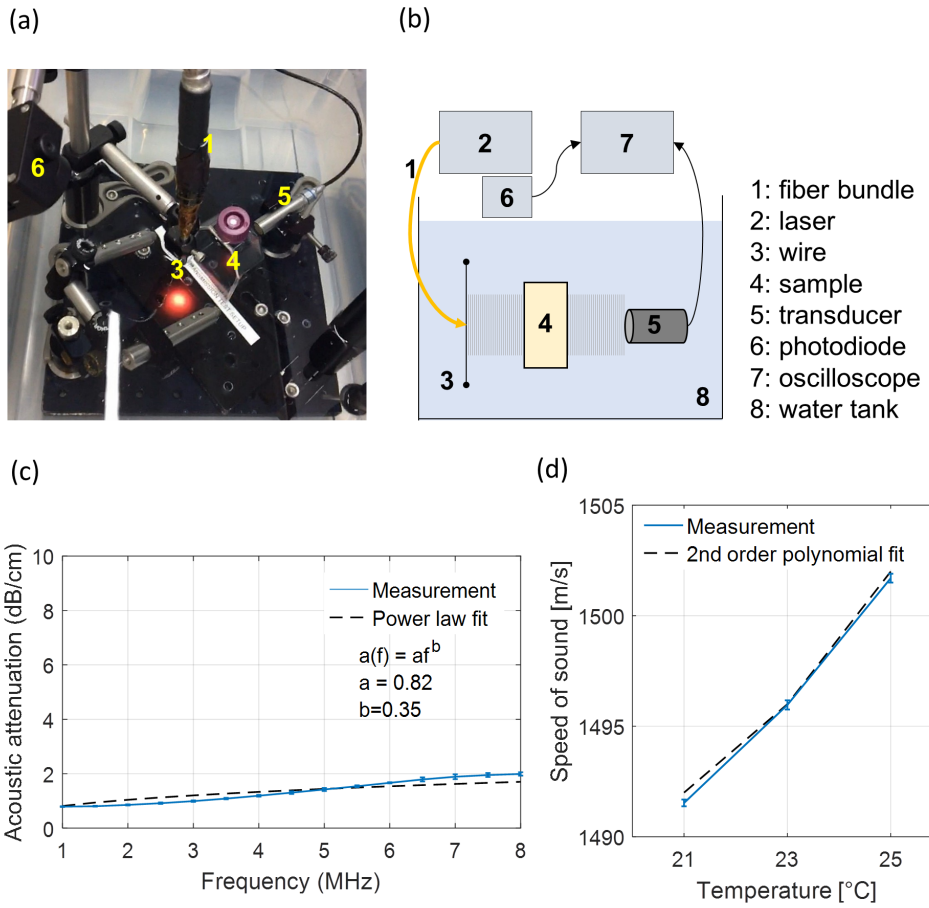

Figure 6.3: Characterization of accuracy of the acoustic attenuation and speed of sound estimation. (a), (b) Photo and schematics of the acoustic transmission measurement setup; (c) Frequency-dependent acoustic attenuation of the phantom in a range from 1 MHz to 8 MHz; (d) Temperature-dependent speed of sound of the phantom.

Table 6.2: Expected and measured values for the speed of sound (SoS) and the acoustic attenuation (AA) distributions for the tissue-mimicking phantom

Property	Expected	Measured
Acoustic attenuation [dB·cm^{-1}·MHz^{-1}]	0.26	0.28±0.008
Speed of sound [m/s]	1492.1	1493±0.04

TUCT method with respect to the accuracy of the reconstructed acoustic attenuation and speed of sound maps. For this, with help of the mechanical stages the transducer array was positioned relative to the phantom such that the center of the cylinder was located in the center of the transducer curvature with coordinates (x,y)=(0,0) [mm], and the mean and standard deviation of the pixel intensities in the circular region of interest (ROI) of 2 mm diameter in the center of the cylinder were evaluated for the AA and SS maps, respectively. The resulting measured values are summarized in Table 6.2. As it can be seen, the AA and SS distributions can be recovered with high accuracy. The bias between the reconstructed and expected values is 7.7% and 0.06% for the respective cases of the AA and SS distributions.

6.3.3 Whole-body mouse imaging *in vivo*

The *in vivo* applicability of the developed TROPUS system was demonstrated via noninvasive whole-body imaging of a mouse. The animal was positioned in the upright position inside the imaging chamber (Fig. 6.1(a)) and maintained under anesthesia throughout the experiment. Representative cross-sectional reconstructions from anterior to posterior regions of the mouse are presented in Fig. 6.4 for all the imaging modes. The fully co-registered images represent very diverse types of tissue contrast, thus reveal distinct and complementary anatomical and physiological information.

Since the OA contrast stems from optical absorption by tissue chromophores, most importantly oxy- and deoxy-hemoglobin [172], vessels and vascularized organs, e.g. kidney or spleen, are clearly visible in the images. At the same time, large vessels, such as the thoracic aorta and vena cava appear anechoic (dark) in the RUCT images. Bones and skin provide clear hyperechoic (bright) contrast while some organs, including stomach and pancreas, produce more diffuse reflections leading to hypoechoic (grey-colored) contrast. Also, considering that the US contrast stems from the acoustic impedance mismatch between different tissues, the RUCT images allow for an easy identification and boundary delineation of distinct organs.

The TUCT images, representing distribution of the SoS and AA across the mouse, provide complementary information to the tissue optical absorption and acoustic reflectivity delivered by the OA and RUCT modalities. The SoS depends on medium density and stiffness, both can be altered under certain disease conditions [70]. As expected, SoS fluctuations amount to about 5% in the healthy soft tissues (Fig. 6.4(c)). Missing transmitted acoustic signals create more significant SoS heterogeneities in bones as well as areas with air accumulation like lungs, stomach or intestines. Absence of an alternative (reference) method for *in vivo* SoS characterization hinders univocal validation of the reconstructed

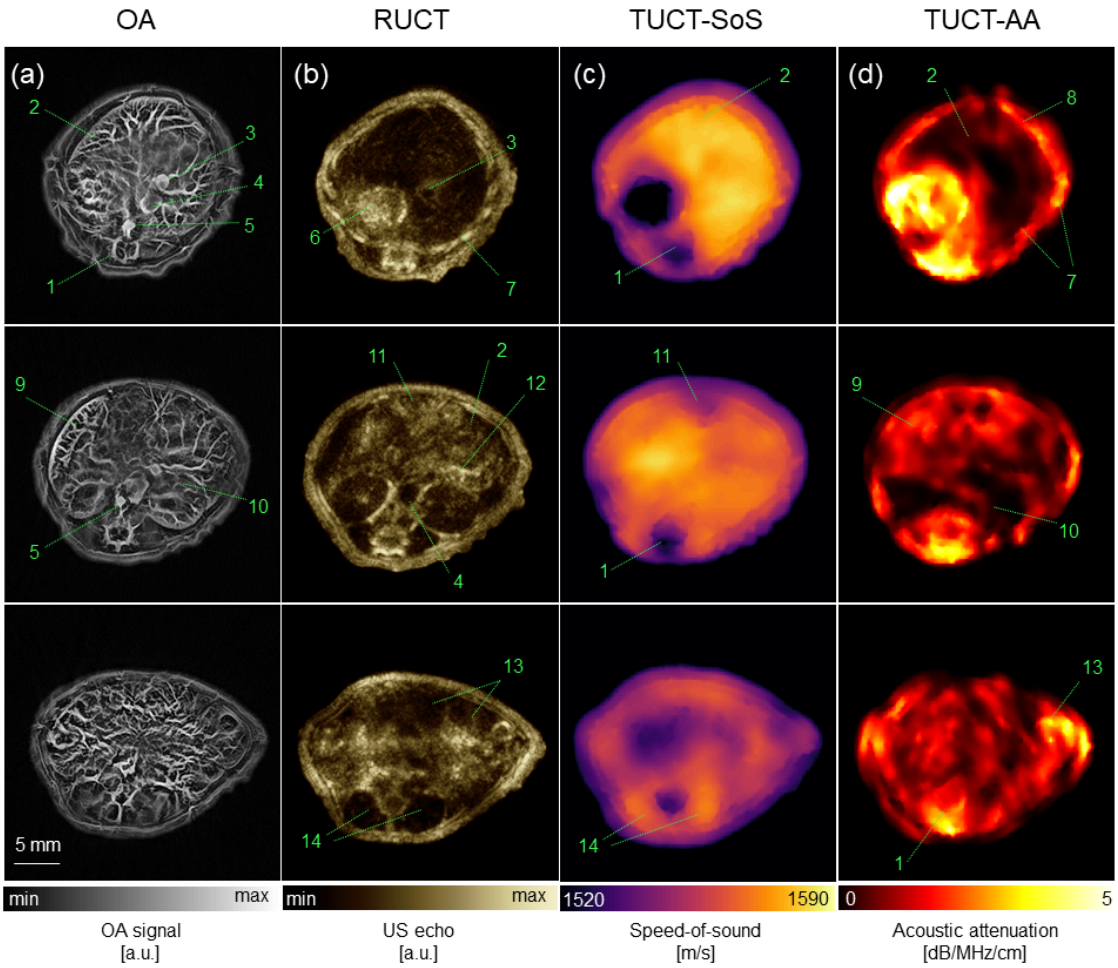

Figure 6.4: Hybrid transmission-reflection optoacoustic ultrasound (TROPUS) whole-body imaging. (a) Representative cross-sections acquired in the optoacoustic mode; (b) The corresponding reflection-mode ultrasound images; (c), (d) The corresponding transmission-mode ultrasound images showing the distribution of the speed of sound and acoustic attenuation, respectively. Annotations: 1: spinal cord; 2: liver; 3: vena porta; 4: vena cava; 5: aorta; 6: stomach; 7: ribs; 8: skin/fat layer; 9: spleen; 10: right kidney; 11: cecum; 12: pancreas; 13: intestines; 14: muscle.

SoS values. However, those are closely resembling the typical average values reported for soft tissues (1540 m/s) [203], liver (1573 m/s) or kidneys (1565 m/s) [45]. The reconstructed AA maps exhibit larger fluctuations44 of more than 60% in the average AA between the 3 cross-sections shown in Fig. 6.4(d).

6.3.4 Image quality enhancement

Raw optoacoustic images reconstructed using commonly employed filtered back-projection schemes are often afflicted by multiple artifacts, thus may exhibit low contrast and insufficient level of anatomical detail (Fig. 6.5(a)). Loss of resolution associated with acoustic heterogeneities and uneven light deposition across the mouse can be partially mitigated by means of a statistically weighted back-projection algorithm, resulting in fewer artifacts, clearer skin boundaries, and a finer detail of internal structures (Fig. 6.5(b)). It is further possible to improve image resolution and reduce artifacts manifested via distorted shape of the peripheral vessels by employing reconstruction that uses different speed of sound inside the mouse and the surrounding water (Fig. 6.5(c)). Visual quality of the OA images is commonly impaired by the presence of highly-absorbing vascular features and highly heterogenous light distribution in the object that lead to erroneous weighting of the recorded signals during the reconstruction process and appearance of hot spots in the images. A number of processing steps can be employed to improve the perceived image contrast. First, we applied contrast limited adaptive histogram equalization (CLAHE) to enhance an overall image contrast (Fig. 6.5(d)). Contrast of the vascular structures can be further improved by using vessel enhancement filters [112, 197], as showcased in Fig. 6.5(e). This particular multi-scale filtering approach, which employs Gaussian kernels of various sizes, can efficiently preserve and highlight blood vessels of different orientation and size48 while further emphasizing the mouse boundary. The final image enhancement step consisted of suppressing the background signals outside the mouse, thus further improving the perceived image quality (Fig. 6.5(f)). It should be noted that the newly developed full-view array geometry has greatly contributed to the overall visibility and resolution of anatomical structures across entire mouse cross-sections, thus mitigating artifacts commonly present in optoacoustic images acquired with limited-view tomographic systems [35]. Yet, the developed cross-sectional imaging system uses in-plane cylindrical focusing, which may result in loss of image quality due to unisotropic resolution in the vertical (z) versus lateral (x-y) dimensions.

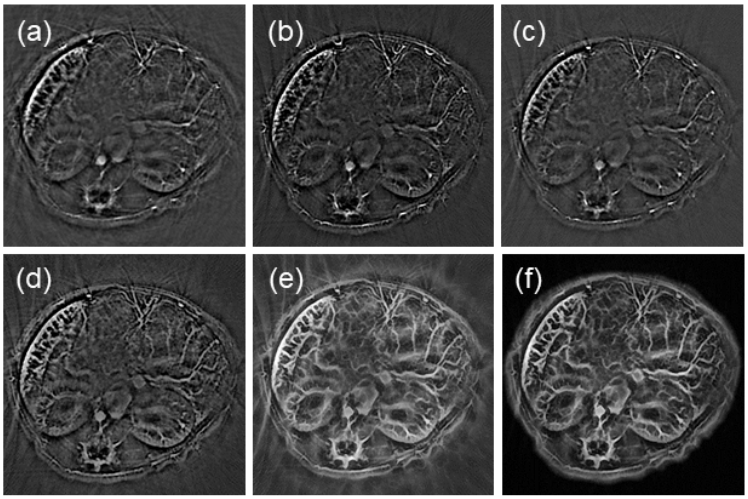

Figure 6.5: Enhancement of the optoacoustic image contrast. (a) Cross-sectional image of the mouse in the kidney area that was reconstructed using two-dimensional filtered back-projection algorithm assuming a uniform average speed of sound of 1542 m/s; (b) The same image reconstructed using a weighted back-projection algorithm; (c) Weighted back-projection reconstruction assuming different speed of sound of 1565 m/s for the mouse body and 1520 m/s in water surrounding the mouse; (d) Contrast enhancement with adaptive histogram equalization. (c) Application of the vesselness filter enhances contrast from vascular structures; (d) Background intensity suppression further enhances the image contrast.

6.4 Discussion

In this work, we report on a new small animal imaging platform, termed transmission-reflection optoacoustic ultrasound (TROPUS), for concomitant non-invasive mapping of the absorbed optical energy, acoustic reflectivity, speed of sound and acoustic attenuation in whole living mice with sub-millimeter resolution, further revealing the synergistic and complementary value of the newly developed multi-modal combination. *In vivo* mouse imaging experiments revealed fine details on the organ parenchyma, vascularization, tissue reflectivity, density and stiffness.

The diverse contrasts and superior imaging performance attained by TROPUS is of value for probing and quantification of multiple anatomical, functional and molecular properties in health and disease. For instance, speed of sound and acoustic attenuation are known to be altered by breast malignancies and other neoplastic lesions50. Pulse-echo US is also an accepted method for detecting changes in elastic properties in several types of tumors [75]. Both RUCT and OA enable imaging at high frame rates thus can render dynamic functional information, such as blood flow and distribution of oxygenated and deoxygenated hemoglobin [180]. Strong light absorption by melanin can be exploited to optoacoustically characterize skin lesions, circulating metastatic cells or lymph node metastases [200]. The use of contrast agents and genetic reporters [37, 202] can further en-

hance the versatility and molecular sensitivity of the multi-modal approach, potentially enabling new labeling and early disease detection approaches.

The information retrieved by one modality can be included as a prior knowledge to enhance reconstruction quality of the other modalities. Here we used the SoS values obtained with TUCT in a two-compartment model for improving the OA reconstructions. Going forward, incorporating the full map of heterogeneous speed of sound distribution may yield further improvements in the OA image quality [191, 205]. The AA and reflectivity maps can further be used for boosting the spatial resolution [87, 123] and removing artefacts [32] in the OA images. Indeed, it was observed that the statistical-weighting-based reconstruction approach could mitigate artefacts associated to acoustic heterogeneities and uneven light deposition in the object. The acoustically mismatched regions identified in RUCT images may potentially enable accurate modelling of scattering, refraction and other US propagation effects as part of a full-wave inversion (FWI) scheme to overcome the relatively low resolution achieved with bend-ray tracing methods in TUCT [77]. Finally, the US and OA data can be combined to allow for a more accurate localization of acoustic sources [169] and may also be used to mitigate the artifacts in the SoS maps for the bone and air regions. At present, exclusion of reflections in the TUCT-AA reconstructions has resulted in the edges between tissues exhibiting higher values, as they represent the combination of absorption and reflection in that region, similarly to the so-called "edge-enhancement" in phase-contrast X-ray CT [136]. In future work we aim at improving the TUCT algorithm by incorporating the full reflectivity information into the transmission reconstruction framework.

Beyond the small animal imaging domain, the TROPUS approach is of great interest for clinical translation. For one, integration of the well-established pulse-echo US imaging capability can facilitate clinical acceptance of the OA and TUCT methods. Recently, pilot clinical trials have demonstrated great value of the hybrid pulse-echo US and OA approach for the diagnosis of breast and skin cancer [42] as well as inflammatory bowel (Crohn's) disease6. Likewise, TUCT has shown great promise in the breast cancer diagnostics and screening applications [122].

In conclusion, the newly developed synergistic multi-modal combination offers unmatched capabilities for imaging diverse tissue properties and bio-markers with high resolution, penetration and contrast.

7 Conclusion and Outlook

With notable progress in hybrid multimodality imaging in the last decades [2] comes realization of the great potential for medical diagnosis achieved through the hybridization, primarily, by blending the anatomical and functional information [155].

Ultrasonography is a well-established modality that is used in everyday clinical practice as well as cutting-edge biomedical research. Its efficient combination with optoacoustic imaging may empower the hybrid method with highly complementary advantages of the versatile functional and molecular imaging capacities of optoacoustic tomography (OAT) in addition to the deep tissue morphological and functional imaging of US, thus open fascinating new prospects for medical and biological applications.

At the time this research project began, the multispectral optoacoustic tomography (MSOT) although has proven its versatile functional and molecular imaging capacities across multiple application areas, it has been almost exclusively used as a stand-alone modality. There are only few studies that demonstrate approaches to combine optoacoustic (OA) and pulse-echo ultrasound (US) imaging, however, all of them utilize the conventional linear array US detectors [102, 140, 144] and, therefore, are inefficient in recording of optoacoustically-induced signals [34].

The key objective that was accomplished in this work was to develop and optimize the instrumentation and algorithms for the first of its kind multimodal imaging system that supports optoacoustic, reflection (RUCT) and transmission (TUCT) ultrasound computed tomography and utilizes the concave ultrasound transducer (UT) detector arrays, that have proven to render a superior OA image quality as compared to the linear array approaches [38].

Based on the comprehensive analysis of the geometry related effects as well as image formation parameters with respect to their influence on both OA and US image quality, optimal selection of the array pitch size, tomographic coverage and spatial compounding parameters has been achieved (see Chapter 4). All the obtained results have the solid ground of numerical simulations and experimental validation.

We further showcased the imaging performance of the hybrid pre-clinical OA-US tomographic system in several *in vivo* mice experiments, by this, proving the general feasibility and the medical diagnostic relevance of the developed hybrid system for small animal imaging.

Accelerating clinical translation of the hybrid OA-US imaging is given a particular importance in this work. This objective found its practical realization in development of the handheld multi-segment UT detector array. The characterization of the imaging performance of this custom-built array, test of various image rendering strategies are described in Chapter 5, along with potentially relevant clinical application of imaging the blood flow and oxygen state in the carotid arteries with multi-segment probe in interleaved OA, pulse-echo US and/or color Doppler US modes. Another potential area of application where hybrid OA-US will add value is imaging of vasculature in upper and lower extremities for

assessment of blood supply in vessels that are relevant for diagnosis of peripheral arterial disease, diabetic foot, (autoimmune) vasculitis [188], and can be reliably identified on US image. Further potential applications in clinical diagnostics are foreseen in the areas of breast cancer [72], rheumatology [119], and dermatology [55].

Finally, for the first time to our knowledge, concomitant mapping of the absorbed optical energy, acoustic reflectivity, speed of sound and acoustic attenuation of *in vivo* biological tissues with sub-millimeter resolution was achieved in the developed trimodal imaging technique that combines optoacoustic, reflection- and transmission-mode ultrasound tomography (OAT-R/TUCT) and utilizes the full-ring UT detector array (see Chapter 6).

And as the research unfolds, the more questions arise, enabling us to give an outlook of the future research directions and unaddressed issues. Achieving ultimate high performance in terms of the reduction of the data rate and faster frame rate was not prioritized over image quality in this work, and, therefore, should be addressed in future, associated with in-depth exploration of patterned and compressed sensing approaches for optoacoustic and ultrasound detection [19, 129].

When considering employing the multi-segment array approach for imaging small animals, other illumination configurations may be considered in order to more uniformly illuminate the animal from multiple angles. In the current design, acoustically and optically transparent foil filled with water was used to ensure optimal coupling to the human body. Alternative coupling approaches can be specifically tailored for particular applications by considering the best trade-off between geometrical constraints of the different body parts and optimal placement of the imaged FOV. In addition, more advanced reconstruction methods, e.g. based on model-based inversion approaches [40, 165], may be further developed in order to enhance the reconstruction accuracy and overall image quality.

Complementarity of the optoacoustic and reflection/transmission ultrasound images was regarded only from the biological standpoint in this work as well as was exploited for image enhancement using dual speed-of-sound reconstruction based on sound velocity maps delivered by transmission ultrasonography. The multimodal aspect of the developed system providing access to hybrid images should be more actively explored in future and can be utilized, for instance, for quantitative correction and artefact reduction in OA images using available *a priori* information available from the reflection/transmission US images and/or raw signals. [158].

Another important aspect that should be prioritized in future work is the clinical translation and accelerated acceptance of the developed hybrid imaging approach that is impossible without a robust and validated for performance technology. The latter often requires the use of biologically relevant imaging phantoms for quality assurance of OA and US (incl. Doppler) performance, which when not commercially available or technically suitable need to be custom designed and manufactured.

We believe the conducted research will serve a good starting point for the development of the next generation of high-performance high-quality hybrid optoacoustic-ultrasound imaging platform that will revolutionize clinical practice by visualizing label-free anatomical, functional and molecular information of unsurpassed quality non-invasively *in vivo* and real-time.

List of publications

1. Elena Merčep, Joaquín López Herraiz, Xosé Luís Deán Ben, and Daniel Razansky. Transmission-reflection optoacoustic ultrasound (TROPUS) computed tomography of small animals. Light: Science & Applications, 8–18, January 2019.

2. Elena Merčep, Xosé Luís Deán Ben, and Daniel Razansky. Imaging of blood flow and oxygen state with a multi-segment optoacoustic ultrasound array. Photoacoustics, 10:48–53, June 2018.

3. Elena Merčep, Xosé Luís Deán Ben, and Daniel Razansky. Combined pulse-echo ultrasound and multispectral optoacoustic tomography with a multi-segment detector array. IEEE transactions on medical imaging, 36(10):2129–2137, October 2017.

4. Elena Merčep, Neal C. Burton, Jing Claussen, and Daniel Razansky. Whole-body live mouse imaging by hybrid reflection-mode ultrasound and optoacoustic tomography. Optics Letters, 40(20):4643–4646, October 2015.

5. Elena Merčep, Gency Jeng, Stefan Morscher, Pai-Chi Li, and Daniel Razansky. Hybrid optoacoustic tomography and pulse-echo ultrasonography using concave arrays. IEEE transactions on ultrasonics, ferroelectrics, and frequency control, 62(9):1651–1661, September 2015.

Other publications

1. Ivana Ivankovic, Elena Merčep, Claus-Georg Schmedt, Xosé Luís Deán Ben, and Daniel Razansky. Real-time volumetric assessment of the human carotid artery: handheld multispectral optoacoustic tomography. Radiology, 291(1):45–50, April 2019.

2. Xosé Luís Deán Ben, **Elena Merčep**, and Daniel Razansky. Hybrid-array-based optoacoustic and ultrasound (OPUS) imaging of biological tissues. Applied Physics Letters, 110(20):203703, May 2017.

3. Ivan Olefir, **Elena Merčep**, Neal C. Burton, Saak V. Ovsepian, and Vasilis Ntziachristos. Hybrid multispectral optoacoustic and ultrasound tomography for morphological and physiological brain imaging. Journal of Biomedical Optics, 21(8):86005, August 2016.

Conference contributions

1. Elena Merčep, Berkan Lafci, Stefan Morscher, Xosé Luís Deán Ben, and Daniel Razansky. Quantitative image correction using semi- and fully-automatic segmentation of hybrid optoacoustic and ultrasound images. Poster presented at Biophotonics Congress: Biomedical Optics, Hollywood, USA, April 3–6, 2018.

2. Mailyn Pérez-Liva, J. M. Udías, Jorge Camacho, **Elena Merčep**, Joaquin López Herraiz. Real-time ultrasound transmission tomography based on Bézier curves. Oral presentation given at International Workshop on Medical Ultrasound Tomography, Speyer, Germany, November 1–3, 2017.

3. Elena Merčep, Xosé Luís Deán Ben, Neal C. Burton, and Daniel Razansky. Hybrid Optoacoustic and ultrasound imaging system with a multi-segment detector array. Oral presentation given at International Workshop on Medical Ultrasound Tomography, Speyer, Germany, November 1–3, 2017.

4. Elena Merčep, Xosé Luís Deán Ben, Neal C. Burton, and Daniel Razansky. Multi-segment detector array for hybrid reflection-mode ultrasound and optoacoustic tomography. Oral presentation given at SPIE Photonics West Conference, San Francisco, USA, January 28–February 2, 2017.

5. Elena Merčep, Gency Jeng, Stefan Morscher, Pai-Chi Li, and Daniel Razansky. Development and optimization of transmission ultrasound tomography using concave arrays. Poster presented at World Molecular Imaging Congress, New York, USA, September 7–10, 2016.

6. Elena Merčep, Neal C. Burton, Benjamin Johnson, Josefine Reber, Jing Claussen, and Daniel Razansky. Contrast enhanced ultrasound in combination with multispectral optoacoustic tomography for whole-body mouse imaging. Poster presented at World Molecular Imaging Congress, New York, USA, September 7–10, 2016.

7. Elena Merčep, Neal C. Burton, Benjamin Johnson, Josefine Reber, Jing Claussen, and Daniel Razansky. Hybrid reflection-mode ultrasound and optoacoustic tomography for whole-body live mouse imaging. Oral presentation given at European Molecular Imaging Meeting, Utrecht, Netherlands, March 8–10, 2016.

8. Elena Nasonova, Gency Jeng, Stefan Morscher, Pai-Chi Li, and Daniel Razansky. Whole-body live mouse imaging by hybrid reflection-mode ultrasound and optoacoustic tomography. Oral presentation given at the 15th Meeting of the Interdisciplinary German Network Molecular Imaging, Freiburg, Germany, October 14–16, 2015.

9. Elena Nasonova, Gency Jeng, Stefan Morscher, Pai-Chi Li, and Daniel Razansky. Optimized image generation with hybrid optoacoustic ultrasound system using concave arrays. Poster presented at World Molecular Imaging Congress, Honolulu, Havaii, September 2–5, 2015.

10. Elena Nasonova [1], Neal C. Burton, Benjamin Johnson, Josefine Reber, Jing Claussen, and Daniel Razansky. Whole-body live mouse imaging by hybrid reflection-mode ultrasound and optoacoustic tomography. Oral presentation given at European Molecular Imaging Meeting, Tübingen, Germany, March 18–20, 2015.

[1] Maiden name

Acknowledgments

This work is a result of the joint collaborative research led by Institute for Biological and Medical Imaging and iThera Medical GmbH, and I am grateful to members of the both teams and in particular would like to acknowledge: my supervisor Prof. Dr. Daniel Razansky for his constructive inspiring feedback and outstanding guidance throughout the project, my truly exemplary and visionary mentor Dr. Xosé Luís Deán Ben for his continued support and help in design of experiments and tools, my second advisor Prof. Dr. Fabian Theis, and my collegues from iThera Medical: Josef Konradl, Stefan Morscher, Alexander Urich, Neal C. Burton, Jing Claussen, Clinton Hupple, Antonia Longo, Till Gradinger, Ruben Moreno and Marcin Kacprowicz. I would like to further express gratitude to Dr. Joaquín López Herraiz (University Complutense of Madrid), for the fruitful collaboration and generously sharing his time and expertise in the field of ultrasound transmission tomography. I would like to acknowledge the team of S-Sharp corporation for their efforts in development the research ultrasound platform, and Prof. Dr. Pai-Chi Li and Dr. Gency Jeng for their extensive contributions and outstanding support. I would like to thank the management team of iThera Medical - the CEO Christian Wiest and CFO Dr. Philipp Bell for facilitating this unique opportunity of embarking on the research project in the company as well as giving me the opportunity to attend conferences, meet so many interesting people, and work in colloboration with the industry partners (among those I am particularly grateful to Rayfos Ltd, Falkenstein Mikrosysteme GmbH, InnoLas Solutions GmbH, and Imasonic SAS). Furthermore I would like to thank all the members of the Institute of Biological and Medical Imaging of the Helmholtz Center Munich headed by Prof. Dr. Vasilis Ntziachristos for the insightful discussions and support. In particular, I am thankful to Ivana Ivankovic, Sarah Glasl, Uwe Klemm, and Michael Reiss. My research here would be impossible without support of my friends, positive attitude and love of my family – my husband Ljubo, my beloved parents Larisa and Alexandr, my brother Oleg, sister-in-law Lana and nephew Stepan. They are always willing to listen and share both my worries and victories. Thank you.

Bibliography

[1] American National Standard for Safe Use of Lasers in Health Care Facilities. Standard Z136.1–2000. Technical Report Standard Z136.1–2000, 2007.

[2] In vivo imaging today and tomorrow: How multimodality imaging is driving translational research, January 2017.

[3] Andres Aguirre, Puyun Guo, John Gamelin, Shikui Yan, Mary M. Sanders, Molly Brewer, and Quing Zhu. Coregistered three-dimensional ultrasound and photoacoustic imaging system for ovarian tissue characterization. *Journal of Biomedical Optics*, 14(5):054014, October 2009.

[4] Paul L. Allan, Grant M. Baxter, and Michael J. Weston. *Clinical Ultrasound, 2-Volume Set E-Book: Expert Consult: Online and Print*. Elsevier Health Sciences, March 2011.

[5] Thomas J. Allen and Paul C. Beard. Optimising the detection parameters for deep-tissue photoacoustic imaging. In *Photons Plus Ultrasound: Imaging and Sensing 2012*, volume 8223, page 82230P. International Society for Optics and Photonics, February 2012.

[6] Anders H. Andersen. A ray tracing approach to restoration and resolution enhancement in experimental ultrasound tomography. *Ultrasonic Imaging*, 12(4):268–291, October 1990.

[7] Bjørn A. J. Angelsen. *Ultrasound imaging : waves, signals, and signal processing. 2. Propagation and scattering in heterogeneous, nonlinear tissue with contrast agent imaging and Doppler measurements*. Emantec, 2000.

[8] Bjørn A. J. Angelsen, Hans Torp, Sverre Holm, Kjell Kristoffersen, and T. A. Whittingham. Which transducer array is best? *European Journal of Ultrasound*, 2(2):151–164, April 1995.

[9] M. Baer and U. Kradolfer. An automatic phase picker for local and teleseismic events. *Bulletin of the Seismological Society of America*, 77(4):1437–1445, August 1987.

[10] Paul Beard. Biomedical photoacoustic imaging. *Interface Focus*, 1(4):602–631, June 2011.

[11] Vera Behar. Beam profile evaluation in spatial compound imaging. *Comptes Rendus de l'Academie Bulgare des Sciences*, 55:5:37, 2002.

[12] Alexander Graham Bell. *Upon the production of sound by radiant energy*. Washington, Gibson Brothers, printers, 1881.

[13] David A. Boas, Dana H. Brooks, Eric L. Miller, Charles A. DiMarzio, Misha Kilmer, Richard J. Gaudette, and Quan Zhang. Imaging the body with diffuse optical tomography. *IEEE Signal Processing Magazine*, 18(6):57–75, November 2001.

[14] Andreas Buehler, Marcin Kacprowicz, Adrian Taruttis, and Vasilis Ntziachristos. Real-time handheld multispectral optoacoustic imaging. *Optics Letters*, 38(9):1404–1406, May 2013.

[15] Andreas Buehler, Amir Rosenthal, Thomas Jetzfellner, Alexander Dima, Daniel Razansky, and Vasilis Ntziachristos. Model-based optoacoustic inversions with incomplete projection data. *Medical Physics*, 38(3):1694–1704, March 2011.

[16] Neal C. Burton, Manishkumar Patel, Stefan Morscher, Wouter H. P. Driessen, Jing Claussen, Nicolas Beziere, Thomas Jetzfellner, Adrian Taruttis, Daniel Razansky, Bohumil Bednar, and Vasilis Ntziachristos. Multispectral opto-acoustic tomography (MSOT) of the brain and glioblastoma characterization. *NeuroImage*, 65:522–528, January 2013.

[17] E. L. Carstensen. The mechanism of the absorption of ultrasound in biological materials. *IRE transactions on medical electronics*, ME-7:158–162, July 1960.

[18] Nitin Chaubal. Ultrasound of Pancreas. *Ultrasound in Medicine and Biology*, 41(4):S5, April 2015.

[19] Tanya Chernyakova and Yonina C. Eldar. Fourier-domain beamforming: the path to compressed ultrasound imaging. *IEEE Transactions on Ultrasonics, Ferroelectrics, and Frequency Control*, 61(8):1252–1267, August 2014.

[20] Peter L. Choyke. Diagnosing prostate cancer with image fusion (MRI, PET, CT, US). *Cancer Research*, 72(4):IA23, February 2012.

[21] Yong Eun Chung and Ki Whang Kim. Contrast-enhanced ultrasonography: advance and current status in abdominal imaging. *Ultrasonography (Seoul, Korea)*, 34(1):3–18, January 2015.

[22] Wikipedia contributors. Doppler ultrasonography, April 2018. Page Version ID: 835636980.

[23] Joseph Culver, Walter Akers, and Samuel Achilefu. Multimodality molecular imaging with combined optical and SPECT/PET modalities. *Journal of Nuclear Medicine: Official Publication, Society of Nuclear Medicine*, 49(2):169–172, February 2008.

[24] Laura Curiel, Rajiv Chopra, and Kullervo Hynynen. Progress in multimodality imaging: truly simultaneous ultrasound and magnetic resonance imaging. *IEEE transactions on medical imaging*, 26(12):1740–1746, December 2007.

[25] Xianjin Dai, Hao Yang, Tianqi Shan, HuiKai Xie, Scott A. Berceli, and Huabei Jiang. Miniature Endoscope for Multimodal Imaging. *ACS Photonics*, 4(1):174–180, January 2017.

[26] Xosé Luís Deán-Ben, Erwin Bay, and Daniel Razansky. Functional optoacoustic imaging of moving objects using microsecond-delay acquisition of multispectral three-dimensional tomographic data. *Scientific Reports*, 4:5878, July 2014.

[27] Xosé Luís Deán-Ben, Thomas F. Fehm, Steven J. Ford, Sven Gottschalk, and Daniel Razansky. Spiral volumetric optoacoustic tomography visualizes multi-scale dynamics in mice. *Light: Science & Applications*, 6(4):e16247, April 2017.

[28] Xosé Luís Deán-Ben, Thomas F. Fehm, Monika Gostic, and Daniel Razansky. Volumetric hand-held optoacoustic angiography as a tool for real-time screening of dense breast. *Journal of Biophotonics*, 9(3):253–259, March 2016.

[29] Xosé Luís Deán-Ben, Steven James Ford, and Daniel Razansky. High-frame rate four dimensional optoacoustic tomography enables visualization of cardiovascular dynamics and mouse heart perfusion. *Scientific Reports*, 5, July 2015.

[30] Xosé Luís Deán-Ben, R. Ma, Daniel Razansky, and Vasilis Ntziachristos. Statistical Approach for Optoacoustic Image Reconstruction in the Presence of Strong Acoustic Heterogeneities. *IEEE Transactions on Medical Imaging*, 30(2):401–408, February 2011.

[31] Xosé Luís Deán-Ben, Elena Merčep, and Daniel Razansky. Hybrid-array-based optoacoustic and ultrasound (OPUS) imaging of biological tissues. *Applied Physics Letters*, 110(20):203703, May 2017.

[32] Xosé Luís Deán-Ben, Vasilis Ntziachristos, and Daniel Razansky. Effects of small variations of speed of sound in optoacoustic tomographic imaging. *Medical Physics*, 41(7):073301, July 2014.

[33] Xosé Luís Deán-Ben and Daniel Razansky. Functional optoacoustic human angiography with handheld video rate three dimensional scanner. *Photoacoustics*, 1(3–4):68–73, December 2013.

[34] Xosé Luís Deán-Ben and Daniel Razansky. Adding fifth dimension to optoacoustic imaging: volumetric time-resolved spectrally enriched tomography. *Light: Science & Applications*, 3(1):e137, January 2014.

[35] Xosé Luís Deán-Ben and Daniel Razansky. On the link between the speckle free nature of optoacoustics and visibility of structures in limited-view tomography. *Photoacoustics*, 4(4):133–140, December 2016.

[36] Thomas Deffieux, Charlie Demene, Mathieu Pernot, and Mickael Tanter. Functional ultrasound neuroimaging: a review of the preclinical and clinical state of the art. *Current Opinion in Neurobiology*, 50:128–135, June 2018.

[37] Nikolaos C. Deliolanis, Angelique Ale, Stefan Morscher, Neal C. Burton, Karin Schaefer, Karin Radrich, Daniel Razansky, and Vasilis Ntziachristos. Deep-tissue reporter-gene imaging with fluorescence and optoacoustic tomography: a performance overview. *Molecular imaging and biology: MIB: the official publication of the Academy of Molecular Imaging*, 16(5):652–660, October 2014.

[38] Alexander Dima and Vasilis Ntziachristos. Non-invasive carotid imaging using optoacoustic tomography. *Optics Express*, 20(22):25044–25057, October 2012.

[39] Alexander Dima and Vasilis Ntziachristos. In-vivo handheld optoacoustic tomography of the human thyroid. *Photoacoustics*, 4(2):65–69, June 2016.

[40] Lu Ding, Xosé Luís Deán-Ben, Christian Lutzweiler, Daniel Razansky, and Vasilis Ntziachristos. Efficient non-negative constrained model-based inversion in optoacoustic tomography. *Physics in Medicine and Biology*, 60(17):6733–6750, September 2015.

[41] U. S. Dinish, Chris Jun Hui Ho, Josefine Reber, Vasilis Ntziachristos, Malini Olivo, Neal Burton, and Stefan Morscher. Advances in Optoacoustic Imaging: From Benchside to Clinic. July 2015.

[42] Gael Diot, Stephan Metz, Aurelia Noske, Evangelos Liapis, Barbara Schroeder, Saak V. Ovsepian, Reinhard Meier, Ernst Rummeny, and Vasilis Ntziachristos. Multispectral Optoacoustic Tomography (MSOT) of Human Breast Cancer. *Clinical Cancer Research: An Official Journal of the American Association for Cancer Research*, 23(22):6912–6922, November 2017.

[43] Vikram S. Dogra, Bhargava K. Chinni, Keerthi S. Valluru, Jacob Moalem, Ellen J. Giampoli, Katie Evans, and Navalgund A. Rao. Preliminary results of ex vivo multispectral photoacoustic imaging in the management of thyroid cancer. *AJR. American journal of roentgenology*, 202(6):W552–558, June 2014.

[44] Christian Doppler and Frantisek Josef Studnicka. *Ueber das farbige Licht der Doppelsterne und einiger anderer gestirne des Himmels.* Prag K. Böhm, 1903.

[45] Francis A. Duck. *Physical Properties of Tissue: A Comprehensive Reference Book*. Academic Press, 1990.

[46] Neb Duric. WE-G-210-02: Ultrasound Tomography: A Breast Imaging Modality Whose Time Has Come. *Medical Physics*, 42(6Part41):3699–3699, 2015.

[47] Karl Theo Dussik. über die Möglichkeit, hochfrequente mechanische Schwingungen als diagnostisches Hilfsmittel zu verwerten. *Zeitschrift fuer die gesamte Neurologie und Psychiatrie*, 174(1):153–168, December 1942.

[48] Robert Ellwood, Olumide Ogunlade, Edward Zhang, Paul Beard, and Ben Cox. Photoacoustic tomography using orthogonal Fabry-Pérot sensors. *Journal of Biomedical Optics*, 22(4):41009, April 2017.

[49] S. A. Ermilov, R. Su, A. Conjusteau, F. Anis, V. Nadvoretskiy, M. A. Anastasio, and A. A. Oraevsky. Three-Dimensional Optoacoustic and Laser-Induced Ultrasound Tomography System for Preclinical Research in Mice: Design and Phantom Validation. *Ultrasonic Imaging*, June 2015.

[50] Claudia Errico, Juliette Pierre, Sophie Pezet, Yann Desailly, Zsolt Lenkei, Olivier Couture, and Mickael Tanter. Ultrafast ultrasound localization microscopy for deep super-resolution vascular imaging. *Nature*, 527(7579):499–502, November 2015.

[51] Héctor Estrada, Xiao Huang, Johannes Rebling, Michael Zwack, Sven Gottschalk, and Daniel Razansky. Virtual craniotomy for high-resolution optoacoustic brain microscopy. *Scientific Reports*, 8(1):1459, January 2018.

[52] Thomas Felix Fehm, Xosé Luís Deán-Ben, and Daniel Razansky. Four dimensional hybrid ultrasound and optoacoustic imaging via passive element optical excitation in a hand-held probe. *Applied Physics Letters*, 105(17):173505, October 2014.

[53] Thomas Felix Fehm, Xosé Luís Deán-Ben, Steven James Ford, and Daniel Razansky. In vivo whole-body optoacoustic scanner with real-time volumetric imaging capacity. *Optica*, 3(11):1153–1159, November 2016.

[54] Richard Feynman. *The Feynman Lectures on Physics Vol. I Ch. 47: Sound. The wave equation*, volume I. Addison Publishing Company, 1969.

[55] Steven J. Ford, Paul L. Bigliardi, Thomas C. P. Sardella, Alexander Urich, Neal C. Burton, Marcin Kacprowicz, Mei Bigliardi, Malini Olivo, and Daniel Razansky. Structural and Functional Analysis of Intact Hair Follicles and Pilosebaceous Units by Volumetric Multispectral Optoacoustic Tomography. *The Journal of Investigative Dermatology*, 136(4):753–761, April 2016.

[56] S. Forte, S. Dellas, B. Stieltjes, and B. Bongartz. Multimodal ultrasound tomography for breast imaging: a prospective study of clinical feasibility. *European Radiology Experimental*, 1:27, December 2017.

[57] Mark Fournelle, Hans J. Welsch, Heinrich Fonfara, Holger Hewener, Christian Günther, Wolfgang Bost, and Robert Lemor. High-contrast real-time optoacoustic imaging of subcutaneous blood vessels. In *World Congress on Medical Physics and Biomedical Engineering, September 7 - 12, 2009, Munich, Germany*, IFMBE Proceedings, pages 352–355. Springer, Berlin, Heidelberg, 2009. DOI: 10.1007/978-3-642-03879-2_100.

[58] Alejandro F. Frangi, Wiro J. Niessen, Koen L. Vincken, and Max A. Viergever. Multiscale vessel enhancement filtering. In *Medical Image Computing and Computer-Assisted Intervention*, volume 1496, pages 130–137, Berlin, Germany, 1998. Springer Verlag.

[59] Jerome Gateau, Miguel Angel Araque Caballero, Alexander Dima, and Vasilis Ntziachristos. Three-dimensional optoacoustic tomography using a conventional ultrasound linear detector array: whole-body tomographic system for small animals. *Medical Physics*, 40(1):013302, January 2013.

[60] Marco Gerling, Ying Zhao, Salvatore Nania, K. Jessica Norberg, Caroline S. Verbeke, Benjamin Englert, Raoul V. Kuiper, Asa Bergström, Moustapha Hassan, Albrecht Neesse, J. Matthias Löhr, and Rainer L. Heuchel. Real-time assessment of tissue hypoxia in vivo with combined photoacoustics and high-frequency ultrasound. *Theranostics*, 4(6):604–613, 2014.

[61] Robert W. Gill. *The Physics and Technology of Diagnostic Ultrasound: Study Guide*. High Frequency Publishing, September 2016.

[62] Jürgen Glatz, Nikolaos C. Deliolanis, Andreas Buehler, Daniel Razansky, and Vasilis Ntziachristos. Blind source unmixing in multi-spectral optoacoustic tomography. *Optics Express*, 19(4):3175–3184, February 2011.

[63] Carri Glide, Nebojsa Duric, and Peter Littrup. Novel approach to evaluating breast density utilizing ultrasound tomography. *Medical Physics*, 34(2):744–753, February 2007.

[64] Albert Goldstein. Slice thickness measurements. *Journal of Ultrasound in Medicine: Official Journal of the American Institute of Ultrasound in Medicine*, 7(9):487–498, September 1988.

[65] Sven Gottschalk, Thomas Felix Fehm, Xosé Luís Deán-Ben, Vassiliy Tsytsarev, and Daniel Razansky. Correlation between volumetric oxygenation responses and electrophysiology identifies deep thalamocortical activity during epileptic seizures. *Neurophotonics*, 4(1), January 2017.

[66] J. F. Greenleaf and A. Alizad. Measurement of tissue viscoelasticity with ultrasound. In *Optical Elastography and Tissue Biomechanics IV*, volume 10067, page 1006705. International Society for Optics and Photonics, February 2017.

[67] James F. Greenleaf, Sahvanna A. Johnson, So L. Lee, Gabor T. Herman, and E. H. Wood. Algebraic Reconstruction of Spatial Distributions of Acoustic Absorption within Tissue from Their Two-Dimensional Acoustic Projections. In *Acoustical Holography*, pages 591–603. Springer, Boston, MA, 1974.

[68] James F. Greenleaf, Steven A. Johnson, and Arnold H. Lent. Measurement of spatial distribution of refractive index in tissues by ultrasonic computer assisted tomography. *Ultrasound in Medicine & Biology*, 3(4):327–339, January 1978.

[69] Sandra L. Hagen-Ansert. *Textbook of Diagnostic Sonography - E-Book: 2-Volume Set*. Elsevier Health Sciences, August 2013.

[70] Andrew M Handorf, Yaxian Zhou, Matthew A Halanski, and Wan-Ju Li. Tissue Stiffness Dictates Development, Homeostasis, and Disease Progression. *Organogenesis*, 11(1):1–15, April 2015.

[71] Hailong He, Georg Wissmeyer, Saak V. Ovsepian, Andreas Buehler, and Vasilis Ntziachristos. Optoacoustic endoscopy with optical and acoustic resolution. In *Photons Plus Ultrasound: Imaging and Sensing 2017*, volume 10064, page 100641C. International Society for Optics and Photonics, March 2017.

[72] Michelle Heijblom, Daniele Piras, Mariël Brinkhuis, Johan C. G. van Hespen, Frank M. van den Engh, Margreet van der Schaaf, Joost M. Klaase, Ton G. van Leeuwen, Wiendelt Steenbergen, and Saranjay Manohar. Photoacoustic image patterns of breast carcinoma and comparisons with Magnetic Resonance Imaging and vascular stained histopathology. *Scientific Reports*, 5:11778, July 2015.

[73] Sverre Holm. Digital beamforming in ultrasound imaging. *Proc. Nordic Signal Processing Symposium, Alesund, Norway*, 1994.

[74] San-Fu Hong, Yu-Shih Lai, Kwo-Whei Lee, and Mu-Kuan Chen. Efficiency of three-dimensional Doppler ultrasonography in assessing nodal metastasis of head and neck cancer. *European archives of otorhinolaryngology: official journal of the European Federation of Otorhinolaryngological Societies (EUFOS)*, September 2014.

[75] Kenneth Hoyt, Benjamin Castaneda, Man Zhang, Priya Nigwekar, P. Anthony di Sant'Agnese, Jean V. Joseph, John Strang, Deborah J. Rubens, and Kevin J. Parker. Tissue elasticity properties as biomarkers for prostate cancer. *Cancer biomarkers : section A of Disease markers*, 4(4-5):213–225, 2008.

[76] Bin Huang, Jun Xia, Konstantin Maslov, and Lihong V. Wang. Improving limited-view photoacoustic tomography with an acoustic reflector. *Journal of Biomedical Optics*, 18(11):110505, November 2013.

[77] Peter Huthwaite and Francesco Simonetti. A practical, robust approach to high resolution ultrasonic breast tomography. *The Journal of the Acoustical Society of America*, 135(4):2178–2178, April 2014.

[78] Johan Huygh, Yannick Peeters, Jelle Bernards, and Manu L. N. G. Malbrain. Hemodynamic monitoring in the critically ill: an overview of current cardiac output monitoring methods. *F1000Research*, 5, December 2016.

[79] Nicusor Iftimia, R. Daniel Ferguson, Mircea Mujat, Ankit H. Patel, Ellen Ziyi Zhang, William Fox, and Milind Rajadhyaksha. Combined reflectance confocal microscopy/optical coherence tomography imaging for skin burn assessment. *Biomedical Optics Express*, 4(5):680–695, April 2013.

[80] ANSI-American National Standards Institute. Workplace Safety Standards.

[81] Michael Jaeger, Jeffrey C. Bamber, and Martin Frenz. Clutter elimination for deep clinical optoacoustic imaging using localised vibration tagging (LOVIT). *Photoacoustics*, 1(2):19–29, May 2013.

[82] Jørgen A. Jensen. Ultrasound Imaging and Its Modeling. In *Imaging of Complex Media with Acoustic and Seismic Waves*, Topics in Applied Physics, pages 135–166. Springer, Berlin, Heidelberg, 2002.

[83] Jorgen Arendt Jensen. FIELD: A Program for Simulating Ultrasound Systems. In *10th Nordicbaltic conference on biomedical imaging, Vol. 4, Supplement 1, Part 1:351–353*, pages 351–353, 1996.

[84] Jorgen Arendt Jensen, Svetoslav Ivanov Nikolov, Kim Løkke Gammelmark, and Morten Høgholm Pedersen. Synthetic aperture ultrasound imaging. *Ultrasonics*, 44 Suppl 1:5–15, December 2006.

[85] Søren K. Jespersen, Jens E. Wilhjelm, and Henrik Sillesen. Multi-angle compound imaging. *Ultrasonic Imaging*, 20(2):81–102, April 1998.

[86] Don H. Johnson and Dan E. Dudgeon. *Array Signal Processing: Concepts and Techniques*. Prentice Hall, Englewood Cliffs, NJ, 1 edition edition, February 1993.

[87] Jithin Jose, Rene G. H. Willemink, Wiendelt Steenbergen, C. H. Slump, Ton G. van Leeuwen, and Srirang Manohar. Speed-of-sound compensated photoacoustic tomography for accurate imaging. *Medical Physics*, 39(12):7262–7271, December 2012.

[88] Thomas Kahn and Harald Busse. *Interventional Magnetic Resonance Imaging*. Springer, Heidelberg, 2012 edition, August 2012.

[89] Thomas Kahn and Harald Busse, editors. *Interventional Magnetic Resonance Imaging*. Diagnostic Imaging. Springer-Verlag, Berlin Heidelberg, 2012.

[90] Avinash C. Kak and Malcolm Slaney. *Principles of Computerized Tomographic Imaging*. Society for Industrial and Applied Mathematics, Philadelphia, January 1987.

[91] Erol Kalkan. An automatic P-Phase arrival-time picker. *Bulletin of the Seismological Society of America*, 106(3):971986, 2016. IP-062691.

[92] Mustafa Karaman, Pai-Chi Li, and M. O'Donnell. Synthetic aperture imaging for small scale systems. *IEEE Transactions on Ultrasonics, Ferroelectrics, and Frequency Control*, 42(3):429–442, May 1995.

[93] John J. P. Kastelein and Eric de Groot. Ultrasound imaging techniques for the evaluation of cardiovascular therapies. *European Heart Journal*, 29(7):849–858, April 2008.

[94] Edmund Kenneth Kerut, Elizabeth F. McLlwain, and Gary D. Plotnick. *Handbook of Echo-Doppler Interpretation*. John Wiley & Sons, Elmsford, N.Y, 0002 edition, March 2004.

[95] Chunwoo Kim, Doyoung Chang, Doru Petrisor, Gregory Chirikjian, Misop Han, and Dan Stoianovici. Ultrasound probe and needle-guide calibration for robotic ultrasound scanning and needle targeting. *IEEE transactions on bio-medical engineering*, 60(6):1728–1734, June 2013.

[96] Kang-Sik Kim. Insana Lab: Ultrasonic Imaging - The University of Illinois at Urbana-Champaign.

[97] Seonmun Kim, Sungwon Lee, Hyun Seok Choi, So-Lyung Jung, Kook-Jin Ahn, and Bum-soo Kim. Pseudostenosis at the Origin of the Vertebral Artery on Contrast-enhanced MRA: Correlation with Aortic Motion on Dynamic 3d Time-Resolved Contrast-Enhanced MRA. *Journal of the Korean Society of Magnetic Resonance in Medicine*, 16:236, January 2012.

[98] Lawrence Edward Kinsler and Austin Rogers Frey. *Fundamentals of Acoustics*. J. Wiley & Sons, January 1962.

[99] Johan Kirkhorn. *Introduction to IQ-demodulation of RF-data*. PhD thesis, IFBT, NTNU, September 1999.

[100] Mendel Kleiner. *Electroacoustics*. CRC Press, Boca Raton, FL, 1 edition edition, February 2013.

[101] Ferdinand Knieling, Clemens Neufert, Arndt Hartmann, Jing Claussen, Alexander Urich, Cornelia Egger, Marcel Vetter, Sarah Fischer, Lukas Pfeifer, Alexander Hagel, Christian Kielisch, Rüdiger S. Görtz, Dane Wildner, Matthias Engel, Jens Röther, Wolfgang Uter, Jürgen Siebler, Raja Atreya, Wolfgang Rascher, Deike Strobel, Markus F. Neurath, and Maximilian J. Waldner. Multispectral Optoacoustic Tomography for Assessment of Crohn's Disease Activity. *The New England Journal of Medicine*, 376(13):1292–1294, 2017.

[102] Roy G. M. Kolkman, Peter J. Brands, Wiendelt Steenbergen, and Ton G. van Leeuwen. Real-time in vivo photoacoustic and ultrasound imaging. *Journal of Biomedical Optics*, 13(5):050510, October 2008.

[103] R. Krimholtz, D. A. Leedom, and G. L. Matthaei. New equivalent circuits for elementary piezoelectric transducers. *Electronics Letters*, 6(13):398–399, June 1970.

[104] Martin Krueger, Andreas Pesavento, and Helmut Ermert. A modified time-of-flight tomography concept for ultrasonic breast imaging. In *1996 IEEE Ultrasonics Symposium. Proceedings*, volume 2, pages 1381–1385 vol.2, November 1996.

[105] Gerrit Cornelis Langhout, Diederik Johannes Grootendorst, Omgo Edo Nieweg, Michel Wilhelmus Jacobus Maria Wouters, Jos Alexander van der Hage, Jithin Jose, Hester van Boven, Wiendelt Steenbergen, Srirang Manohar, and Theodoor Jacques Marie Ruers. Detection of melanoma metastases in resected human lymph nodes by noninvasive multispectral photoacoustic imaging. *International Journal of Biomedical Imaging*, 2014:163652, 2014.

[106] Mark W. Lenox, James Wiskin, Matthew A. Lewis, Stephen Darrouzet, David Borup, and Scott Hsieh. Imaging Performance of Quantitative Transmission Ultrasound. *International Journal of Biomedical Imaging*, 2015:454028, 2015.

[107] Deborah Levine. Use of ultrasound as an alternative to CT. Technical report, Beth Israel-Deaconess Medical Center, Boston, MA, November 2010.

[108] Changhui Li and Lihong V. Wang. Photoacoustic tomography and sensing in biomedicine. *Physics in medicine and biology*, 54(19):R59–R97, October 2009.

[109] Cuiping Li, Neb Duric, and Lianjie Huang. Comparison of ultrasound attenuation tomography methods for breast imaging. *Proceedings of SPIE - The International Society for Optical Engineering*, March 2008.

[110] Cuiping Li, Neb Duric, Peter Littrup, and Lianjie Huang. In Vivo breast sound-speed imaging with ultrasound tomography. *Ultrasound in medicine & biology*, 35(10):1615–1628, October 2009.

[111] Cuiping Li, Lianjie Huang, Neb Duric, Haijiang Zhang, and Charlotte Rowe. An improved automatic time-of-flight picker for medical ultrasound tomography. *Ultrasonics*, 49(1):61–72, January 2009.

[112] Lei Li, Liren Zhu, Cheng Ma, Li Lin, Junjie Yao, Lidai Wang, Konstantin Maslov, Ruiying Zhang, Wanyi Chen, Junhui Shi, and Lihong V. Wang. Single-impulse

panoramic photoacoustic computed tomography of small-animal whole-body dynamics at high spatiotemporal resolution. *Nature Biomedical Engineering*, 1(5):s41551–017–0071–017, May 2017.

[113] Mucong Li, Yuqi Tang, and Junjie Yao. Photoacoustic tomography of blood oxygenation: A mini review. *Photoacoustics*, 10:65–73, June 2018.

[114] Pai-Chi Li, Churng-Ren Chris Wang, Dar-Bin Shieh, Chen-Wei Wei, Chao-Kang Liao, Carolina Poe, Suwen Jhan, Ann-Ann Ding, and Ya-Na Wu. In vivo photoacoustic molecular imaging with simultaneous multiple selective targeting usingantibody-conjugated gold nanorods. *Optics Express*, 16(23):18605–18615, November 2008.

[115] Shengying Li, Marcel Jackowski, Donald P. Dione, Trond Varslot, Lawrence H. Staib, and Klaus Mueller. Refraction corrected transmission ultrasound computed tomography for application in breast imaging. *Medical Physics*, 37(5):2233–2246, May 2010.

[116] Li Shengying, Jackowski Marcel, Dione Donald P., Varslot Trond, Staib Lawrence H., and Mueller Klaus. Refraction corrected transmission ultrasound computed tomography for application in breast imaging. *Medical Physics*, 37(5):2233–2246, April 2010.

[117] Fredrik Lingvall. *Time-domain Reconstruction Methods for Ultrasonic Array Imaging A Statistical Approach - Semantic Scholar*. PhD thesis, UPPSALA UNIVERSITY, 2004.

[118] Jian Y. Lu, Hehong Zou, and James F. Greenleaf. Biomedical ultrasound beam forming. *Ultrasound in Medicine & Biology*, 20(5):403–428, 1994.

[119] Christian Lutzweiler, Reinhard Meier, Ernst Rummeny, Vasilis Ntziachristos, and Daniel Razansky. Real-time optoacoustic tomography of indocyanine green perfusion and oxygenation parameters in human finger vasculature. *Optics Letters*, 39(14):4061–4064, July 2014.

[120] Jieming Ma, Kerem Karadayi, Murtaza Ali, and Yongmin Kim. Ultrasound phase rotation beamforming on multi-core DSP. *Ultrasonics*, 54(1):99–105, January 2014.

[121] Robert J. Mailloux. *Phased Array Antenna Handbook, Second Edition*. Artech Print on Demand, Boston, 2 edition edition, March 2005.

[122] Bilal Malik, John Klock, James Wiskin, and Mark Lenox. Objective breast tissue image classification using Quantitative Transmission ultrasound tomography. *Scientific Reports*, 6:38857, December 2016.

[123] Subhamoy Mandal, Xosé Luís Deán-Ben, and Daniel Razansky. Visual Quality Enhancement in Optoacoustic Tomography Using Active Contour Segmentation Priors. *IEEE Transactions on Medical Imaging*, 35(10):2209–2217, October 2016.

[124] Wojciech Marczak. Water as a standard in the measurements of speed of sound in liquids. *The Journal of the Acoustical Society of America*, 102(5):2776–2779, November 1997.

[125] Dev Maulik. Physical Principles of Doppler Ultrasonography. In *Doppler Ultrasound in Obstetrics and Gynecology*, pages 9–17. Springer, Berlin, Heidelberg, 2005.

[126] Dev Maulik. Sonographic Color Flow Mapping: Basic Principles. In *Doppler Ultrasound in Obstetrics and Gynecology*, pages 69–84. Springer, Berlin, Heidelberg, 2005.

[127] Michael C McDaniel, Parham Eshtehardi, Fadi J Sawaya, John S Douglas, Jr, and Habib Samady. Contemporary clinical applications of coronary intravascular ultrasound. *JACC. Cardiovascular interventions*, 4(11):1155–1167, November 2011.

[128] Christopher M. Kramer MD. *Multimodality Imaging in Cardiovascular Medicine*. Demos Medical Publishing, October 2010.

[129] Jing Meng, Lihong V. Wang, Leslie Ying, Dong Liang, and Liang Song. Compressed-sensing photoacoustic computed tomography in vivo with partially known support. *Optics Express*, 20(15):16510–16523, July 2012.

[130] Elena Merčep, Neal C. Burton, Jing Claussen, and Daniel Razansky. Whole-body live mouse imaging by hybrid reflection-mode ultrasound and optoacoustic tomography. *Optics Letters*, 40(20):4643–4646, October 2015.

[131] Elena Merčep, Xosé Luís Deán-Ben, and Daniel Razansky. Combined Pulse-Echo Ultrasound and Multispectral Optoacoustic Tomography With a Multi-Segment Detector Array. *IEEE transactions on medical imaging*, 36(10):2129–2137, October 2017.

[132] Elena Merčep, Gency Jeng, Stefan Morscher, Pai-Chi Li, and Daniel Razansky. Hybrid optoacoustic tomography and pulse-echo ultrasonography using concave arrays. *IEEE transactions on ultrasonics, ferroelectrics, and frequency control*, 62(9):1651–1661, September 2015.

[133] Frank R. Miele. *Ultrasound Physics and Instrumentation, 4th Edition*. Pegasus Lectures, Inc., Forney, TX, 4th edition edition, January 2006.

[134] Miguel Angel Araque Caballero. *Incorporating Sensor Properties in Optoacoustic Imaging*. Dissertation, Technical University of Munich, Munich, 2013.

[135] P. Mohana Shankar and Vernon L. Newhouse. Speckle reduction with improved resolution in ultrasound images. *IEEE Transactions on Sonics and Ultrasonics*, 32(4):537–543, July 1985.

[136] P. Monnin, S. Bulling, J. Hoszowska, J.-F. Valley, R. Meuli, and F. R. Verdun. Quantitative characterization of edge enhancement in phase contrast x-ray imaging. *Medical Physics*, 31(6):1372–1383, June 2004.

[137] Stefan Morscher, Wouter H. P. Driessen, Jing Claussen, and Neal C. Burton. Semi-quantitative Multispectral Optoacoustic Tomography (MSOT) for volumetric PK imaging of gastric emptying. *Photoacoustics*, 2(3):103–110, September 2014.

[138] Vaseem Mulla. Ultrasound instrumentation physics, April 2017.

[139] Mohammadreza Nasiriavanaki, Jun Xia, Hanlin Wan, Adam Quentin Bauer, Joseph P. Culver, and Lihong V. Wang. High-resolution photoacoustic tomography of resting-state functional connectivity in the mouse brain. *Proceedings of the National Academy of Sciences*, page 201311868, December 2013.

[140] Andrew Needles, Andrew Heinmiller, John Sun, Catherine Theodoropoulos, David Bates, Desmond Hirson, Melissa Yin, and F. Stuart Foster. Development and initial application of a fully integrated photoacoustic micro-ultrasound system. *IEEE transactions on ultrasonics, ferroelectrics, and frequency control*, 60(5):888–897, May 2013.

[141] Volker Neuschmelting, Neal C. Burton, Hannah Lockau, Alexander Urich, Stefan Harmsen, Vasilis Ntziachristos, and Moritz F. Kircher. Performance of a Multispectral Optoacoustic Tomography (MSOT) System equipped with 2d vs. 3d Handheld Probes for Potential Clinical Translation. *Photoacoustics*, 4(1):1–10, December 2015.

[142] Joel J. Niederhauser, Michael Jaeger, and Martin Frenz. Comparision of laser-induced and classical ultasound. In *Biomedical Optoacoustics IV*, volume 4960, pages 118–124. International Society for Optics and Photonics, July 2003.

[143] Joel J. Niederhauser, Michael Jaeger, and Martin Frenz. Comparison of laser-induced and classical ultrasound. In *Biomedical Optoacoustics IV*, volume 4960, pages 118–124. International Society for Optics and Photonics, July 2003.

[144] Joël J. Niederhauser, Michael Jaeger, Robert Lemor, Peter Weber, and Martin Frenz. Combined ultrasound and optoacoustic system for real-time high-contrast vascular imaging in vivo. *IEEE transactions on medical imaging*, 24(4):436–440, April 2005.

[145] Vasilis Ntziachristos. Going deeper than microscopy: the optical imaging frontier in biology. *Nature Methods*, 7(8):603–614, August 2010.

[146] Vasilis Ntziachristos and Daniel Razansky. Molecular Imaging by Means of Multispectral Optoacoustic Tomography (MSOT). *Chemical Reviews*, 110(5):2783–2794, May 2010.

[147] Matthew O'Donnell and Thomas J. Linnemeier. Efficient synthetic aperture imaging from a circular aperture with possible application to catheter-based imaging. *IEEE transactions on ultrasonics, ferroelectrics, and frequency control*, 39(3):366–380, 1992.

[148] Milan Oeri, Wolfgang Bost, Steffen Tretbar, and Marc Fournelle. Calibrated Linear Array-Driven Photoacoustic/Ultrasound Tomography. *Ultrasound in Medicine & Biology*, 42(11):2697–2707, 2016.

[149] Jae K. Oh, James B. Seward, and A. Jamil Tajik. *The Echo Manual*. Lippincott Williams&Wilki, Philadelphia, 3rd ed edition, October 2006.

[150] Krzysztof J. Opielinski and Tadeusz Gudra. Multi-parameter ultrasound transmission tomography of biological media. *Ultrasonics*, 44:e295–e302, December 2006.

[151] Alan V. Oppenheim and Ronald W. Schafer. *Discrete-Time Signal Processing: Pearson New International Edition*. Pearson Education Limited, Harlow, 3 ed edition, July 2013.

[152] A. A. Oraevsky, B. Clingman, J. Zalev, A. T. Stavros, W. T. Yang, and J. R. Parikh. Clinical optoacoustic imaging combined with ultrasound for coregistered functional and anatomical mapping of breast tumors. *Photoacoustics*, 12:30–45, December 2018.

[153] Alexander A. Oraevsky, Steven L. Jacques, and Frank K. Tittel. Determination of tissue optical properties by piezoelectric detection of laser-induced stress waves. volume 1882, pages 86–101, July 1993.

[154] Catherine M. Otto. *Textbook of Clinical Echocardiography: Expert Consult - Online and Print*. Saunders W.B., Philadelphia, Pa, 5th edition edition, April 2013.

[155] Parasuraman Padmanabhan, Anu Maashaa Nedumaran, Sachin Mishra, Ganesh Pandarinathan, Govindaraju Archunan, and Balázs Gulyás. The Advents of Hybrid Imaging Modalities: A New Era in Neuroimaging Applications. *Advanced Biosystems*, 1(8):1700019, August 2017.

[156] Mailyn Pérez Liva. *Time domain image reconstruction methods for transmission ultrasound computed tomography*. Doctoral thesis, University Complutense of Madrid, Madrid, 2017.

[157] Bernd J. Pichler, Martin S. Judenhofer, and Christina Pfannenberg. Multimodal imaging approaches: PET/CT and PET/MRI. *Handbook of Experimental Pharmacology*, (185 Pt 1):109–132, 2008.

[158] Mailyn Pérez-Liva, Joaquin L. Herraiz, Luis Medina-Valdés, Jorge Camacho, Carlos Fritsch, Bradley E. Treeby, and J. M. Udías. Regularization of image reconstruction in ultrasound computed tomography. In *2015 IEEE Nuclear Science Symposium and Medical Imaging Conference (NSS/MIC)*, pages 1–3, October 2015.

[159] Xiaolei Qu, Takashi Azuma, Hongxiang Lin, Hirofumi Nakamura, Satoshi Tamano, Shu Takagi, Shin-ichiro Umemura, Ichiro Sakuma, and Yoichiro Matsumoto. Computational cost reduction by avoiding ray-linking iteration in bent-ray method for sound speed image reconstruction in ultrasound computed tomography. *Japanese Journal of Applied Physics*, 56(7S1):07JF14, June 2017.

[160] Jens U. Quistgaard. Signal acquisition and processing in medical diagnostic ultrasound. *IEEE Signal Processing Magazine*, 14(1):67–74, January 1997.

[161] Enrico Ragaini and Ronald F. Woodman. Demodulation of complex baseband radar signals for the analysis of multiple narrow spectral lines. *Radio Science*, 32(2):783–789, March 1997.

[162] Bin Rao, Li Li, Konstantin Maslov, and Lihong Wang. Hybrid-scanning optical-resolution photoacoustic microscopy for in vivo vasculature imaging. *Optics letters*, 35(10):1521–1523, May 2010.

[163] Daniel Razansky, Nikolaos C. Deliolanis, Claudio Vinegoni, and Vasilis Ntziachristos. Deep tissue optical and optoacoustic molecular imaging technologies for pre-clinical research and drug discovery. *Current Pharmaceutical Biotechnology*, 13(4):504–522, March 2012.

[164] Daniel Razansky, Martin Distel, Claudio Vinegoni, Rui Ma, Norbert Perrimon, Reinhard W. Köster, and Vasilis Ntziachristos. Multispectral opto-acoustic tomography of deep-seated fluorescent proteins in vivo. *Nature Photonics*, 3(7):412–417, July 2009.

[165] Amir Rosenthal, Vasilis Ntziachristos, and Daniel Razansky. Model-based optoacoustic inversion with arbitrary-shape detectors. *Medical Physics*, 38(7):4285–4295, July 2011.

[166] Amir Rosenthal, Daniel Razansky, and Vasilis Ntziachristos. Fast semi-analytical model-based acoustic inversion for quantitative optoacoustic tomography. *IEEE transactions on medical imaging*, 29(6):1275–1285, June 2010.

[167] Stephen Rosenzweig, Richard Bouchard, Thomas Polascik, Liang Zhai, and Kathryn Nightingale. Advanced Ultrasound: Prostate Elastography and Photoacoustic Imaging. In Robert L. Bard, Jurgen J. Fütterer, and Dan Sperling, editors, *Image Guided Prostate Cancer Treatments*, pages 31–45. Springer Berlin Heidelberg, January 2014.

[168] T. D. Sachs and C. D. Janney. A two-beam acoustic system for tissue analysis. *Physics in Medicine and Biology*, 22(2):327–340, March 1977.

[169] Robert W. Schoonover and Mark A. Anastasio. Image reconstruction in photoacoustic tomography involving layered acoustic media. *Journal of the Optical Society of America. A, Optics, Image Science, and Vision*, 28(6):1114–1120, June 2011.

[170] Chi Hyung Seo and Jesse T. Yen. Sidelobe Suppression in Ultrasound Imaging using Dual Apodization with Cross-correlation. *IEEE transactions on ultrasonics, ferroelectrics, and frequency control*, 55(10):2198–2210, October 2008.

[171] Qi Shao, Ekaterina Morgounova, Chunlan Jiang, Jeunghwan Choi, John Bischof, and Shai Ashkenazi. In vivo photoacoustic lifetime imaging of tumor hypoxia in small animals. *Journal of biomedical optics*, 18(7):076019, 2013.

[172] Lingyan Shi and Robert R. Alfano. *Deep Imaging in Tissue and Biomedical Materials: Using Linear and Nonlinear Optical Methods*. Pan Stanford Publishing Pte Ltd, Singapore, 1 edition, 2017.

[173] Steven Smith. *Digital Signal Processing: A Practical Guide for Engineers and Scientists*. Newnes, October 2013.

[174] Gerrit Sollie. Ultrasound transmission tomography: a low-cost realization. *PhD Thesis, Technische Universitaet Eindhoven*, September 1988.

[175] Ioan Sporea and Roxana Şirli. Is Contrast Enhanced Ultrasound (CEUS) ready for use in daily practice for evaluation of focal liver lesions? *Medical ultrasonography*, 16(1):37–40, March 2014.

[176] Bernard D. Steinberg. Digital beamforming in ultrasound. *IEEE transactions on ultrasonics, ferroelectrics, and frequency control*, 39(6):716–721, 1992.

[177] Ingo Stoffels, Stefan Morscher, Iris Helfrich, Uwe Hillen, Julia Leyh, Julia Lehy, Neal C. Burton, Thomas C. P. Sardella, Jing Claussen, Thorsten D. Poeppel, Hagen S. Bachmann, Alexander Roesch, Klaus Griewank, Dirk Schadendorf, Matthias Gunzer, and Joachim Klode. Metastatic status of sentinel lymph nodes in melanoma determined noninvasively with multispectral optoacoustic imaging. *Science Translational Medicine*, 7(317):317ra199, December 2015.

[178] Jochen Stritzker, Lorenz Kirscher, Miriam Scadeng, Nikolaos C. Deliolanis, Stefan Morscher, Panagiotis Symvoulidis, Karin Schaefer, Qian Zhang, Lisa Buckel, Michael Hess, Ulrike Donat, William G. Bradley, Vasilis Ntziachristos, and Aladar A. Szalay. Vaccinia virus-mediated melanin production allows MR and optoacoustic deep tissue imaging and laser-induced thermotherapy of cancer. *Proceedings of the National Academy of Sciences of the United States of America*, 110(9):3316–3320, February 2013.

[179] Jimmy L. Su, Bo Wang, Katheryne E. Wilson, Carolyn L. Bayer, Yun-Sheng Chen, Seungsoo Kim, Kimberly A. Homan, and Stanislav Y. Emelianov. Advances in Clinical and Biomedical Applications of Photoacoustic Imaging. *Expert opinion on medical diagnostics*, 4(6):497–510, November 2010.

[180] Thomas Szabo. *Diagnostic Ultrasound Imaging: Inside Out*. Academic Press, Amsterdam, 2. auflage. edition, December 2013.

[181] Hamid R. Tahmasebpour, Anne R. Buckley, Peter L. Cooperberg, and Cathy H. Fix. Sonographic examination of the carotid arteries. *Radiographics: A Review Publication of the Radiological Society of North America, Inc*, 25(6):1561–1575, December 2005.

[182] Yi Tan, Kaiye Xia, Qiushi Ren, and Changhui Li. Three-dimensional photoacoustic imaging via scanning a one dimensional linear unfocused ultrasound array. *Optics Express*, 25(7):8022–8028, April 2017.

[183] Jianbo Tang and Huabei Jiang. Single Element-Based Dual Focused Photoacoustic Microscopy. *Photonics*, 2(1):156–163, February 2015.

[184] Albert Tarantola. *Inverse Problem Theory: Methods for Data Fitting and Model Parameter Estimation*. Elsevier Science Ltd, Amsterdam ; New York : New York, NY, U.S.A, August 1987.

[185] Adrian Taruttis, Eva Herzog, Daniel Razansky, and Vasilis Ntziachristos. Real-time imaging of cardiovascular dynamics and circulating gold nanorods with multispectral optoacoustic tomography. *Optics express*, 18(19):19592–19602, September 2010.

[186] Adrian Taruttis, Stefan Morscher, Neal C. Burton, Daniel Razansky, and Vasilis Ntziachristos. Fast Multispectral Optoacoustic Tomography (MSOT) for Dynamic Imaging of Pharmacokinetics and Biodistribution in Multiple Organs. *PLoS ONE*, 7(1):e30491, January 2012.

[187] Adrian Taruttis and Vasilis Ntziachristos. Advances in real-time multispectral optoacoustic imaging and its applications. *Nature Photonics*, 9(4):219–227, April 2015.

[188] Adrian Taruttis, Arwin C. Timmermans, Philip C. Wouters, Marcin Kacprowicz, Gooitzen M. van Dam, and Vasilis Ntziachristos. Optoacoustic Imaging of Human Vasculature: Feasibility by Using a Handheld Probe. *Radiology*, 281(1):256–263, October 2016.

[189] Adrian Taruttis, Gooitzen M. van Dam, and Vasilis Ntziachristos. Mesoscopic and macroscopic optoacoustic imaging of cancer. *Cancer Research*, 75(8):1548–1559, April 2015.

[190] Hopp Torsten, Ruiter Nicole, Bamber C, Jeffrey, Duric Neb, and van Dongen W.A, Koen. *Proceedings of the International Workshop on Medical Ultrasound Tomography: 1.-3. Nov. 2017, Speyer, Germany*. KIT Scientific Publishing, January 2018.

[191] Bradley E. Treeby. Acoustic attenuation compensation in photoacoustic tomography using time-variant filtering. *Journal of Biomedical Optics*, 18(3):036008, March 2013.

[192] Ihor Trots, Andrzej Nowicki, Marcin Lewandowski, and Yuriy Tasinkevych. Synthetic Transmit Aperture Method in Medical Ultrasonic Imaging. 4(4), 2010.

[193] Ihor Trots, Andrzej Nowicki, Marcin Lewandowski, and Yuriy Tasinkevych. Synthetic Aperture Method in Ultrasound Imaging. April 2011.

[194] Stratis Tzoumas, Nikolaos Deliolanis, Stefan Morscher, and Vasilis Ntziachristos. Unmixing Molecular Agents From Absorbing Tissue in Multispectral Optoacoustic Tomography. *IEEE transactions on medical imaging*, 33(1):48–60, January 2014.

[195] Stratis Tzoumas, Antonio Nunes, Ivan Olefir, Stefan Stangl, Panagiotis Symvoulidis, Sarah Glasl, Christine Bayer, Gabriele Multhoff, and Vasilis Ntziachristos. Eigenspectra optoacoustic tomography achieves quantitative blood oxygenation imaging deep in tissues. *Nature Communications*, 7, June 2016.

[196] Barry D. Van Veen and Kevin M. Buckley. Beamforming: a versatile approach to spatial filtering. *IEEE ASSP Magazine*, 5(2):4–24, April 1988.

[197] Depeng Wang, Yuehang Wang, Weiran Wang, Dandan Luo, Upendra Chitgupi, Jumin Geng, Yang Zhou, Lidai Wang, Jonathan F Lovell, and Jun Xia. Deep tissue photoacoustic computed tomography with a fast and compact laser system. *Biomedical Optics Express*, 8(1):112–123, December 2016.

[198] Xueding Wang, Yongjiang Pang, Geng Ku, Xueyi Xie, George Stoica, and Lihong V. Wang. Noninvasive laser-induced photoacoustic tomography for structural and functional in vivo imaging of the brain. *Nature Biotechnology*, 21(7):803–806, July 2003.

[199] Xueding Wang, Yuan Xu, Minghua Xu, Seiichirou Yokoo, Edward S. Fry, and Lihong V. Wang. Photoacoustic tomography of biological tissues with high cross-section resolution: Reconstruction and experiment. *Medical Physics*, 29(12):2799–2805, December 2002.

[200] Yating Wang, Dong Xu, Sihua Yang, and Da Xing. Toward in vivo biopsy of melanoma based on photoacoustic and ultrasound dual imaging with an integrated detector. *Biomedical Optics Express*, 7(2):279–286, January 2016.

[201] Yu-Hsin Wang, Ai-Ho Liao, Jui-Hao Chen, Churng-Ren Chris Wang, and Pai-Chi Li. Photoacoustic/ultrasound dual-modality contrast agent and its application to thermotherapy. *Journal of Biomedical Optics*, 17(4):0450011–0450018, 2012.

[202] Judith Weber, Paul C. Beard, and Sarah E. Bohndiek. Contrast agents for molecular photoacoustic imaging. *Nature Methods*, 13(8):639–650, August 2016.

[203] Peter Neil Temple Wells. *Biomedical ultrasonics*. Academic Press, 1977.

[204] Jun Xia, Muhammad R. Chatni, Konstantin Maslov, Zijian Guo, Kun Wang, Mark Anastasio, and Lihong V. Wang. Whole-body ring-shaped confocal photoacoustic computed tomography of small animals in vivo. *Journal of Biomedical Optics*, 17(5):050506, May 2012.

[205] Jun Xia, Chao Huang, Konstantin Maslov, Mark A. Anastasio, and Lihong V. Wang. Enhancement of photoacoustic tomography by ultrasonic computed tomography based on optical excitation of elements of a full-ring transducer array. *Optics Letters*, 38(16):3140–3143, August 2013.

[206] Minghua Xu and Lihong V. Wang. Universal back-projection algorithm for photoacoustic computed tomography. *Physical Review E*, 71(1):016706, January 2005.

[207] Joon-Mo Yang, Christopher Favazza, Ruimin Chen, Junjie Yao, Xin Cai, Konstantin Maslov, Qifa Zhou, K. Kirk Shung, and Lihong V. Wang. Simultaneous functional photoacoustic and ultrasonic endoscopy of internal organs *in vivo*. *Nature Medicine*, 18(8):1297–1302, August 2012.

[208] Hongxia Yao. *Synthetic aperture methods for medical ultrasonic imaging*. PhD thesis, 1997.

[209] Karin Zell, Jonathan I. Sperl, Mika W. Vogel, Reinhard Niessner, and Christoph Haisch. Acoustical properties of selected tissue phantom materials for ultrasound imaging. *Physics in Medicine and Biology*, 52(20):N475–484, October 2007.

[210] Karel Zuiderveld. Contrast limited adaptive histogram equalization. In Paul S. Heckbert, editor, *Graphics Gems IV*, pages 474–485. Academic Press Professional, Inc., San Diego, CA, USA, 1994.